ION IMPLANTED BRAGG GRATINGS IN SOI RIB WAVEGUIDES

Ion Implanted Bragg Gratings in Silicon-on-Insulator Rib Waveguides

By

MICHAEL BULK

B.Sc. (McMaster) 2005

A Thesis
Submitted to the School of Graduate Studies
in Partial Fulfilment of the Requirements
for the Degree

Master of Applied Science (M.A.Sc.)

McMaster University
©Copyright by Michael Bulk, 2008.

MASTER OF APPLIED SCIENCE (2008)
(Engineering Physics)

McMaster University
Hamilton, Ontario

TITLE: Ion Implanted Bragg Gratings in Silicon-on-Insulator Rib Waveguides

AUTHOR: Michael Bulk

SUPERVISOR: Dr. P.E. Jessop

NUMBER OF PAGES: viii, 122

Abstract

Ion implanted Bragg gratings integrated in rib waveguide structures were simulated, fabricated and characterized for the silicon-on-insulator (SOI) photonics platform. After selective silicon self-implantation, to an amorphizing dose of 2×10^{15} ions/cm^2, the approximately 0.3 damage-induced increase in the refractive index provided the modulation mechanism necessary for the formation of a Bragg grating. The benefits of implanted Bragg gratings compared to the more widely utilized surface relief type gratings include planar surface retention, desirable for subsequent processing and wafer bonding, and a smaller depth of the index modulation, important for minimizing filtering bandwidths. To our knowledge, this is the first time ion implantation has been utilized to produce Bragg gratings integrated in an SOI rib waveguide. The benefits of using SOI for an optoelectronics platform include: cost minimization, reduced device size, and compatibility with silicon based microelectronics.

Device performance was simulated using coupled mode theory (CMT) in conjunction with beam propagation methods (BPM), to determine transverse modal profiles for computing coupling coefficients and to determine geometric dimensions suitable to achieve adequate grating strength and single-mode operation. The Monte Carlo ion implantation simulator SUSPREM4, implementing the binary collision approximation (BCA), was used to determine the amorphous silicon grating profiles. Implanted grating devices were then fabricated into SOI having a 2.5 μm device layer and were optically characterized. For a grating length of 2100 μm and an implant energy of 60 keV, the extinction ratio of the resonant wavelength was found to be -18.11 dB and -0.87 dB for TE and TM polarizations respectively. The excess loss per unit length was measured to be 1.2 dB/mm for TE polarization and 0.6 dB/mm for TM polarization. After annealing the gratings at temperatures of up to 300 °C, used to annihilate low energy point defects responsible for absorption, it was found that the excess loss per unit

length was reduced to 0.3 dB/mm for TE polarization. Compared to etched gratings with similar dimensions, it was determined that the strength of the implanted gratings was approximately 2.5 times stronger for grating lengths one third the length as result of mode-shifting due to the higher index of refraction. This is of great consequence to the miniaturization and densification of Bragg grating based devices in silicon photonics.

Acknowledgements

First of all, I would like to thank my supervisor, Dr. Paul Jessop, for allowing me to pursue this Masters degree and for providing me with the insight and guidance that allowed for the success of this project.

I would also like to thank Dr. Andy Knights for his invaluable advice, ideas and his genuine interest in my project that really helped me through some of the more difficult aspects of the research.

I would also like to extend a giant thank you to Chris Brooks. He not only helped me immensely in learning the intricacies of scientific research, silicon processing and optical characterization, but he also became a great friend and spent many hours talking to me about, and helping me out with some of the technical challenges of my research.

Many thanks also go out to the entire centre for emerging device technology (CEDT) research staff. They provided their knowledge and expertise in helping me setup my experiments and endowed me with invaluable training that I will continue to use for years to come. Thank you to Shabnam Homampour for helping with some of the measurements required for my research.

I also would like to thank my fantastic girlfriend Ashley and my good friend Scott, for supporting me and putting up with me for the past two years. Finally, I want to send a special thank you to my parents. I greatly appreciate the support, the advice, and the sacrifices you have made to allow me to get to this stage of my life. I can not express how thankful I am for everything you guys have done for me throughout my life.

Contents

CHAPTER 1 INTRODUCTION **1**

1.1 OPTICS AND THE PROGRESSION TOWARDS INTEGRATION 1
1.2 SILICON PHOTONICS 3
1.3 BRAGG GRATINGS AND SILICON PHOTONICS 5

CHAPTER 2 BACKGROUND THEORY **9**

2.1 THE PROPAGATION OF GUIDED LIGHT 9
2.1.1 Maxwell's Equations and the Electromagnetic Wave Equation *11*
2.1.2 Wave Propagation in Slab Waveguides *14*
2.1.3 SOI Rib Waveguides and the Effective Index Method *18*
2.1.4 Single Mode Condition for Rib Waveguides *20*
2.1.5 Beam Propagation Method and Mode Profiles *21*
2.1.6 Reversal Symmetries and Mode Orthogonality *22*
2.2 ION IMPLANTATION IN SILICON 24
2.2.1 Fundamentals of Ion Implantation *25*
2.2.2 Ion-Beam-Induced Defects and Damage Accumulation *27*
2.2.3 Amorphous Silicon Damage Profiles *30*
2.2.4 Damage-Induced Refractive Index Modification and Loss *35*
2.2.5 Post-Implant Annealing *39*
2.3 MODELLING IMPLANTED BRAGG GRATINGS IN WAVEGUIDE STRUCTURES 40
2.3.1 Bragg Grating Fundamentals *43*
2.3.2 Grating Modelling and Contradirectional Coupled Mode Theory *46*
2.3.3 The Coupling Coefficient and Grating Strength *53*
2.3.4 Grating Spectral Response and Gratings with Loss *61*
2.3.5 Propagation Losses Due to Implant *69*

CHAPTER 3 FABRICATION **72**

3.1 FABRICATION OF SILICON PHOTONIC DEVICES 72
3.2 FABRICATION OF BRAGG GRATINGS 75
3.2.1 Lithographic Based Fabrication Techniques *75*
3.2.2 Other Fabrication Methods for Bragg Gratings *79*
3.3 IMPLANTED BRAGG GRATINGS IN SOI WAVEGUIDES 80

CHAPTER 4 EXPERIMENTAL RESULTS **93**

4.1 EXPERIMENTAL SETUP FOR OPTICAL CHARACTERIZATION 93
4.2 TRANSMISSION SPECTRA AND STRENGTH OF IMPLANTED GRATINGS 95
4.3 LOSS MEASUREMENTS 101
4.4 LOW TEMPERATURE ANNEALING EFFECTS 103
4.5 COMPARISON TO ETCHED GRATINGS 107

CHAPTER 5 CONCLUSION **110**

List of Figures

Figure 1.1 Surface Relief and Index Modulated Grating types. 6

Figure 2.1 Assymetric slab waveguide structure 10
Figure 2.2 First three computed TE modes in an asymmetric waveguide. 18
Figure 2.3 General rib type structure in SOI. 19
Figure 2.4 The effective index method for a rib waveguide 19
Figure 2.5 Depiction of implant requirements for an implanted Bragg grating in SOI. 32
Figure 2.6 Lateral damage profiles using SUSPREM4 simulator. 33
Figure 2.7 Longitudinal damage profile of 50 keV Si implant in Si. 35
Figure 2.8 Schematic of integrated photonic devices employing Bragg gratings. 42
Figure 2.9 Ion implanted Bragg grating in waveguide structure 44
Figure 2.10 Integrated Bragg grating conceptualized as a dielectric stacked mirror 44
Figure 2.11 Additional Layer Method used to model Bragg grating. 47
Figure 2.12 Phase matching conditions for forward and backward coupling 52
Figure 2.13 Maximum reflected power versus the silicon device layer height. 56
Figure 2.14 Calculated coupling coefficient κ vs. duty cycle for TE and TM modes 58
Figure 2.15 Modal confinement of TE and TM modes 59
Figure 2.16 Mode profiles for implant depth of 250nm 60
Figure 2.17 Calculated reflected and transmitted spectra of Bragg gratings 66
Figure 2.18 Calculated reflected spectrum normalized to transmitted power 68
Figure 2.19 Calculated reflected spectrum versus the absorption coefficient 69
Figure 2.20 Propagation loss versus grating length for TE and TM polarization 70

Figure 3.1 Interference holography principles 76
Figure 3.2 Lloyd's mirror setup employing a 325 nm HeCd laser 77
Figure 3.3 Fabrication process utilised to produce implanted Bragg gratings in rib 81
Figure 3.4 SEM showing deposited SiO_2 layer and a-Si layer 83
Figure 3.5 Illustration of fabricated Bragg gratings 88
Figure 3.6 Dimensions of the actual etched rib and the simulated rib 91
Figure 3.7 SEM image of the completed ion implanted SOI rib structure. 92

Figure 4.1 Experimental setup for optical characterization. 94
Figure 4.2 Measured TE transmission spectra versus length for 60 keV implantation 96
Figure 4.3 Measured transmission spectra of TE and TM polarization 98
Figure 4.4 Grating strength versus grating length for 50 keV and 60 keV implants. 98
Figure 4.5 Comparison of measured and calculated TE spectral response 100
Figure 4.6 Excess loss measurements for TE and TM polarizations 102
Figure 4.7 Excess loss and the absorption loss as a function of annealing temperature 104
Figure 4.8 Annealing response of transmitted grating spectra 105
Figure 4.9 Etched grating in SOI rib waveguide 108
Figure 4.10 TE and TM transmission spectra of etched Bragg grating 108

List of Tables

Table 3-1 Processing steps to achieve Bragg gratings in PR 85

Chapter 1

Introduction

1.1 Optics and the Progression towards Integration

Over the past 15 years, telecommunication networks based on fiber optic technology have pervaded the information-transmission industry, substantiated by the unparalleled bandwidth afforded by optical fibers. Traditionally, the information carrying capacity was limited by the resistive and capacitive effects imparted on the electrons by

the metal cabling and terminating electronics. However, in optical cables, the information carrying photon is only capacity limited by dispersive effects [1]. Also, the unique chargeless nature of the photon enables the coexistence of multiple optical signals in the same guiding medium with minimal cross talk. These characteristics give optical systems unprecedented bandwidth and speed compared to an equivalent electrical system. Consequently, the deployment of optically based networks formed the groundwork for a complete restructuring of data and information sharing mechanisms on a global scale, with the end result being the proliferation of high speed internet globally.

As the demand for instantaneous data, voice and video becomes greater and greater, further deployment of optical fiber becomes necessary. In fact, we are now seeing fiber optic networks being directly routed to households (Fiber to the Home). Someday optics may even provide a means to transmit signals between different components inside your computer [2]. With this, increasingly more devices providing functions such as routing, switching, and multiplexing are required. Electronically based devices, requiring optical-electrical-optical (OEO) conversions, tend to be temporally restrictive and impractical, leading to a need for their equivalent optical counterparts. Unfortunately, traditional optical components are expensive, large, and take tremendous time and practise to properly align. In order to achieve compact, low cost, manufacturable optical components, it is beneficial to progress towards device integration, which revolutionized the electronics industry; serving as the catalyst to our present 'silicon' age. Integration allows for the synchronous production of innumerable devices, with near identical behaviour.

The idea of integrated optics was originally conceptualized in the 1960s when work outlining the design and analysis of waveguides, bends and filters was presented [3]. Since then, many material platforms, including III-V compounds [4], polymers [5], oxide based systems [6], and sol-gel [7], have been proposed to provide optical integration, all having a varying degree of success. Often the degree of success is limited to factors such as material cost, or relatively unknown processing techniques. With electrical bottlenecks in silicon looming, the ubiquity and inexpensiveness of silicon, and the existence of well established fabrication processes and facilities, attention has been turning to a previously unlikely candidate for the optics revolution: silicon.

1.2 Silicon Photonics

Silicon is the backbone to all present day microelectronics. It is a cheap, abundant, and well understood material that can be processed to be among the purest crystalline solids existing [8]. There exist countless well defined fabrication processes that allow for device integration down to the nanometer scale. As it turns out, silicon is also virtually transparent to wavelengths greater than 1.1 μm. This immediately reinforces its candidacy to support optical device functionality in the standard telecom windows of 1.3 and 1.55 μm. These benefits for optics have already been pointed out by a number of authors [9-11].

Originally a groundbreaking material for the scaling of microelectronics, silicon-on-insulator (SOI) also provides the necessary characteristics for silicon to become a

photonics platform. SOI consists of a silicon device layer that is separated from the bulk silicon crystal by a thin insulating layer, usually silicon dioxide. The high refractive index contrast between that of silicon and silicon dioxide provides the optical confinement necessary for the propagation of purely guided modes [12]. The high index contrast also allows for the dense integration of optical components and tight bend radii relative to that of III-V material systems or optical fibers [10]. With all the existing technology in place, photonic devices in silicon can be designed with an unparalleled degree of integration at a fraction of the cost of standard optical components. It also lends itself to the seamless integration of both electrical and optical functionality on the same wafer, opening entirely new technological possibilities.

The advantages of silicon as a photonics platform are also offset by a number of disadvantages. Physically, silicon is fundamentally limited by two major issues, an indirect band gap and centrosymmetric inversion symmetry [13]. The former is a major obstacle in producing an efficient silicon light source, while the latter results in a negligible electro-optic effect. Despite these short-comings numerous methods have been developed to counteract these limitations and have resulted in gain in silicon and the production of monolithic optical modulators operating in excess of 2.5 GHz [14-16]. Other disadvantages lie in the vulnerability of light propagation to non-idealities of the structure (mainly surface scattering) and coupling losses due to a high degree of modal mismatch between the fiber modes and silicon rib waveguide modes [17].

Over the past two decades a myriad of silicon photonic devices have been conceived to provide functionalities that include switching [18], splitting [19], infrared

signal detection [20], and coupling [21]. Another important device to silicon photonics is the Bragg grating. Gratings can provide functions that are not limited to filtering, mode converting, coupling and reflecting, and they also have dimensions suitable for integration [22].

1.3 Bragg Gratings and Silicon Photonics

Fiber Bragg gratings (FBG) are a fundamental element of optical fiber networks and are used in applications ranging from dispersion compensation to optical add/drop filtering [23]. They have also found a multitude of sensorial uses, ranging from temperature sensing to biological sensing [23]. On the other hand, Integrated Bragg gratings, which are not solely reliant on the photorefractive effect, can be implemented with a greater degree of functionality.

Integrated Bragg gratings can be broken down into two categories, surface relief gratings and index modulated gratings. The two types of gratings are illustrated in Figure 1.1. The surface relief grating is defined by a physical removal of the substrate, through a process such as etching, and generally has large coupling coefficients with abrupt interfaces. These types of gratings are inherently passive devices. Index modulated gratings can be formed through phenomenological effects that include the photorefractive effect, electro-optic effect, acousto-optic effect, or even through doping processes. These devices are interesting because they have active device capabilities and they generally retain a planar surface. Planar surface retention is an increasingly important attribute as

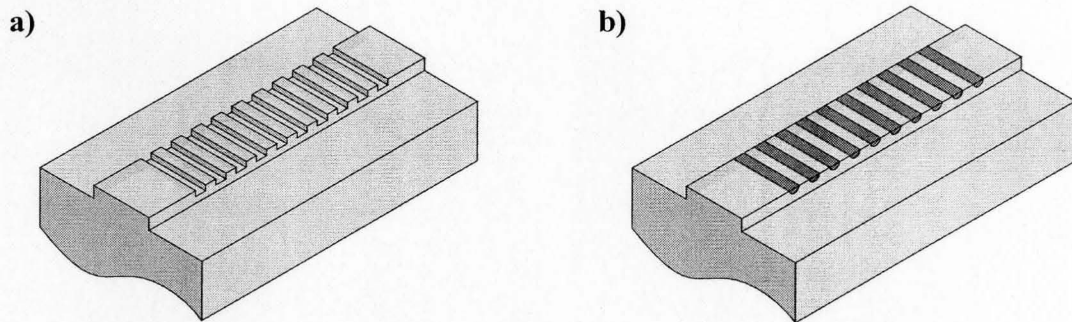

Figure 1.1 a) Surface relief grating and b) index modulated grating.

optically integrated circuits are progressing towards three-dimensional integration to increase device density [24].

The preliminary wok on integrated gratings was in providing the feedback mechanisms for distributed feedback (DFB) and distributed Bragg reflector (DBR) semiconductor lasers, having III-V material platforms [25, 26]. However, as technology progressed numerous other applications for Bragg gratings with a variety of material platforms were explored. To name a few, integrated gratings on SiO_2/Si_3N_4 rib waveguides were fabricated at Bell Laboratories [27], laser written Bragg gratings were demonstrated in fused silica at Macquarie University [28] and even electrically tuneable Bragg gratings were introduced in unique polymer based materials [29].

In the case of SOI, where many of the optical effects are negligible, a surface relief type grating is often the most viable option. These devices are inherently passive, although electrically tuneable Bragg gratings based on the plasma dispersion effect have been developed [30]. Thermo-optically tuned Bragg gratings have also been realized [31]. The grating is typically formed through a lithographic patterning technique and an

etching sequence. Indeed, SOI waveguide couplers and filters have been demonstrated using interference holography and RIE etching [32], or e-beam lithography [33]. More recently, focused ion beam milling was used to fabricate higher order mode conversion and filtering in SOI [34, 35].

A common problem to surface corrugated gratings is the non-planar surface required. As mentioned, with an increasing trend towards three dimensional optical circuits, maximum planar retention is desirable for the complex bonding techniques required. Also, the optical filters tend to have limited spectral bandwidths due to the high index contrast of the gratings.

Fortunately, silicon has a unique property, which was first explored by Baranova *et al.* in the early seventies [36]. When ions are implanted in crystalline silicon, the imparted energy of the impinging ions causes damage to the lattice. As the damage accumulates there is also an increase in the index of refraction. The refractive index increases until the damaged crystalline undergoes transformation to the amorphous state, at which point the index of refraction saturates to a value ~0.3 greater than the crystalline value [37].

This has immediate implications for gratings in SOI. By selectively implanting periodic regions, the gratings can be formed by the ion implantation induced amorphization of silicon. With this method the gratings retain a planar surface and have some flexibility concerning the degree of contrast present between grating teeth. The trade-off is the introduction of loss due to the damage from the ion implantation process, which was first explored by Fan and Ramdas [38].

Therefore, the ultimate goal of this thesis is to explore the viability of producing integrated Bragg gratings in SOI rib waveguides using ion beam induced amorphization, and compare their optical characteristics to etched gratings with similar dimensions.

Chapter 2 will explore the background theory surrounding wave propagation in SOI rib waveguides. It will also cover the basics of ion implantation, damage accumulation, and predicting the amorphous profile through Monte Carlo implant simulations. Coupled mode theory will then be introduced as a method to model the implanted Bragg gratings and predict their response to incident light.

Chapter 3 outlines the design and fabrication procedures followed to integrate the implanted Bragg gratings in SOI rib waveguides. Two samples with different implantation energies were fabricated with multiple grating lengths patterned on each sample.

Finally, Chapter 4 presents the experimental results obtained from the samples and analyzes the results by using comparisons to simulated models, surface relief gratings with similar dimensions, and by performing annealing studies.

Chapter 2

Background Theory and Analysis

2.1 The Propagation of Guided Light

The principles of light propagation and its interaction with matter are well established and the background material presented in this section is also covered in great detail in many introductory texts [10, 39-41].

Diffraction, a fundamental optical property resulting from the wave nature of light, predicts the divergence of optical beams with a finite cross section as they propagate in free-space. Therefore, in free-space optics it is necessary to employ lenses and other optical components to control the beam. Alternatively, Snell's Law enunciates the ability to confine propagating light when a dielectric medium of higher refractive index is surrounded by a material with a lower refractive index. Figure 2.1 shows a basic asymmetric dielectric slab waveguide. In this case T is the guiding layer thickness, $\theta_{c,n1/n2}$ represent the critical angles for total internal reflection and $n_2 > n_3 > n_1$. For SOI waveguides, n_1 is usually air, n_2 is silicon and n_3 is silicon dioxide. Provided the guiding layer is greater than a critical thickness, the structure depicted will be able to confine light when the incident angles at the dielectric interfaces are greater than both critical angles. In this simplified ray model, the light will continue to propagate in a zig-zag pattern without attenuation, provided the material is lossless. For incident angles smaller than the critical angle, large radiation losses will occur at the dielectric interfaces.

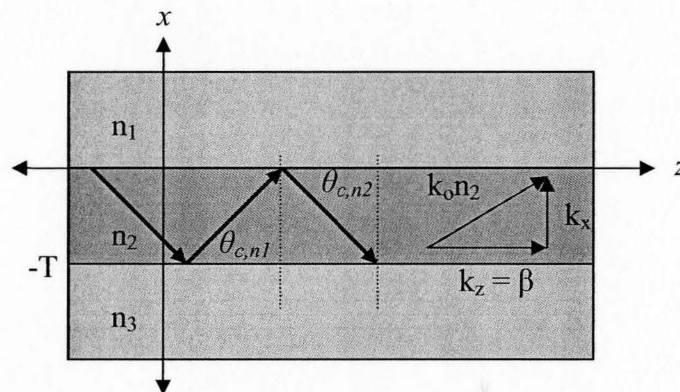

Figure 2.1 Assymetric slab waveguide of thickness T and index n_2 surround by media of lower index n_1 and n_3

Through a geometric optics formulism, or the electromagnetic wave equation, it can be shown that only discrete guided-modes exist, and their characteristics are determined by the geometry of the waveguide. In the geometric optics approach the modes are classified by their incident angle, as shown in the figure above, while for wave optics they are classified by their propagation constant β. Since a full description of the propagating mode is required in this work, only the wave optics approach will be analyzed. The following sections will determine the modal characteristics of confined light in both one-dimensional and two-dimensional waveguides by examining Maxwell's equations through analytical, approximate and numerical methods. Both the transverse electric (TE) and transverse magnetic (TM) modes of propagation will be examined. Some of the optical properties, particularly mode orthogonality, will be introduced as a precursor to couple mode theory, which is presented in section 2.2.

2.1.1 Maxwell's Equations and the Electromagnetic Wave Equation

In the late nineteenth century, James Clerk Maxwell published his groundbreaking theories of electromagnetism. For the first time all the interactions between electric, magnetic, electromagnetic and optical phenomena could be explained by the same fundamental set of laws. These laws have predicted the existence of many important phenomena including the presence of electromagnetic waves in free-space. Maxwell's equations can be expressed as

$$\nabla \times E = -\frac{dB}{dt} \tag{2.1}$$

$$\nabla \times H = \frac{dD}{dt} + J \tag{2.2}$$

$$\nabla \cdot D = \rho \tag{2.3}$$

$$\nabla \cdot B = 0 \tag{2.4}$$

In the above equations E and H are the time varying electric field vector and magnetic field vector respectively. The parameters D and B represent the electric displacement and magnetic displacement vectors respectively, while J is the electric current density vector and ρ is the electric charge density. The electric current density and electric charge can be considered a source of electromagnetic radiation. The above relations govern the electromagnetic field in its entirety.

For optical components, comprising primarily of dielectric materials, it is often the case that both the current density ρ and the charge density J are zero. Substituting $\rho = J = 0$ into Maxwell's equations results in non-zero solutions, thus proving the existence of electromagnetic fields in the absence of any charges or currents. To obtain unique solutions for the field vectors E and H, constitutive (material) relations must be employed to reduce the number of unknowns. The constitutive relations are

$$D = \varepsilon E \tag{2.5}$$

$$B = \mu H \tag{2.6}$$

where ε and μ are the permittivity and permeability tensors respectively and represent macroscopic parameters relating the interaction of a material with electric and magnetic fields.

To derive the wave equations, we take the curl of both sides of Equation (2.1) employ Equation (2.2) and substitute in relations (2.5) and (2.6). We now use the familiar vector identity $\nabla \times \nabla \times E = \nabla(\nabla \cdot E) - \nabla^2 E$, assume $\rho = J = 0$, and simplify to obtain the result

$$\nabla^2 E - \mu\varepsilon \frac{d^2}{dt^2} E = 0 \tag{2.7}$$

This represents the familiar wave equation for the electric field vector E in a homogenous and isotropic medium. A similar result can also be found for the magnetic field vector H, but is not shown.

The solutions to the wave equations are electromagnetic waves of the form

$$E(x,y,z,t) = E_o(r,t)e^{i(k \cdot r - \omega t)} \tag{2.8}$$

where $E_o(r,t)$ is the slowly varying amplitude of the harmonic wave, k is the wave vector and ω is the angular frequency. The wave vector is defined as $|k| = 2\pi / \lambda$, where λ is the wavelength. For the situation when $E_o(r,t)$ is a constant in space and time the solutions are reduced to plane waves. Substituting Equation (2.8) into the wave equation leads to the relationship

$$k^2 E = \omega^2 \mu\varepsilon E \tag{2.9}$$

or

$$k^2 = \omega^2 \mu\varepsilon \tag{2.10}$$

where this is referred to as the *dispersion relation*. For surfaces of constant phase the phase velocity of the propagating wave can be expressed as

$$v = \frac{\omega}{k} = \frac{1}{\sqrt{\mu\varepsilon}} \tag{2.11}$$

Also, the refractive index is defined as

$$v = \frac{c}{n} \tag{2.12}$$

and $c = 1/\sqrt{\mu_o\varepsilon_o}$ in a vacuum. Therefore, assuming $\mu = \mu_o$, the index of refraction of a dielectric medium can be expressed as

$$n = \sqrt{\frac{\varepsilon}{\varepsilon_o}} \tag{2.13}$$

2.1.2 Wave Propagation in Slab Waveguides

As mentioned previously, a dielectric layer surrounded by layers having a lower refractive index can guide light as a result of total internal reflection. To analyze the propagation characteristics of the structure in Figure 2.1, the wave equation can be applied to each dielectric layer, while enforcing the required continuity relations at each dielectric interface.

Assuming a plane wave propagating in the *z*-direction, the electromagnetic fields vary as

$$E(r) = E(x,y)e^{i(\omega t - \beta z)} \tag{2.14}$$

$$H(r) = H(x,y)e^{i(\omega t - \beta z)} \tag{2.15}$$

where β is the propagation constant and is equivalent to the *z* component of the wave vector k_z. For convenience, the effective index *N* of the mode can be introduced and is defined as

$$\beta = Nk_o \tag{2.16}$$

and $N = n_2 \sin\theta$. The effective index can be thought of as the index of refraction of the mode as it propagates down the waveguide. Analyzing the conditions required for total internal reflection, it can be found that the effective index must adhere to $n_3 < N < n_2$.

Due to the structural invariance of the slab waveguide in the *y*-direction, the electromagnetic fields are independent of *y*. Maxwell's equations predict the existence of two mutually orthogonal states. These are the TE and TM modes of the waveguide. The TE modes have their electric field perpendicular to the *xz* plane and have field components E_y, H_x, and H_z. TM modes have the field components H_y, E_x, and E_z.

The solutions described in Equations (2.14) and (2.15) must obey the wave equation in all three layers. After substitution, the wave equation for TE polarization can be computed as

$$\frac{\partial^2 E_y}{\partial x^2} + \left(k_o^2 n^2 - \beta^2\right) E_y = 0 \tag{2.17}$$

where the remaining magnetic field components can be determined through Maxwell's equations. Similarly, for TM polarization the wave equation becomes

$$\frac{\partial^2 H_y}{\partial x^2} + \left(k_o^2 n^2 - \beta^2\right) H_y = 0 \tag{2.18}$$

The solutions of the TE and TM modes form an eigenvalue equation when subject to the boundary conditions at the interfaces $x = 0$ and $x = -T$. Since the derivation of the TE and TM modes is similar, only the TE modes will be discussed here. The TE field solutions in all three dielectric layers have the form

$$E_y = \begin{cases} E_1 e^{-\gamma_1 x} & x > 0 & \text{cover} \\ E_2 \cos(k_x x + \varphi) & 0 \geq x \geq -T & \text{guiding layer} \\ E_3 e^{\gamma_3 (x+T)} & x < -T & \text{substrate} \end{cases} \tag{2.19}$$

where,

$$\gamma_1^2 = \beta^2 - n_1^2 k^2 \tag{2.20}$$

$$k_x^2 = n_2^2 k^2 - \beta^2 \tag{2.21}$$

$$\gamma_3^2 = \beta^2 - n_3^2 k^2 \tag{2.22}$$

The continuity relations require that the tangential field components E_y and H_z and their derivatives are continuous at the interfaces $x = 0$ and $x = -T$. At $x = 0$, after simplification, we obtain

$$\begin{gathered} E_1 = E_2 \cos\varphi \\ \tan\varphi = \gamma_1 / k_x \end{gathered} \tag{2.23}$$

Similarly, at $x = -T$

$$\begin{gathered} E_3 = E_2 \cos(k_x T - \varphi) \\ \tan(k_x T - \varphi) = \gamma_3 / k_x \end{gathered} \tag{2.24}$$

Combining the above relations we obtain the following transcendental equation

$$k_x T = (m+1)\pi - \tan^{-1}\left(\frac{k_x}{\gamma_3}\right) - \tan^{-1}\left(\frac{k_x}{\gamma_1}\right) \tag{2.25}$$

where m = 0, 1, 2... denote the $TE_{m=0,1,2...}$ mode numbers. The TE_0 mode is the fundamental mode of the waveguide and has the largest effective index corresponding to the ray with the angle closest to 90 degrees. We note that because m is a positive integer there only exist discrete solutions that have a corresponding discrete wave vector and propagation constant. These discrete solutions are deemed the modes of the waveguide.

Provided the indices of the layers and the thickness T are known, k_x can be determined from Equation (2.25). Upon substitution of k_x into Equation (2.21) the propagation constant β and the effective index N can be determined. When the effective index N of the modes is within the range $n_3 < N < n_2$ the propagating light will be confined. Therefore, under certain geometric conditions only a limited number of modes will be supported and the other modes will be 'cut-off'. This is very important because the waveguide parameters can now be tailored to only allow certain modes to propagate.

Compared to the ray picture, the wave model allows one to obtain the modal profile of the propagating mode, which is essential to integrated photonic device design. The first three modes of an arbitrary asymmetric three-level waveguide are illustrated in Figure 2.2.

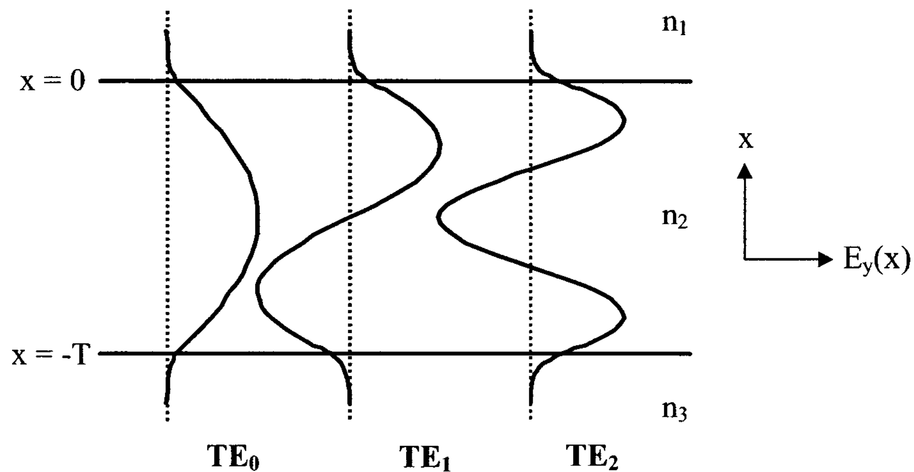

Figure 2.2 First three computed TE modes in an asymmetric waveguide.

From the figure it is seen that the modes are sinusoidal or cosinusoidal in the medium n_2, depending if the mode number is even or odd. Alternatively, the imaginary root present in the cladding layers leads to solutions which decay exponentially. If the roots are not imaginary in the cladding layers, sinusoidal solutions may exist and light is no longer confined to the core region. Sinusoidal solutions that exist in all three regions are called the radiation modes of the waveguide.

2.1.3 SOI Rib Waveguides and the Effective Index Method

In practise slab waveguides can be impractical because they only confine light in one direction. In order to have complete Cartesian routing capabilities it is necessary to provide a means of lateral confinement to the slab waveguide structure. In many

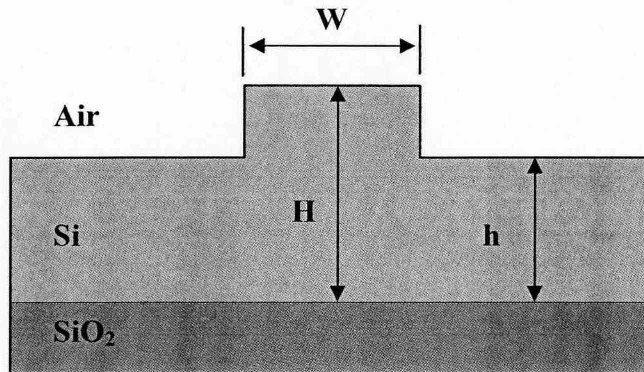

Figure 2.3 General rib type structure in SOI.

integrated optical circuits, and especially in an SOI platform, the lateral confinement is provided through a rib type structure. The rib structure is generally formed through a partial etch of the silicon device layer via reactive ion etching (RIE) or wet chemical etching. A typical rib structure in SOI is illustrated in Figure 2.3.

Unlike the previous slab waveguide analysis, no analytical solutions exist for the rib waveguide. As a result, intensive numerical solutions are often required to solve for the modes of the waveguide. Fortunately, the effective index method (EIM) can be employed to compute approximate modal solutions. The basis of EIM is outlined in Figure 2.4.

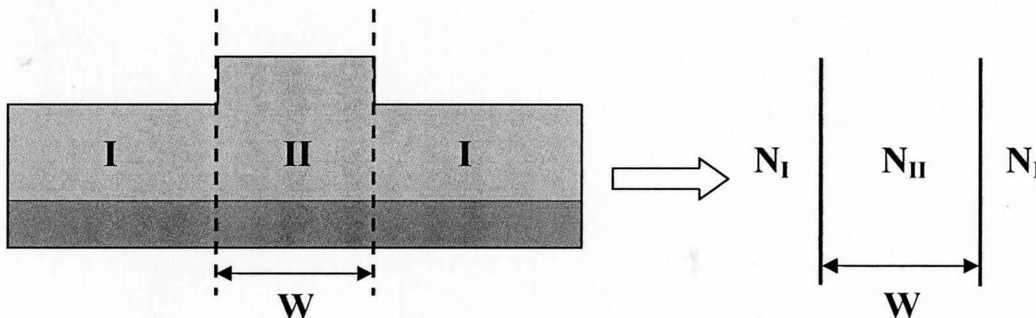

Figure 2.4 The effective index method for a rib waveguide structure.

The effective index method reduces the three-dimensional rib waveguide into a problem that involves the solution of two separate slab waveguide problems, one in the vertical direction and one in the horizontal direction. The rib region *II* and the two side regions *I* are first treated as individual slab waveguides with confinement in the *x*-direction. The effective indices of each region then form the indices describing the confinement of the slab waveguide in the lateral direction. Solving for the lateral slab waveguide, we obtain an approximate index of the entire structure. This tends to be a good approximation in many situations, but is less accurate for large index steps and complex structures. If we assume regions *II* and *I* are both single mode slab waveguides, in order to achieve modal confinement in the rib, Figure 2.4 illustrates that the required condition is $N_{II} > N_{I}$.

When solving for the TE-like modes of the rib waveguide, the effective index is first solved in each slab region assuming TE mode solutions. After synthesizing the effective slab structure, the TE modes become the TM modes of the laterally confined slab waveguide. Therefore, the slab solutions must be computed assuming TM solutions. To find the TM-like modes of the rib waveguide the analysis is exactly flipped.

2.1.4 Single Mode Condition for Rib Waveguides

Due to its high refractive index, single mode waveguides in silicon are exceedingly small relative to the corresponding dimensions of single mode optical fibers. Such dimensional discrepancies lead to a large degree of modal mismatch between the two waveguides and an impractically large amount of coupling losses [42]. Then in the

early 1990s, Soref *et al.* demonstrated the ability to produce single mode rib waveguides with dimensions otherwise thought to be multimode [43]. It was found that with certain parameters only the fundamental mode was strongly confined to the rib and subsequent higher order modes radiated out the sides of the rib. Confirmation of single mode propagation was carried out through the empirical work and EIM analysis of Rickman and Pogossian respectively [44, 45]. The single mode condition is given by

$$\frac{W}{H} \leq c + \frac{h/H}{\sqrt{1-(h/H)^2}} \tag{2.26}$$

where the parameters are defined by Figure 2.3 and c is a constant that has been debated to have a value of either 0.3 or -0.05 by Soref and Pogossian. According to Soref's derivation, the single mode condition is restricted to occurrences where $(r = h/H) < 0.5$. The requirement simply states that the etched slab region must be at least half the height of the rib region. This ensures adequate coupling of the higher order vertical modes in the rib region with the fundamental mode of the slab regions. Indeed, if the effective indices of the higher-order modes of the rib waveguide fall below the effective index of the fundamental mode of the side region they will couple out of the rib [46].

2.1.5 Beam Propagation Method and Mode Profiles

While the effective index method allows for an understanding of the guiding conditions of a rib waveguide, it fails to provide a spatial description of the mode profile. Often a numerically based approach is required for modal profiles in complex waveguide structures, resulting in time-intensive computations. Of these, the Beam Propagation

Method (BPM) is perhaps one of the most widely used numerical methods due to its computational speed [47]. The premise behind the BPM involves factoring the rapid phase variation out of the wave equation in the propagation direction by introducing a slowly varying field u. This results in the fundamental BPM equation

$$\frac{\partial u}{\partial z}=\frac{j}{2k_r}\left(\frac{\partial^2 u}{\partial x^2}+\frac{\partial^2 u}{\partial y^2}+\left(k^2-k_r^2\right)u\right) \tag{2.27}$$

where k_r is known as the reference wave number and represents the average phase variation of the field. Equation (2.27) shows that the wave equation is reduced to a first order initial value problem that can be solved via a simple integration in the propagation direction z. Although numerous numerical methods can be employed, many of the BPM algorithms implement the finite-difference method to solve this numerical integral.

The finite-difference method establishes a discrete grid in the transverse (xy) plane describing the electric or magnetic field and computes its evolution at discrete points along the propagation direction z. Provided an initial launch condition is given, the BPM algorithm computes the transverse field at the next grid point z and repeats the process successively through the remaining structure. Therefore, at any point along the propagation direction the field profile may be extracted and analyzed, making this very convenient to monitor field changes.

2.1.6 Reversal Symmetries and Mode Orthogonality

We previously described the guiding characteristics and modal profiles of waveguide structures. We will now introduce a few modal properties that are important

to formulating coupled mode theory (CMT), which will be used to model the integrated Bragg gratings in this thesis.

The first set of waveguide properties are known as the waveguide symmetry properties. For simplicity, breaking down the E field into longitudinal and transverse components yields

$$\begin{aligned} E &= E_t + \hat{z}E_z \\ E_t &= \hat{x}E_x + \hat{y}E_y \end{aligned} \tag{2.28}$$

The H field can be separated in a similar manner. It is possible to show that if the propagation constant β is substituted with $-\beta$, Maxwell's equations are still satisfied provided we make the following replacements

$$\begin{aligned} E_t &\to E_t \quad & H_t &\to -H_t \\ E_z &\to E_z \quad & H_z &\to H_z \end{aligned} \tag{2.29}$$

Therefore, every forward propagating mode has a corresponding backward propagating mode and they are related through Equation (2.29). This is known as z-reversal symmetry. In a similar manner, the complex conjugates of the fields are also a solution of Maxwell's equations and this property is known as time-reversal symmetry [48].

The basis of CMT stems from the orthogonality relations for dielectric waveguides. The derivation of these relations is excluded but they can be generalized compactly for all m and n modes as [48]

$$\iint \left(E_{mt} \times H_{nt}\right) \cdot \hat{z}dS = 2P\,\mathrm{sgn}(n)\delta_{|m|,|n|} \tag{2.30}$$

where P is the power carried by the mode, sgn(n) is defined as +1 if n is positive and -1 if it is negative, and $\delta_{m,n}$ is the Kronecher delta, which is zero unless $m = n$. The relation

states that all the modes supported by the waveguide structure are orthogonal. Therefore, provided the modes represent a complete set, they form a basis set and can be used to describe any arbitrary light propagating in the waveguide through linear superposition.

2.2 Ion Implantation in Silicon

Ion implantation has been crucial to the introduction of dopants into silicon integrated circuits for the past twenty years and is poised to remain dominant in this area for years to come. As the dimensions of devices continue to decrease the spatial requirements of the doping profiles become increasingly strict. The unique dechanneling properties of amorphous silicon have made ion beam-induced amorphization of silicon extremely important to confine doping profiles to very shallow and narrow regions, enabling the production of next generation silicon devices [49].

Ion implantation also provides a means to tailor the optical properties of silicon and, as a result, has tremendous ramifications for integrated optical circuits in silicon. In particular, amorphous silicon possesses unique optical properties, such as a higher refractive index than crystalline silicon, which makes it an interesting material for integrated optics [50]. Therefore, the selective ion implantation induced-amorphization of silicon provides added flexibility and diversity in the fabrication of silicon photonic circuits. Indeed, the higher refractive index of implanted silicon has been exploited as a means to provide optical confinement previously [51].

This work is primarily interested in the added functionality provided by the selective self-amorphization of silicon photonic devices. As a result, the conditions for, and profiles of, self-amorphized silicon will be explored by examining the defect production and damage accumulation incurred during ion implantation, how the optical properties are affected, and the response to annealing. To begin some of the basic concepts of ion implantation will be presented.

2.2.1 Fundamentals of Ion Implantation

Since the defect profile is intimately tied to the ion stopping profile, it is beneficial to review some of the basic principles of ion implantation. As an incident ion impinges the silicon surface it will begin to interact with, and impart energy on, the constituent lattice ions. The ion will begin to lose energy through both nuclear and electronic interactions, where the rate of energy loss with distance travelled in the target is given by

$$\frac{dE}{dx} = -N\left[S_n(E) + S_e(E)\right] \tag{2.31}$$

Here, N is the density of the target (5×10^{22} cm^{-3} for silicon) and $S_n(E)$ and $S_e(E)$ are the nuclear and electronic stopping powers respectively [49]. Nuclear stopping encompasses the losses that are incurred through the elastic scattering of the ions from target atoms, while electronic stopping describes the additional inelastic drag forces caused by electronic interactions. Both of the loss mechanisms are dependent on the velocity of the incident ion. In general, the nuclear stopping power tends to be larger for lower energies. At high energies there is a reduced cross section caused by small interaction times of the

fast particles with the scattering nuclei. Conversely, the drag forces increase proportionately with velocity and tend to be unappreciable for low energy implants. Also, nuclear stopping powers increase with the atomic number Z of the ion. Therefore, light ions moving at high velocities tend to have significant electronic stopping powers, while nuclear stopping powers dominant for heavy ions at low implant energies. In either respect, the ion will continue to propagate the crystal lattice until its energy is reduced to approximately 15 eV, whereby the cohesive forces will trap the ion in the lattice [52].

Because of the random nature of the scattering process, and the large number of ions implanted, the ion distribution is often modelled to first order by a symmetric Gaussian distribution given by

$$C(x) = C_p \exp\left(-\frac{\left(x - R_p\right)^2}{2\Delta R_p^2}\right) \tag{2.32}$$

where C_p is the peak concentration where the Gaussian is centred, R_p is the average range normal to the surface and ΔR_p is the straggle about the range [49]. The peak concentration can be found through

$$C_p = \frac{Q}{\sqrt{2\pi}\Delta R_p} \tag{2.33}$$

where Q is the dose of the implant. The random nature of the process also results in lateral scattering with a corresponding lateral straggle. In practical devices blanket implants are rarely used. Instead, an implant window is utilized and the characteristics of the lateral straggle become very important. It can be quite difficult to experimentally

measure lateral doping profiles, so it is often assumed that the two-dimensional distribution is a composed of the product of the vertical and lateral distributions as

$$C(x,y) = C_{vert}(x)\exp\left(-\frac{y^2}{2\Delta R_l^2}\right) \tag{2.34}$$

where ΔR_l is the lateral straggle. To determine the range and straggle of the implanted ions a statistical approach is required. Although numerous methods exist, only monte-carlo simulators, such as Marlowe [53] and Transport of Ions in Matter (TRIM) [54], consider the atomic structure of the silicon lattice in detail, making it suitable to predict values of the range and straggle.

While the modelling of ion distributions in terms of a distribution function is useful, it fails to provide a complete description of the detailed atomic-scale events that take place along the ion's trajectory. An atomistic approach has proven to be the only viable method to accurately model the final damage and ion distribution in crystalline silicon.

2.2.2 Ion-Beam-Induced Defects and Damage Accumulation

As the ion propagates the silicon lattice the ion-atom interactions can cause structural modifications due to the energy transfer from the implanted ions to the lattice atoms. Provided the ion possesses a total energy of 15 – 20 eV, known as the threshold energy, the collision can produce a vacancy-interstitial *V-I* (Frenkel) pair [55]. Below the threshold energy, the energy transfer will only result in lattice vibrations and,

consequently, a local heating of the target material. This is known as the thermal spike regime. When the incident ions impart a much larger energy to the lattice atoms than is required to produce a Frenkel Pair, the kinetic energy of the displaced atoms can cause further displacements of lattice atoms. These additional events are known as recoils. Therefore, the production of defects is a cascade process, with the impinging ion initializing the process. The net effect of all the displacement events is referred to as the collision cascade of the ion. Large defect densities are typically found within the region of the ion path, with the majority of the defects located near the end of range (EOR), where the ion's energy is sufficiently low so that nuclear displacement collisions dominant.

The entire kinetic collision process is terminated after about one picosecond [56]. For approximately the next nanosecond a thermalization process occurs whereby part of the collision cascade is annihilated due to interactions with other migrating point defects [57]. The migration of point defects is known to be temperature dependent, so a reduction in the implant temperature allows for a greater retention of the collision cascade damage. The collapsing of the collision cascade is referred to as dynamic annealing. The remaining damage typically exhibits clusters of vacancies surrounded by interstitials. Therefore, the cascade consists of point defects, defect complexes or, some have speculated, locally amorphous regions [36, 58, 59]. The core of the cascade has been shown to be amorphous for heavy ions, whereas only isolated defect clusters exist for the implantation of light ions [60, 61]. Generally, a definitive structure of individual

cascades has to be prognosticated via modelling as their small size (~10^{-25} cm^3) make their investigation by experimental means tremendously difficult.

As the ions bombard the silicon surface the cascades produced overlap and point defects, defects clusters and amorphous regions aggregate until a highly unstable *c*-Si lattice exists. At some point, it becomes thermodynamically favourable for the *c*-Si to undergo a transformation to an *a*-Si state. The *a*-Si state preserves the four-fold coordination characteristic of *c*-Si, but the long range order is suppressed by distortions of the bond angles [52]. There also tends to be a high concentration of defects in the as-implanted material that include dangling bonds [62], floating bonds [63], and strained Si-Si bonds [64].

As might be expected, the cumulative mechanism of amorphization construes a critical dependence on the irradiation parameters. The accumulation of damage is dictated by a competition between damage accumulation and dynamic annealing. It has been shown that the mass of the ion species, the temperature of the substrate, the dose and the dose rate of the implanted ions all play an interdependent role on amorphization [52]. Observations have deemed that as the ion fluences increase the amount of residual damage increases, where a critical fluence is required at a particular temperature to induce a wholly amorphous layer [56]. It was found that light ions generally required higher fluences than heavy ions and that the critical fluence at room temperature is significantly higher than implants carried out at liquid nitrogen temperatures [57, 65, 66]. For the case of silicon self-amorphization, doses on the order of 10^{15} (cm^{-3}) have been demonstrated to

produce amorphous layers at liquid nitrogen temperatures [65]. For further information on the amorphization of silicon, an excellent review is given in [52].

2.2.3 Amorphous Silicon Damage Profiles

The small size and short lifetime of cascades makes it difficult to accurately measure cascade profiles. As a result, it is often necessary to employ theoretical models to predict the number of atoms displaced by a bombarding ion and provide an estimate of the amount of damage incurred. Numerous models have been proposed for this purpose, with the most noteworthy being molecular dynamic (MD) simulations [67], computer simulations based on the binary collision approximation (BCA) [68], such as TRIM and MARLOWE, and analytical models based on linear Boltzmann transport theory [69]. The BCA model only considers collisions amongst moving and stationary atoms in the displacement cascade, while the full collision dynamics are incorporated into the MD models. Therefore, the MD models tend to provide more accurate results at the expense of computational time. This work utilizes a BCA based simulator known as SSUPREM4, which is part of the ATHENA 2D process simulation software, and implements a Monte Carlo based implantation method.

There have been numerous phenomenological models proposed to interpret experimental amorphization results, however no single model properly accounts for all the experimental observations. Some of these models include the critical energy/defect density model [70], overlap damage model [57], nucleation limited model [71], and various defect-based models [52]. One of the most well used models, and is considered

hereafter, is the critical energy/defect density model. In this model, the energy deposited by bombarding ions per unit volume must exceed a critical value for an energetically favourable transformation to the amorphous state to occur. In terms of defects, this relates to displacement concentrations on the order of 10% of the silicon lattice density of 5×10^{22} atoms/cm^{-3} [72].

As mentioned, the defects from one cascade will combine and also annihilate with defects from other cascades. The accumulation of damage is the net result of this process. At the point of amorphization, the incremental change in the damage saturates. Mathematically, the increment in the damage due to an additional implanted ion in a volumetric element can be expressed as

$$\Delta n(x) = nf_{rec}\left(1-\frac{N}{N_{\alpha}}\right) \tag{2.35}$$

where n is the number of displacement defects generated in an isolated cascade, f_{rec} is the fraction of defects that recombine within a cascade and from overlapping cascades, N is the local defect density and N_{α} is the threshold defect density where the crystal is effectively amorphous. When N is larger than the threshold defect density, there is no further increase in the incremental damage due to additional cascades. As mentioned, the threshold defect damage required to induce amorphization is often quoted to be 10% of the silicon lattice density.

To form an implanted grating suitable for telecommunication wavelengths in an SOI rib structure requires a periodicity on the order of 220 nm. The implant mask can be illustrated as in Figure 2.5.

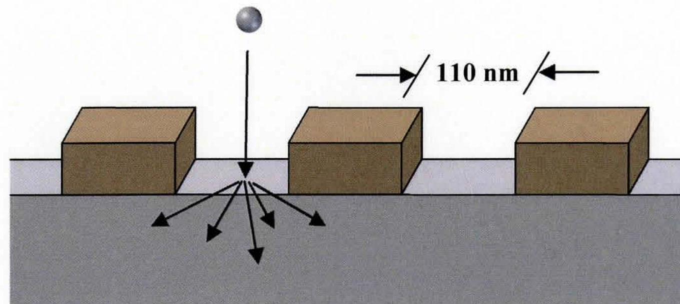

Figure 2.5 Depiction of implant requirements for an implanted Bragg grating in SOI.

As the implanted ion interacts with the silicon lattice atoms the randomness of the collision process results in a two-dimensional damage profile that will extend under the mask edges. The depth of the implant and the lateral straggle are both increasing functions of the implantation energy. Since each implantation window is only 110 nm, it is crucial that the overlap of the implant damage from adjacent teeth is minimal; otherwise the modulation depth of the implanted grating will become nonexistent. Therefore, the lateral implant damage from any window should be less than about 55 nm, or half the distance of the grating tooth. This results in a limitation of the implant depth due to the energy limited lateral damage constraint. As will be shown later, the depth of the grating strongly influences the strength of the grating and, therefore, SOI substrate dimensions have to be taken into consideration to ensure adequate grating strength.

The SUSPREM4 simulator was used to determine the maximum implant energy to ensure adequate lateral grating modulation. Once this energy was determined the maximum implant depth was obtained. Assuming silicon self-implantation, a duty cycle of 50/50 for the implantation mask, a dose of 2×10^{15} (cm^{-2}), liquid nitrògen implantation

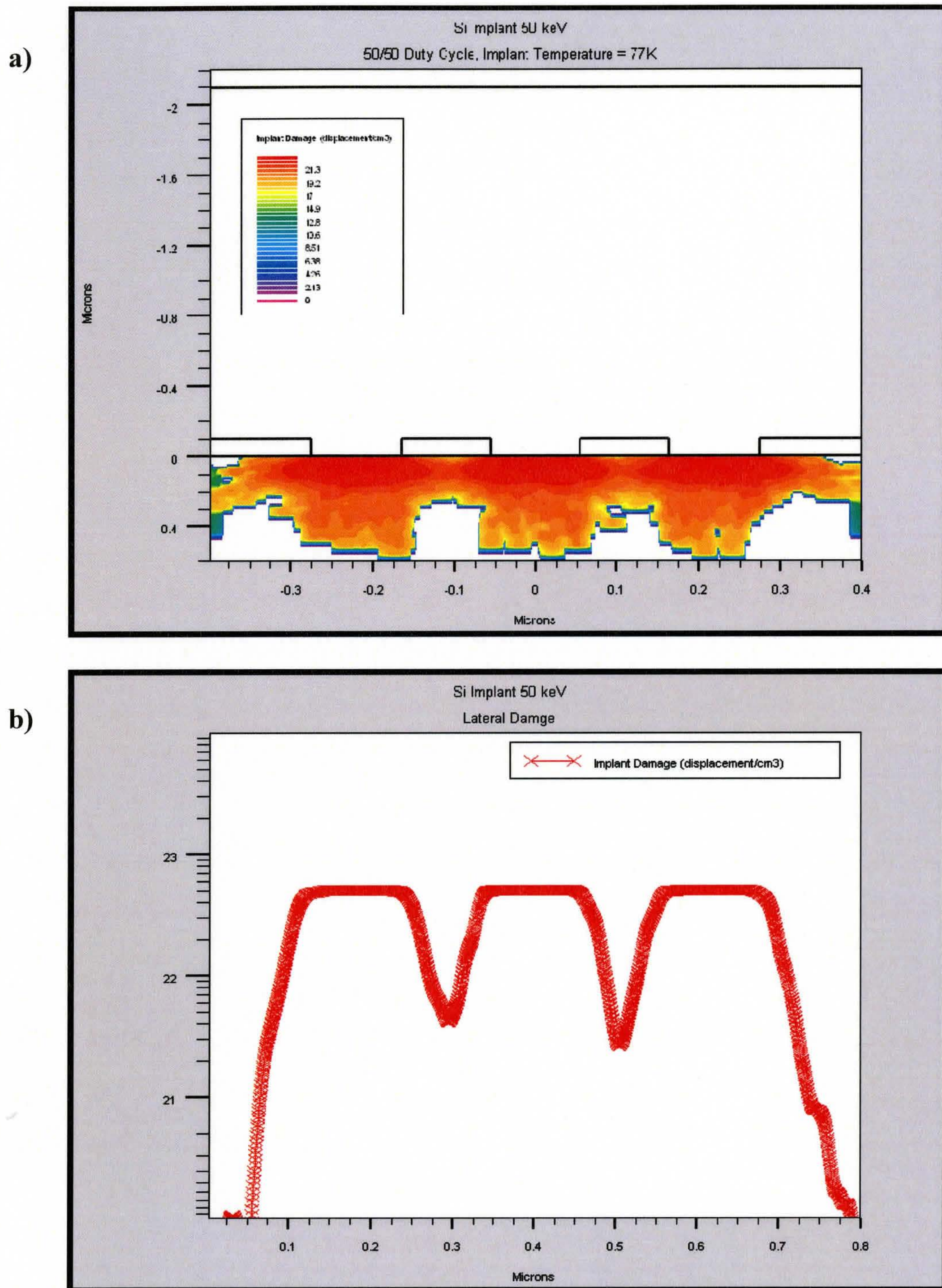

Figure 2.6 a) Damage profile obtained using the SSUPREM4 implantation simulator, b) lateral cutline depicting the lateral damage profile.

temperature, and allowing the Monte Carlo algorithm to simulate 100,000 implanted ions, a typical damage profile is presented in Figure 2.6.

By implementing the 10% displacement criterion, the plots can be analyzed and only the implanted areas exhibiting greater than 5×10^{21} displacements/cm^{-3} were considered amorphous. By increasing the implantation energy and monitoring the lateral damage profile, it was determined that to satisfy the lateral damage constraints, implantation energies of up to about 60 keV can be used. For energies higher than this the overlap of damage cascades between adjacent teeth begins to deteriorate the index modulation significantly. From the profile it was also found that the duty cycle of the 50 keV implanted grating is approximately 20/80 for crystalline silicon to amorphous silicon regions.

In a similar manner, the depth of the amorphous region can be determined knowing the maximum implant energy imparted by the lateral constraint. Figure 2.7 shows the implantation damage as a function of depth for a 50 keV implant. For a 50 keV implant the estimated amorphous silicon depth is 155 nm.

It was previously noted that the implantation profiles are dependent on the ion species, implantation temperature, dose, dose rate and other factors. Therefore, these results are specific to the implant conditions specified above. By altering the ion species, duty cycle of the implantation mask, and other parameters, alternative damage profiles can be achieved.

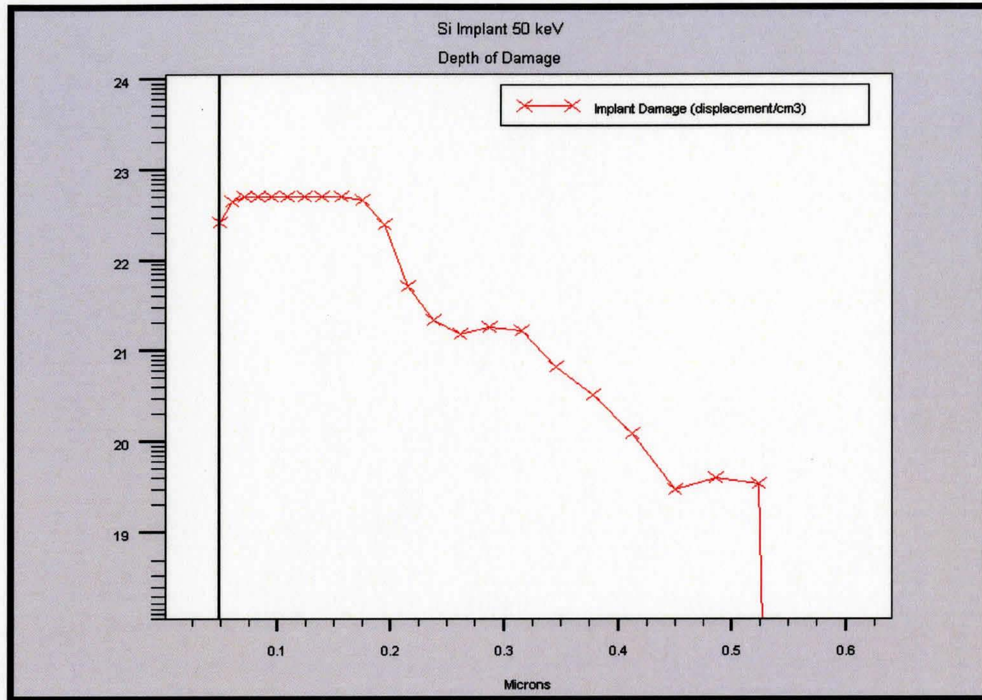

Figure 2.7 Longitudinal damage profile of 50 keV Si implant in Si.

2.2.4 Damage-Induced Refractive Index Modification and Loss

Investigations have shown that the real part, as well as the imaginary part, of the refractive index increases as damage accumulates in the silicon lattice [73-77]. Numerous sources have determined that the real part of the refractive index is approximately 0.3 greater than that of crystalline silicon for wavelengths in the near infrared [51, 77]. The studies found that, provided the implantation temperature is below a critical value, the index of refraction increases abruptly with dose and then saturates; a similar manner observed in defect accumulation, suggesting the intimate correlation

between the structural defects and the optical properties of ion-implanted silicon. Similar to silicon amorphization, the increase in index requires higher doses for lighter ions. However, lighter ions tend to exhibit a more abrupt increase in the index, compared to a more gradual increase for heavier ions [77]. For this reason, it was suggested that the increase in the index is related to the relative volumetric change of the amorphous phase within the crystalline silicon.

It was initially hypothesized that the increase in the refractive index could be attributed to an increased atomistic density of the amorphous silicon relative to crystalline silicon. However, experimental evidence has determined that the density of amorphous silicon is in fact approximately 1.8% lower than crystalline silicon [78]. Since the increased refractive index is not attributable to a densification of the electronic oscillators, other modification mechanisms have been suggested. Zammit *et al.* determined that a large degree of lattice strain is present in implant-induced amorphous silicon due to bond-angle variation caused by the presence of point defects [79]. Studies involving calorimetry, raman scattering, and infrared reflectivity have also found evidence suggesting similar results [80, 81]. The optical absorption studies performed by Zammit *et al.* correlated a reduction in the refractive index of as-implanted *a*-Si to the annealing of point defects and a concomitant reduction in lattice strain. However, after low temperature anneals, eliminating many of the point defects, a thermally-stabilized amorphous silicon still exists, exhibiting a refractive index in between as-implanted and crystalline silicon [82]. Hence, point defect induced strain only attributes partially to refractive index modifications.

Fredrickson *et al.* suggested that the increased index of refraction could be ascribed to the presence of dangling bond defects introduced during ion implantation [83]. Previous films grown by the evaporation and thermal decomposition of silane onto thermally oxidized silicon showed a relation between the refractive index and the presence of dangling bonds, which have a polarizing ability greatly enhanced compared to covalent bonds in crystalline silicon [84]. However, a paper released by the same group a few years later found evidence that the density of dangling bonds is not sufficient to explain the degree of the index shift [75]. After invoking the Drude or Lorentz-Lorentz dielectric equations they determined that a ~28% increase in the average bond polarizability could explain the increased index of refraction. Therefore, with insufficient work to support a particular cause, it is often stated that the increase in the refractive index is a result of a modification in the electronic band structure of crystalline silicon [51].

The modification of the electronic band structure also has a significant effect on the absorption characteristics. Numerous authors have demonstrated a broadening of the band edges and the introduction of defect related electronic states in the band gap that are directly related to the implant-induced damage [79, 85-87]. This leads to substantial subgap optical absorption and inflated absorption coefficients. In fact, absorption coefficients on the order of thousands of decibels per centimetre have been reported, limiting amorphous silicon's functionality as a photonic material [77]. However, losses in the range of 300 dB/cm have been demonstrated via the aid of low temperature

annealing (~500 °C), making it suitable for optical devices with lengths that are less than ~100 μm [51].

Of interest to operating wavelengths in the range of 1.55 μm, are the absorption bands associated with the silicon divacancy defect. Divacancies are stable at room temperature and were found to be the primary vacancy type defect as confirmed by Coleman, Burrows, and Knights [88]. The absorption bands associated with the various states of the divacancy have been observed at 1.8 μm, 3.3 μm and 3.9 μm [89]. In particular, the 1.8 μm absorption band possesses tails that extend to wavelengths in the telecom range. In the case of heavier ion implantation, such as silicon, it is known that implantation results in an increase in divacancy concentration first, goes through a maximum on the order of 10^{19} cm^{-3} and then decreases until a completely amorphous layer is formed [77]. There have been numerous successful models to predict the effect of divacancies on optical absorption, however they are limited to pre-amorphization dose regimes when the absorption is mainly related to the concentration of divacancies.

With increasing dose the absorption losses tend to saturate after the onset of amorphization [77]. Absorption losses remain large, but the divacancy concentration decreases suggesting that the concentration of other loss abetting defects is still high. These losses can be linked to absorption from defects and traps, such as dangling bond and point defect complexes, and scattering losses due to variations in the structural homogeneity of the amorphous silicon network [85]. Fortunately, loss effects can be partially mitigated via low temperature annealing.

2.2.5 Post-Implant Annealing

Post-implant annealing of amorphous silicon reveals various temperature dependent stages, indicative of the hierarchical nature of the damaged structure. Annealing studies have also uncovered the metastability of the as-implanted amorphous silicon network, with a thermally-relaxed amorphous silicon existing in conjunction to the initial as-implanted transitional state.

Interstitial and vacancy type point defects exhibit a high degree of mobility and tend to diffuse at temperatures lower than room temperature [90]. Slightly more structurally complex defects, namely di-interstitials and divacancies, require annealing temperatures of 150 °C [91] and 100-250 °C [92] respectively. As damage accumulates, simple point defects undergo agglomeration to form extended defects clusters of interstitials or vacancies that include, {113} defects, dislocation loops, clusters of vacancies, and cavities [52]. Temperatures of 800-1000 °C are often required to remove these types of defects, although at approximately 400 °C most of the vacancy type defects break up and the released point defects annihilate with interstitials. The removal of complex clusters typically involves the dissolution of clusters to point defects that diffuse towards, and eventually are annihilated at, the surface.

An interesting property of implanted silicon is the presence of a thermally relaxed amorphous state with a significantly reduced absorption coefficient [77]. The sharpening of the band edges and the broad exothermic nature of the process suggest that the network readjusts progressively during annealing to a completely relaxed state. It has been

reported that the process can be ascribed to a reduction in the strain of the material, which can be associated with a readjustment of the bond angle and bond length in the amorphous silicon network [93]. Numerous studies have demonstrated a correlation between the mutual reduction in strain and bond angle distortion to the annihilation of points defects and defect complexes [94, 95]. Annealing has also been found to significantly reduce the concentration of dangling bond type defects [62].

As the annealing temperature increases, the progressive annihilation of the point defects and defects clusters and the elimination of the 1.8 μm divacancy absorption band lead to a sharpening of the band edges and a reduction in the number of defect states existing in the band gap. Consequently, the subgap optical absorption is repressed and absorption coefficients on the order of 3 – 6 times lower than the as-implanted samples have been reported for annealing temperatures as low as 550 °C [77]. Also, the strain-reduced relaxed amorphous silicon state was found to possess a refractive index that is approximately 95% of the as-implanted state [83]. Therefore, annealing as-implanted silicon provides tremendous benefits for photonic applications by maintaining an increased refractive index, while significantly reducing the absorption losses.

2.3 Modelling Implanted Bragg Gratings in Waveguide Structures

As previously described, Maxwell's equations predict the existence of modes in accordance with the continuity relations and boundary conditions invoked by the waveguide's physical geometry. Of particular interest are the mode orthogonality and the

z-reversal and time-reversal symmetric waveguide properties. Mathematically, and intuitively, these properties state that in a dielectric waveguide all the supported modes are orthogonal and for every forward-travelling mode with propagation constant β_z, there exists a corresponding backward-travelling mode with propagation constant $-\beta_z$, where the remaining field components are related by the equations given in Section 2.1.6. This is important as the ability to efficiently couple power from the forward propagating mode to the backward propagating mode leads to features important to optical devices such as optical feedback, wavelength filtering and broadband reflection.

One method to provide contradirectional coupling is through the introduction of fine periodic refractive index variations in the dielectric medium. In a one-dimensional arrangement these structures are referred to as Bragg gratings. It is noted that Bragg gratings can be thought of as a subset of photonic crystals, although typically, photonic crystal terminology is concerned with two and three dimensional periodicity. For familiarity, there exist alternative situations where waves propagate in periodic media. For instance, an electron subject to the periodic electrostatic potential of the lattice ions gives rise to the presence of electronic bandgaps in semiconductors. A similar situation also occurs when x-rays diffract from a crystallographic lattice. Therefore, it can be beneficial to examine the corollaries between these seemingly unrelated topics to better understand, and form, the analytical and empirical models used to describe each of them.

Bragg gratings integrated in optical waveguide structures possess many unique qualities that make them of paramount importance to the development of optically integrated circuits. They possess dimensions, structures, and fabrication procedures

ideally suited to integration. At the most basic level, a Bragg grating allows for the manipulation of the propagation constant of the incident light through diffraction. In a passive orientation, Bragg gratings can be implemented as wavelength filters, input/output couplers, waveguide couplers, mode converters, and focusing couplers to name a few [22]. Figure 2.8 illustrates a number of the passive grating geometries that can be realized in integrated optics.

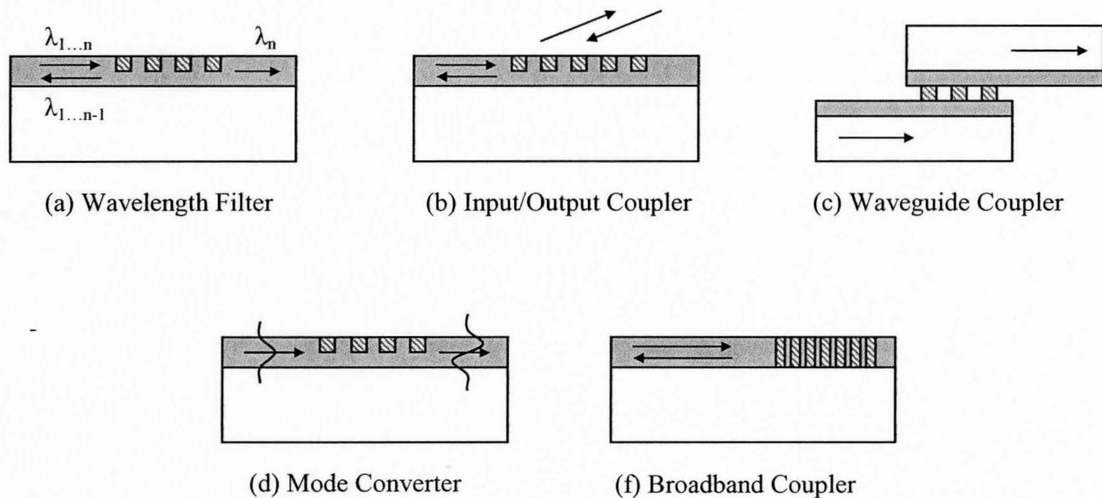

Figure 2.8 Schematic diagram depicting a variety of integrated photonic devices employing Bragg gratings.

Over the past few decades numerous materials and methods have been developed to introduce periodic modifications to guiding layers. As mentioned, the most well known method employs the photorefractive effect via UV illumination to change the index of refraction in fiber Bragg gratings. Other methods include the use of the acousto-optic effect and the electro-optic effect, providing active device functionality [20]. Unfortunately, these methods are limited to materials that exhibit appreciable electro-

optic, acousto-optic or photorefractive properties. In the case of silicon, where these properties are weak, different approaches are required. The most common approach is to physically corrugate the surface with a lithography and etching process or focused ion beam milling. However, there is an expressed interest in planar surface retention for subsequent processing, limiting the aforementioned techniques. Alternatively, ion implantation can be utilized to locally modify the index of refraction while retaining a planar surface. Therefore, modeling of planar gratings created via ion implantation will be discussed in the following sections.

2.3.1 Bragg Grating Fundamentals

The structure we wish to investigate is depicted in Figure 2.9. The grating is formed via selective silicon ion implantation, where crystalline damage accumulates and eventually increases the index of refraction. As damage is produced it also introduces defects that cause an increase in the optical absorption. An inherent trade-off then exists between index modification and optical absorption.

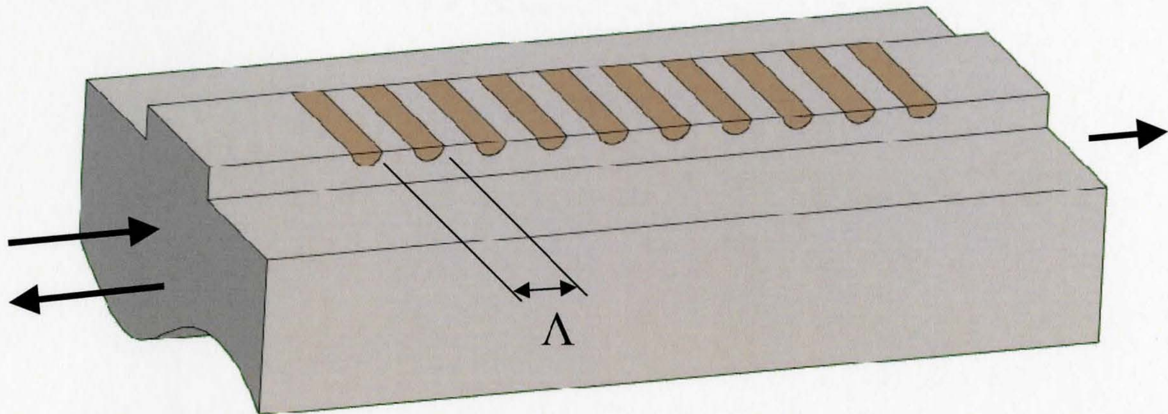

Figure 2.9 Ion implanted Bragg grating. Grating with period Λ formed through selective ion implantation. Under Bragg condition the grating can couple forward-propagating mode to backward-propagating mode.

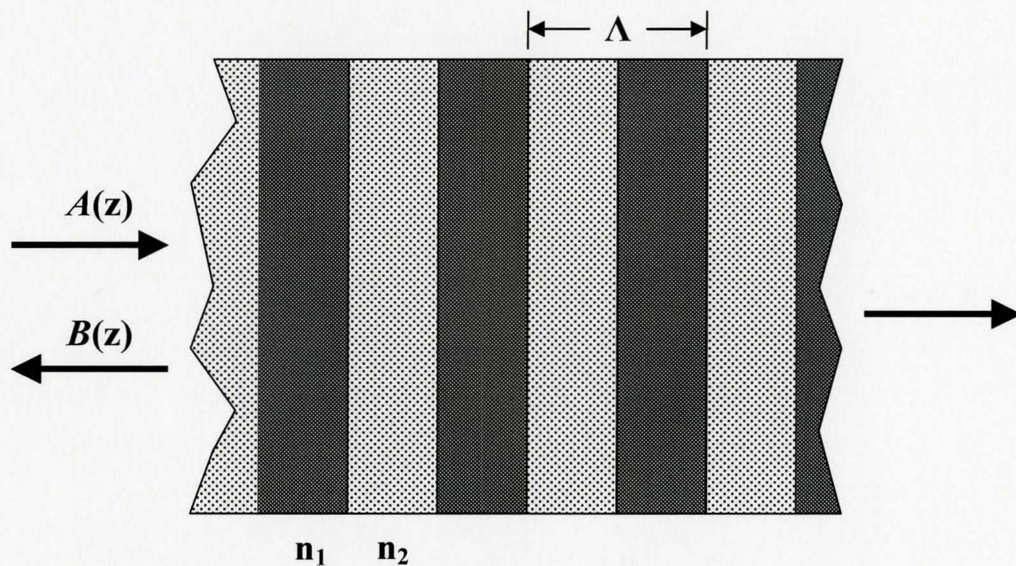

Figure 2.10 Integrated Bragg grating conceptualized as a dielectric stacked mirror with period Λ.

Although diffraction based, it is convenient to consider the structure as a one-dimensional specular reflector as shown in Figure 2.10. The light reflected from consecutive interfaces must interfere constructively. For incident light with vacuum wavelength λ_o, this means the Bragg period Λ must adhere to the condition:

$$\Lambda = \frac{m\lambda_o}{2n_{eff}}, \tag{2.36}$$

where n_{eff} is the effective index of the mode and is dependent on the material and the waveguide structure, and m is a positive integer that represents the order of the Bragg grating. When considering reflections from an interface, the diffraction order is inconsequential. However, being a diffractive device, the efficiency depends on the diffraction order, with first-order diffraction generally being the strongest. Therefore, this work is primarily concerned with first-order (m = 1) Bragg gratings. Setting m = 1 in Equation (2.36), we can determine the required grating period for different wavelengths and materials. Since one of the main goals of silicon photonics is the proliferation of integrated optical components for telecom applications, we are mainly interested in wavelengths in the area of 1550 nm. By approximating the effective index of waveguide modes in silicon to 3.5 and using Equation (2.36), the required period is approximately 220 nm. Using conventional photolithographic techniques it can be difficult to achieve these small dimensions. For this reason it is sometimes beneficial to produce higher order Bragg gratings to simplify the fabrication process, although this work only examines first-order gratings.

2.3.2 Grating Modelling and Contradirectional Coupled Mode Theory

When theoretically modelling a Bragg grating it can be beneficial to examine situations that exhibit similar phenomena. Perhaps the best example of this is the Floquet-Bloch Theorem applied to electrons propagating in a crystalline solid. This method involves describing the electronic waves as Bloch waves, with their periodicity governed by the crystal structure. Indeed, these methods have been employed previously to find exact solutions for the propagation of electromagnetic radiation in Bragg gratings [96, 97]. In many cases, where only approximate solutions to Maxwell's equations exist, this formulism unravels. Numerical solutions can still be found through rigorous finite-difference time-domain algorithms, although they tend to be computationally impractical.

A better method treats the periodic variation of the dielectric constant as a perturbation to an otherwise z-invariant unperturbed structure. This is known as coupled mode theory and is the most common way to analyze Bragg gratings [41, 98-100]. Coupled mode theory solves for the orthogonal set of modes of an unperturbed structure and predicts the coupling between these modes as a result of a perturbation. Thus, the objective of coupled mode theory is to express the overall modes of the perturbed structure, by the superposition of coupled modes from the unperturbed structure. The best approach to constructing the unperturbed structure is through the additional layer method (ALM), which will be discussed hereafter. To account for arbitrarily shaped gratings, the extended additional layer method (EALM) was derived and takes into account both the longitudinal and lateral directions [101]. Other modelling methods,

which will not be discussed in this work, include the ray optics determination [102] and effective index/impedance matching techniques [103].

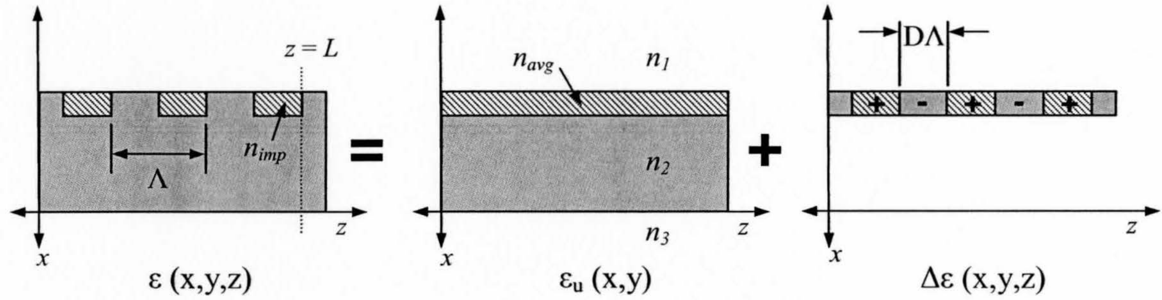

Figure 2.11 Depiction of the ALM used to decompose the implanted Bragg grating into unperturbed and perturbed regions. Here, ε(x,y,z) represents the complete structure, ε_u(x,y) is the unperturbed structure and Δε(x,y,z) is the perturbation.

Figure 2.11 depicts the decomposition of the implanted grating into an unperturbed waveguide and a perturbation function. Here, n_{avg} is the *z*-averaged refractive index, n_{imp} is the refractive index of the implant, and *D* is the percent duty cycle of the unimplanted material. Accordingly, the dielectric tensor of the full structure as a function of space can be written as

$$\varepsilon(x,y,z) = \varepsilon_u(x,y) + \Delta\varepsilon(x,y,z) \tag{2.37}$$

where $\varepsilon_u(x,y)$ is the unperturbed part of the dielectric tensor and $\Delta\varepsilon(x,y,z)$ is the dielectric perturbation, which is periodic in the *z* direction and congruent with the grating periodicity. The perturbation is non-zero only in the grating region.

For the *z*-invariant unperturbed dielectric waveguide, the normal modes of propagation can be expressed as

$$E(x,y,z,t) = E_m(x,y)e^{i(\omega t - \beta_m z)} \tag{2.38}$$

where β_m is the propagation constant, m is the mode index and $E_m(x,y)$ is the wave function of the mth mode. The propagation constants can be solved for using the methods discussed in Sections 2.1.2 and 2.1.3 and each normal mode satisfies the modified wave equation,

$$\left(\frac{\partial^2}{\partial x^2} + \frac{\partial^2}{\partial y^2} + \omega^2 \mu \varepsilon_u(x,y) - \beta_m^2 \right) E_m(x,y) = 0 \tag{2.39}$$

Provided the normal modes form a complete basis set, if any arbitrary field is excited at $z = 0$, the propagation of this field within the unperturbed waveguide can be expressed as a linear superposition of normal modes:

$$E = \sum_m A_m E_m(x,y) e^{i(\omega t - \beta_m z)} \tag{2.40}$$

where A_m are the modal expansion coefficients and the summation covers all existing modes.

If an arbitrary mode $E_1(x,y)e^{i(\omega t - \beta_1 z)}$ defined by the unperturbed waveguide is subject to the perturbation at $z = 0$, it is now influenced by the dielectric tensor $\varepsilon(x,y,z) = \varepsilon_u(x,y) + \Delta\varepsilon(x,y,z)$. The effect of the perturbation $\Delta\varepsilon(x,y,z)$ is to produce an additional polarization of the electronic oscillators. This can be expressed as:

$$\Delta P = \Delta\varepsilon(x,y,z) E_1(x,y) e^{i(\omega t - \beta_1 z)} \tag{2.41}$$

Physically, the effect of this additional polarization is to act as a distributed radiating source. Under proper conditions it is then possible for the induced source to transfer

energy from one mode and feed it into another mode, say $E_2(x,y)e^{i(\omega t-\beta_2 z)}$. This is the premise of mode coupling.

It is still possible to express the overall electric field as a linear summation of the unperturbed modes, however mode coupling must now be taken into account. When the waves are influenced by the perturbation, the modes $E_m(x,y)e^{i(\omega t-\beta_m z)}$ cease being eigenmodes and the modal expansion coefficients become z dependent. The E-field in the perturbed waveguide can be expressed as:

$$E=\sum_m A_m(z)E_m(x,y)e^{i(\omega t-\beta_m z)} \tag{2.42}$$

where the z dependence of the expansion coefficients $A_m(z)$ accounts for the coupling between orthogonal modes. Equation (2.42) now describes the evolution of the scalar coefficients $A_m(z)$ in the propagation direction z. As will be shown, coupled mode theory replaces Maxwell's equations for E and H by a set of coupled ordinary linear differential equations.

Substituting Equation (2.42) into the wave equation

$$\left[\nabla^2+\omega^2\mu\left(\varepsilon_u(x,y)+\Delta\varepsilon(x,y,z)\right)\right]E=0 \tag{2.43}$$

and using Equation (2.39) we obtain,

$$\begin{aligned}\sum_m\left(\frac{d^2}{dz^2}A_m-2i\beta_m\frac{d}{dz}A_m\right)E_m(x,y)e^{i(\omega t-\beta_m z)}= \\ -\omega^2\mu\sum_n\Delta\varepsilon(x,y,z)A_nE_n(x,y)e^{i(\omega t-\beta_n z)}\end{aligned} \tag{2.44}$$

To simplify Equation (2.44), we make use of the slowly varying amplitude approximation (SVA). The approximation is valid when the perturbation is considered weak, resulting

in an energy transfer between modes over distances that are long relative to the period of light. Mathematically it is expressed as:

$$\frac{d^2 A_m}{dz^2} \square \beta_m \frac{dA_m}{dz} \tag{2.45}$$

This tends to be a suitable approximation when the perturbation is small. Neglecting the second-order derivative in Equation (2.44) results in

$$-2i\sum_m \beta_m \left(\frac{d}{dz} A_m\right) E_m(x,y) e^{-i\beta_m z} = -\omega^2 \mu \sum_n \Delta\varepsilon(x,y,z) A_n E_n(x,y) e^{-\beta_n z} \tag{2.46}$$

where the time-varying component has been removed. To isolate for the modal coefficients we make us of the orthogonality properties discussed in Section 2.1.6. Taking the dot product of Equation (2.46) with $E_k^*(x,y)$ and integrating over all x and y leads to the retention of the kth mode only on the left-hand side. Using the orthogonality property of the modes (2.30) the result is

$$\left(\frac{2\omega\mu}{|\beta_k|}\right) \frac{d}{dz} A_k = \frac{\omega^2 \mu}{2i\beta_k} \sum_n \left(\int E_k^* \cdot \Delta\varepsilon(x,y,z) E_n dxdy \right) A_n(z) e^{i(\beta_k - \beta_n)z} \tag{2.47}$$

For a periodic medium the perturbation can be expanded as a Fourier series in z as

$$\Delta\varepsilon(x,y,z) = \sum_{m\neq 0} \Delta\varepsilon_m(x,y) \exp\left(-im\frac{2\pi}{\Lambda} z\right) \tag{2.48}$$

where the summation is over all m harmonics except $m = 0$ because it is already accounted for in Equation (2.37) as $\varepsilon_u(x,y)$. Substituting Equation (2.48) into Equation (2.47) leads to

$$\frac{d}{dz} A_k = -i\frac{|\beta_k|}{\beta_k} \sum_m \sum_n \kappa_{kn}^{(m)} A_n(z) e^{i\left(\beta_k - \beta_n - m\frac{2\pi}{\Lambda}\right)z} \tag{2.49}$$

where $\kappa_{kn}^{(m)}$ is called the coupling coefficient and is given by

$$\kappa_{kn}^{(m)} = \frac{\omega}{4} \int E_k^* \cdot \Delta\varepsilon_m(x,y) E_n dxdy \tag{2.50}$$

The coupling coefficient is a measure of the strength of the coupling between modes *k* and *n* due to the *m*th Fourier component of the perturbation. Equation (2.50) is just a simple overlap integral between the *k*th mode and the *n*th mode over the grating region, since this is the only location the perturbation is nonzero.

Equation (2.49) represents a complete set of coupled ordinary linear differential equations and accounts for the coupling between an infinite set of modes. In practise, however, we are generally concerned with single mode waveguide structures and Equation (2.49) is reduced to a set of two equations relating two *z*-dependent modal amplitudes.

There are two conditions that must be satisfied to elicit substantial mode coupling. The first is known as the phase matching condition and is dictated by the phase component of Equation (2.49).

$$\beta_k - \beta_n - m\frac{2\pi}{\Lambda} = 0 \tag{2.51}$$

Equation (2.51) states that resonant coupling occurs when the two modes with propagation constants β_k and β_n are related to each other by $m\frac{2\pi}{\Lambda}$. Graphically, this can be expressed as shown in Figure 2.12.

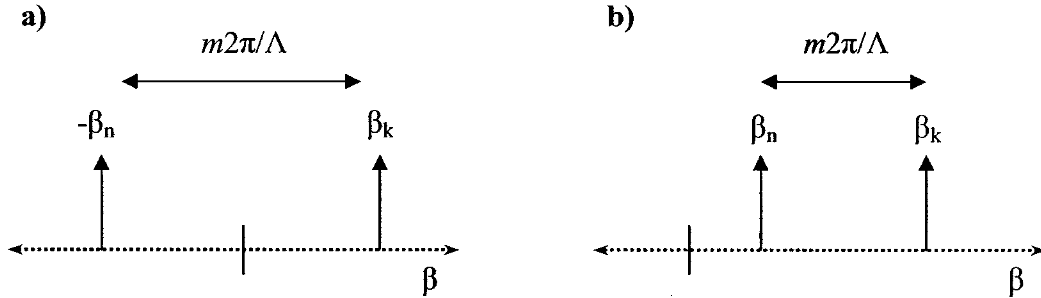

Figure 2.12 Phase matching condition between modes for a) contradirectional coupling and b) codirectional coupling

To understand the effects of phase matching, consider the increment of the kth modal coefficient dA_k in the region between z and $z + dz$, due to mode coupling with the nth mode via the mth Fourier component of the perturbation. This incremental effect can be expressed as

$$dA_k = -i\frac{|\beta_k|}{\beta_k}\kappa_{kn}^{(m)}A_n(z)e^{i\left(\beta_k-\beta_n-m\frac{2\pi}{\Lambda}\right)z}dz \tag{2.52}$$

Knowing that the modal amplitudes vary slowly as a function of space, Equation (2.52) can be integrated over a distance L that is larger than Λ, but small enough that the modal coefficients can be considered constant. Under these limits of integration Equation (2.52) can be written as

$$\Delta A_k = -i\frac{|\beta_k|}{\beta_k}\kappa_{kn}^{(m)}A_n\int_L e^{i\left(\beta_k-\beta_n-m\frac{2\pi}{\Lambda}\right)z}dz \tag{2.53}$$

When Equation (2.53) is integrated over the limit $L>>\Lambda$, the integrand vanishes, due its inherent sinusoidal nature, for all coupling between the kth and nth modes when the phase matching condition is not met. The integral is only nonzero when the phase matching condition is met exactly. This serves as an approximation, but demonstrates the stringent

phase matching requirements of coupled modes in periodic media. The second is the coupling coefficient must be nonzero.

In the case of contradirectional mode coupling in a single mode rib waveguide, there exists two propagating modes that can be represented as $AE_0(x,y)e^{i(\omega t-\beta_0 z)}$ for the forward travelling mode and $BE_0(x,y)e^{i(\omega t+\beta_0 z)}$ for the backward travelling mode. The coupled equations (2.49) are reduced to

$$\begin{aligned} \frac{d}{dz}A &= -i\kappa B(z)e^{i\Delta\beta z} \\ \frac{d}{dz}B &= i\kappa^* A(z)e^{-i\Delta\beta z} \end{aligned} \tag{2.54}$$

where $\kappa = \kappa_{00}^{(m)}$ and $\Delta\beta = \beta_0 - (-\beta_0) - m\frac{2\pi}{\Lambda}$. It can be shown that $\kappa_{00}^{(m)} = \left[\kappa_{00}^{(-m)}\right]^* = \kappa$ provided the perturbation tensor is Hermitian. The reflectivity per unit length of the grating depends directly on κ and its calculation is explored hereafter.

2.3.3 The Coupling Coefficient and Grating Strength

As previously mentioned, the implanted grating structure of Figure 2.11 can be decomposed into unperturbed $\varepsilon_u(x,y)$ and perturbed $\Delta\varepsilon(x,y,z)$ constituents. The dielectric permeability is related to the index of refraction through

$$\varepsilon(x,y) = \varepsilon_o n^2(x,y) \tag{2.55}$$

Using Equation (2.55), the unperturbed region can represented by a piecewise function as

$$\varepsilon_u(x,y) = \begin{cases} \varepsilon_o\left(Dn_2^2 + (1-D)n_{imp}^2\right) & grating \\ \varepsilon_o n^2(x,y) & elsewhere \end{cases} \tag{2.56}$$

where the dielectric permeability over the grating region is just the *z*-averaged index of refraction and *D* is the duty cycle of the non-implanted region. Similarly, assuming a square implanted region, the perturbation can be expressed as

$$\Delta\varepsilon(x,y,z) = \begin{cases} \varepsilon_o\left(n_2^2 - n_{imp}^2\right)\sum_{m=-\infty}^{\infty} b_m \exp\left(-im\frac{2\pi}{\Lambda}z\right) & grating \\ 0 & elsewhere \end{cases} \tag{2.57}$$

where b_m are the Fourier coefficients of the *z*-periodic perturbation. As an approximation, the perturbation has been reduced to a square wave of unitary amplitude and the Fourier coefficients can be computed as

$$b_m = \frac{\sin(m\pi D)}{m\pi} \tag{2.58}$$

The $z = 0$ origin was arbitrarily centered on a grating tooth, producing only real Fourier coefficients. It is worth mentioning that with the choice of the z-averaged additional layer in the unperturbed structure, the $m = 0$ coefficient approaches zero because the 'DC' component has already been accounted for. Substituting Equation (2.57) into Equation (2.50), the coupling coefficient for the single mode rib waveguide can be found through

$$\kappa_{00}^{(m)} = \frac{\omega\varepsilon_o}{4m\pi}\sin(m\pi D)\iint_{grating} E_0^* \cdot (n_2^2 - n_{imp}^2)E_0\,dxdy \tag{2.59}$$

Therefore, Equation (2.59) can be used to solve the coupling coefficient for each *m*th harmonic of the perturbation and using superposition the result of each harmonic on the mode coupling can be summed using Equation (2.49) to find the final result. To simplify

calculations it is common practise to retain only the first Fourier coefficient [100]. This is generally a valid approximation because the perturbation acts as a driving oscillator for the backward-travelling modes and its first harmonic coincides closest with the fundamental backward-travelling mode. Also, the implanted grating profiles generated in Section 2.2.3 show an almost sinusoidal nature, meaning the higher order Fourier coefficients will be negligible and will not contribute appreciably to the coupling. Generally, these approximations hold closer to reality for a 50/50 duty cycle when the first Fourier coefficient is maximized, however due to computational simplifications the approximations are assumed for alternative duty cycles as well.

Since the strength of the grating response is directly related to the degree of overlap between the grating and the mode profile, care must be employed to ensure rib dimensions are chosen to produce adequate grating strength. In the case of implanted Bragg gratings it was found in Section 2.2.3 that the maximum implant depth is on the order of 150 nm. Using a simple slab waveguide structure as an approximation, the reflected grating strength was computed as a function of the silicon device layer height using a simplified CMT approach. The results are plotted in Figure 2.13.

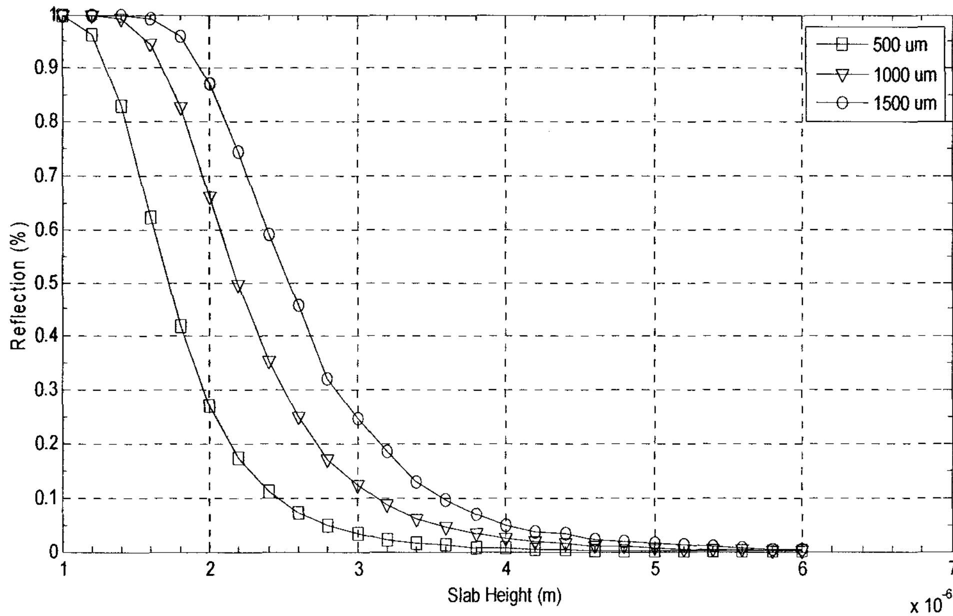

Figure 2.13 Maximum reflected power versus the silicon device layer height.

Figure 2.13 shows the maximum reflected power as a function of the slab waveguide height assuming an implanted grating height of 100 nm for grating lengths of 500, 1000, and 1500 μm. Slab heights greater than approximately 2 μm lead to a large reduction in the maximum reflected power for even the largest grating length. Since integrated grating lengths are typically on the order of a few thousand microns, and coupling losses increase as the slab height decreases, SOI with a silicon device layer height of approximately 2 μm will provide adequate modal overlap.

To compute the coupling coefficients of the Bragg grating, the BPM iterative mode solver technique was implemented to determine the mode profile of the fundamental mode for the unperturbed rib waveguide. The SOI device layer height was assumed to have a height of 2.5 μm, while a 0.8 μm etch depth of the rib was assumed to ensure single mode operation. The effect of varying the duty cycle was investigated by

altering the index of refraction of the additional layer of the unperturbed structure, which is merely the z-averaged value as define in Equation (2.56). Substituting the fundamental modes for TE and TM polarizations into Equation (2.59), the coupling coefficient κ as a function of duty cycle $1 - D$ was computed for various implant depths and is illustrated in Figure 2.14. The duty cycle plotted represents the percentage of the teeth composed of implanted material.

Figure 2.14 depicts some interesting effects of the duty cycle $1 - D$ on the coupling strength. First, the TE and TM modes display substantial polarization dependence. That is, the coupling coefficient for TE polarization at a particular duty cycle is much larger than the corresponding TM polarization for the same implant depth. This is a result of TE mode possessing a larger modal overlap with the grating region relative to the TM mode. Indeed, Figure 2.15 shows the confinement factor of the TE and TM modes with the grating region for a 50/50 duty cycle and 20/80 duty cycle while varying the implant depth.

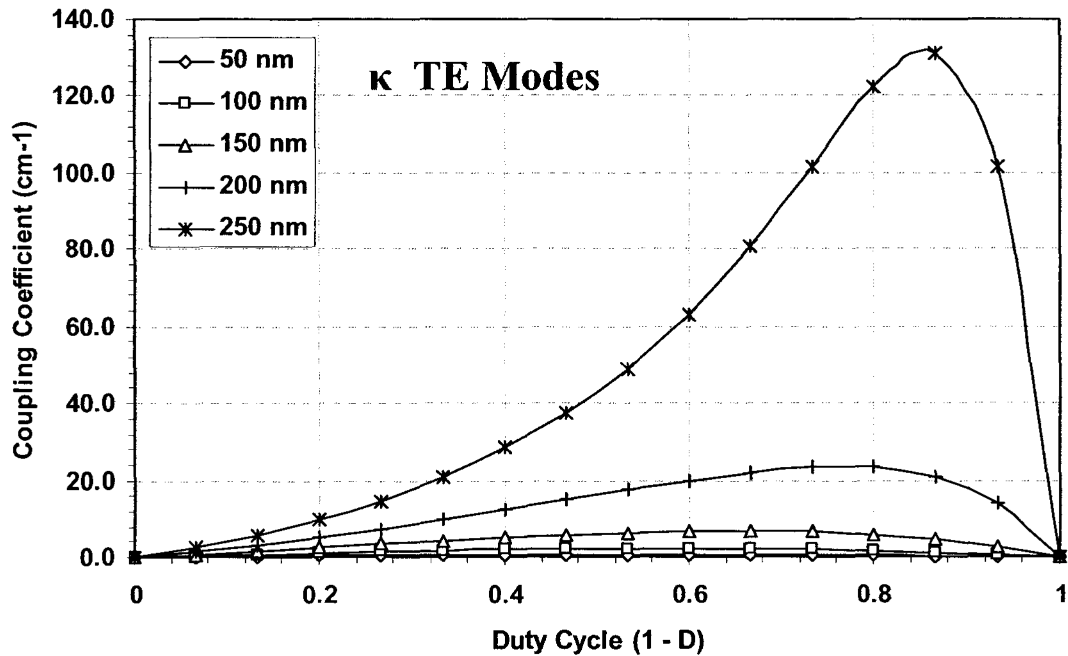

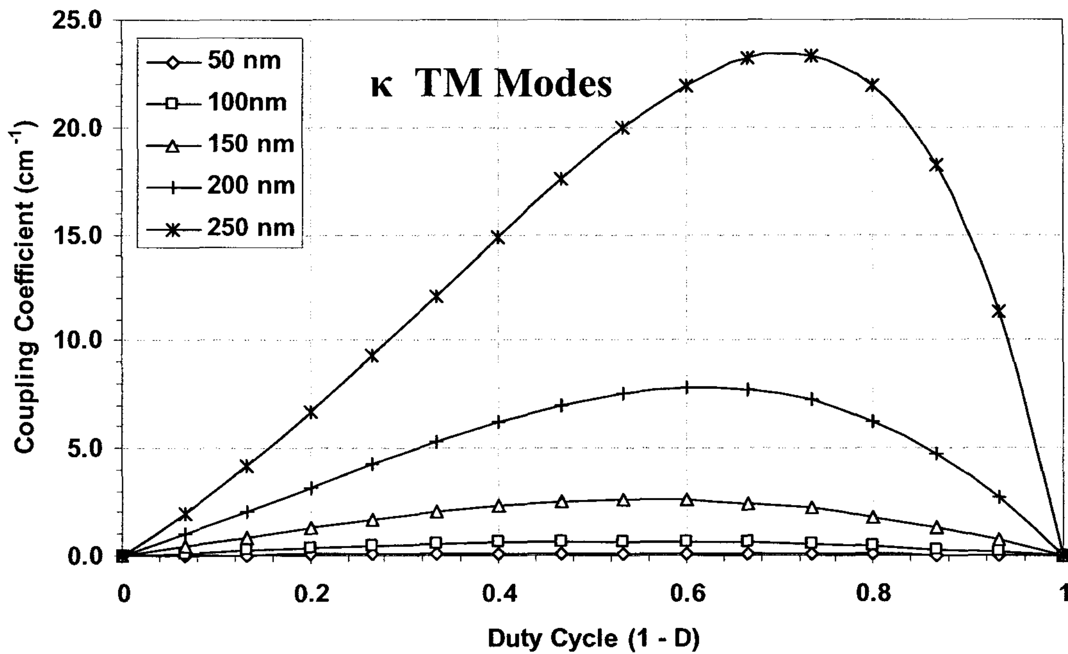

Figure 2.14 Calculated coupling coefficient κ vs. duty cycle 1 - D for implanted Bragg gratings of depth 50 to 250 nm in an SOI ridge waveguide for TE and TM.

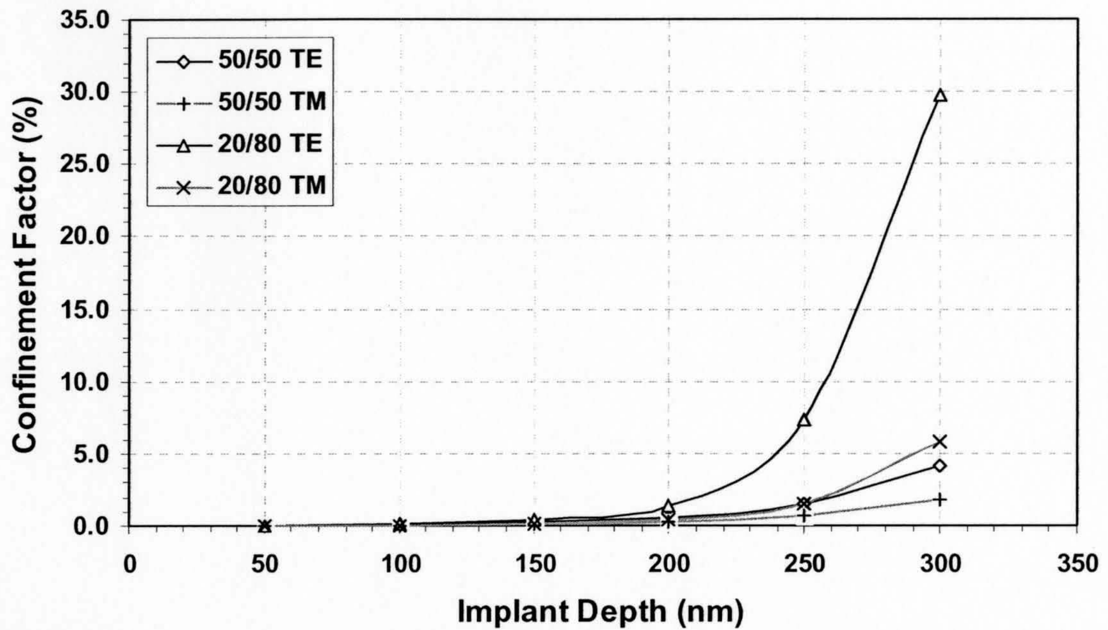

Figure 2.15 Modal confinement of TE and TM modes versus implant depth for 50/50 duty cycle and 20/80 duty cycle.

Also of interest, the maximum coupling coefficient shifts away from a 50/50 duty cycle as the implant depth increases. This can be attributed to the preferential mode-shifting of the light towards the higher index of refraction of the implanted region. Figure 2.16 illustrates the calculated mode profiles for an implant depth of 250 nm for TE polarization and duty cycles [$D/(1-D)$] of 40/60 and 20/80.

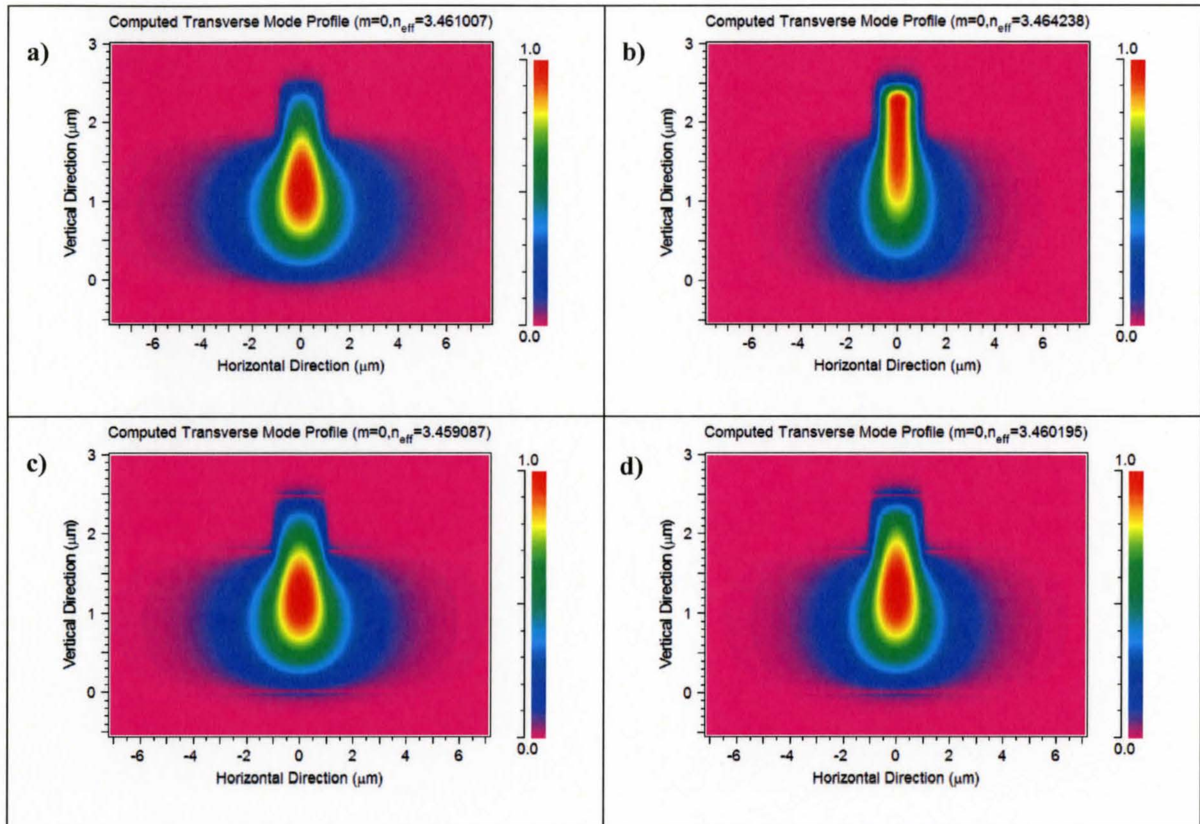

Figure 2.16 Mode profiles for implant depth of 250nm for a) TE polarization with 40/60 duty cycle, b) TE polarization with 20/80 duty cycle, c) TM polarization with 40/60 duty cycle and d) TM polarization 20/80 duty cycle.

Mode-shifting depends significantly on the thickness of the implanted layer and for sufficient implant thicknesses the light will be confined primarily in the implanted layer, in agreement with total internal reflection. This explains the abrupt increase in the coupling coefficient in Figure 2.14 between the 200 and 250 nm implants. The 250 nm implant elicits substantial mode-shifting and causes a dramatic increase of the mode overlap with grating region. The end result is a much larger coupling coefficient, leading to a reduction in the required coupling length. For high density silicon photonics components this is beneficial, however since the implanted region is lossy, a trade off

exists between increased coupling strength and increased loss. This will be explored further in the following sections.

2.3.4 Grating Spectral Response and Gratings with Loss

One of the fundamentally important characteristics of Bragg gratings is their high degree of frequency dependence. To explore the spectral response of the ion implanted grating, Equation (2.54) must be solved as a function of frequency.

In the previous section mode profiles were calculated to determine the coupling coefficient at one particular frequency. In order to compute the spectral response over a predetermined frequency range the process would have to be carried through for all frequencies. Unlike the one-dimensional case, this can be a very impractical approach for two-dimensional structures such as the rib waveguide. Fortunately, mode profiles tend to exhibit minimal variance over the relatively small bandwidth of interest. Therefore, it usually suffices to treat the mode profile as constant and simply alter the propagation constant β according to the change in frequency.

The phase matching condition is given by

$$\Delta\beta = \beta - (-\beta) - m\frac{2\pi}{\Lambda} = 2(\beta - \beta_o) \tag{2.60}$$

where $\beta_o = m\pi / \Lambda$. The effective index of the mode can be defined such that

$$\beta = n_{eff}\frac{\omega}{c} = n_{eff}\frac{2\pi}{\lambda} \tag{2.61}$$

For contradirectional coupling the phase matching condition can now be written as

$$\Delta\beta = 2\beta - m\frac{2\pi}{\Lambda} = \frac{2n_{eff}}{c}(\omega - \omega_o) \tag{2.62}$$

where ω_o is the center frequency where the phase matching condition is satisfied and ω is the operating frequency. We now have a direct relationship between the phase matching condition and the deviation from the resonant wavelength. To find the spectral response the coupled equations (2.54) must be solved. The general solutions are

$$\begin{aligned} A(z) &= C_1 e^{i(\Delta\beta/2)z - sz} + C_2 e^{i(\Delta\beta/2)z + sz} \\ B(z) &= \frac{i}{\kappa}\frac{d}{dz}A(z) \end{aligned} \tag{2.63}$$

where C_1 and C_2 are constants and s is defined as

$$s = \sqrt{|\kappa|^2 - [\beta(\omega) - \beta_o]^2} \tag{2.64}$$

To solve Equation (2.63) we must impart the boundary conditions relevant to the implanted grating structure. Assuming the grating region extends from $z = 0$ to $z = L$, the light in the forward travelling mode at the input of the grating ($z = 0$) is expressed as $A(0)$. Furthermore, at end of the grating ($z = L$) it is assumed that there exists no backward-travelling mode $B(L) = 0$. Implementing these boundary conditions the particular solutions are

$$\begin{aligned} A(z) &= e^{i(\Delta\beta/2)z}\frac{s\cosh[s(L-z)] + i(\Delta\beta/2)\sinh[s(L-z)]}{s\cosh(sL) + i(\Delta\beta/2)\sinh(sL)}A(0) \\ B(z) &= e^{-i(\Delta\beta/2)z}\frac{-i\kappa^{*}\sinh[s(L-z)]}{s\cosh(sL) + i(\Delta\beta/2)\sinh(sL)}A(0) \end{aligned} \tag{2.65}$$

The result is two equations dictating the forward propagating $A(z)$ and backward propagating $B(z)$ modal coefficients at any point z in the grating region. The reflection efficiency of the Bragg grating can be calculated through

$$R = \left|\frac{B(0)}{A(0)}\right|^2 = \frac{|\kappa|^2 \sinh^2(sL)}{s^2\cosh^2(sL) + (\Delta\beta/2)^2 \sinh^2(sL)} \tag{2.66}$$

Maximum reflectance occurs when $\Delta\beta = 0$, and Equation (2.66) simplifies to

$$R_{\max} = \tanh^2(|\kappa|L) \tag{2.67}$$

In agreement with intuition, the reflectance is an increasing function of $|\kappa|L$. Also, assuming lossless gratings, conservation of energy requires

$$R + T = 1 \tag{2.68}$$

where T is the defined as the transmittance.

Equation (2.65) describes the case where the perturbation is real valued and does not take into account medium gain or loss. For ion implanted gratings, the situation is a bit more complicated as the implantation process introduces loss in the medium. Since Bragg gratings are of paramount importance in distributed feedback lasers, numerous methods have been investigated to explain gain and loss mechanisms in periodic media [104-106].

To start off, we assume the refractive index perturbation and the complex refractive index perturbation follow the same square wave approximation stated previously. Taking into account loss, the dielectric perturbation can be expressed as

$$\Delta\varepsilon(x,y,z) = \varepsilon_o \Delta n^2 + i\frac{2\Delta\gamma\Delta n}{k_o} \tag{2.69}$$

where $\Delta\gamma$ is the exponential loss coefficient and by convention γ is negative to represent material loss [41]. Knowing that each periodic perturbation follows the same square

wave function, the z-dependence can be factored and expanded as a Fourier series to become

$$\Delta\varepsilon(x,y,z)=\varepsilon_o\left[\left(\Delta n^2\right)+i\frac{2\Delta\gamma\Delta n}{k_o}\right]\sum_{m=-\infty}^{\infty}b_m\exp\left(-im\frac{2\pi}{\Lambda}z\right) \tag{2.70}$$

Substituting back into Equation (2.47), the coupling coefficient becomes

$$\kappa_{00}^{(m)}=\frac{\omega\varepsilon_o}{4m\pi}\sin(m\pi D)\left((\Delta n^2)+i\frac{2\Delta\gamma\Delta n}{k_o}\right)\iint_{grating}E_0^*\cdot E_0dxdy \tag{2.71}$$

where $\Delta\gamma=\gamma_2-\gamma_{imp}$. It is noted that in the calculation, the unperturbed waveguide modes were computed ignoring any loss that exists in the waveguide. From the equation we see that the effect of the implanted damage is to introduce a complex coupling coefficient. The result is that gain/loss coupling can occur and serves as the principle behind gain-coupled distributed feedback lasers.

In addition to the coupling coefficients, we must account for loss in the coupled equations (2.54). Adding loss components to the equation results in

$$\begin{aligned}\frac{d}{dz}A&=-i\kappa B(z)e^{i2\Delta\beta z}+\gamma_u A\\ \frac{d}{dz}B&=i\kappa^*A(z)e^{-i2\Delta\beta z}-\gamma_u\beta\end{aligned} \tag{2.72}$$

where γ_u is the modal loss of the propagating mode due to the ion-induced damage. It is easy to show that when the coupling coefficient vanishes the solutions exponentially decay as expected. The solutions can be found very easily provided we make the substitution

$$A(z) = A'(z)e^{\gamma_u z}$$
$$B(z) = B'(z)e^{-\gamma_u z} \tag{2.73}$$

Equation (2.72) now becomes

$$\frac{d}{dz}A'(z) = -i\kappa B'(z)e^{i2(\Delta\beta + i\gamma_u/2)z}$$
$$\frac{d}{dz}B'(z) = i\kappa^* A'(z)e^{-i2(\Delta\beta + i\gamma_u/2)z} \tag{2.74}$$

This is the exact form of the coupled equations determined previously and solutions can be readily computed provided we replace $\Delta\beta$ with $2(\Delta\beta + i\gamma_u/2)$. These solutions are given by

$$A(z) = e^{i(\Delta\beta/2)z}\frac{s\cosh[s(L-z)] + i(\Delta\beta + i\gamma_u/2)\sinh[s(L-z)]}{s\cosh(sL) + i(\Delta\beta + i\gamma_u/2)\sinh(sL)}A(0)$$
$$B(z) = e^{-i(\Delta\beta/2)z}\frac{-i\kappa^*\sinh[s(L-z)]}{s\cosh(sL) + i(\Delta\beta + i\gamma_u/2)\sinh(sL)}A(0) \tag{2.75}$$

here s is given by

$$s^2 = |\kappa|^2 + (\gamma_u/2 - i\Delta\beta)^2 \tag{2.76}$$

Assuming an implant depth of 150 nm the reflected and transmitted spectra are plotted versus the deviation from the phase matching condition $\Delta\beta$ in Figure 2.17. The absorption losses were estimated based on experimental results obtained and will be discussed in the following chapters. The estimated value of the modal loss for the unannealed 50 keV implant was $\gamma_u = 2.05$ cm^{-1} and the modal loss for the 60 keV implant was $\gamma_u = 2.76$ cm^{-1}.

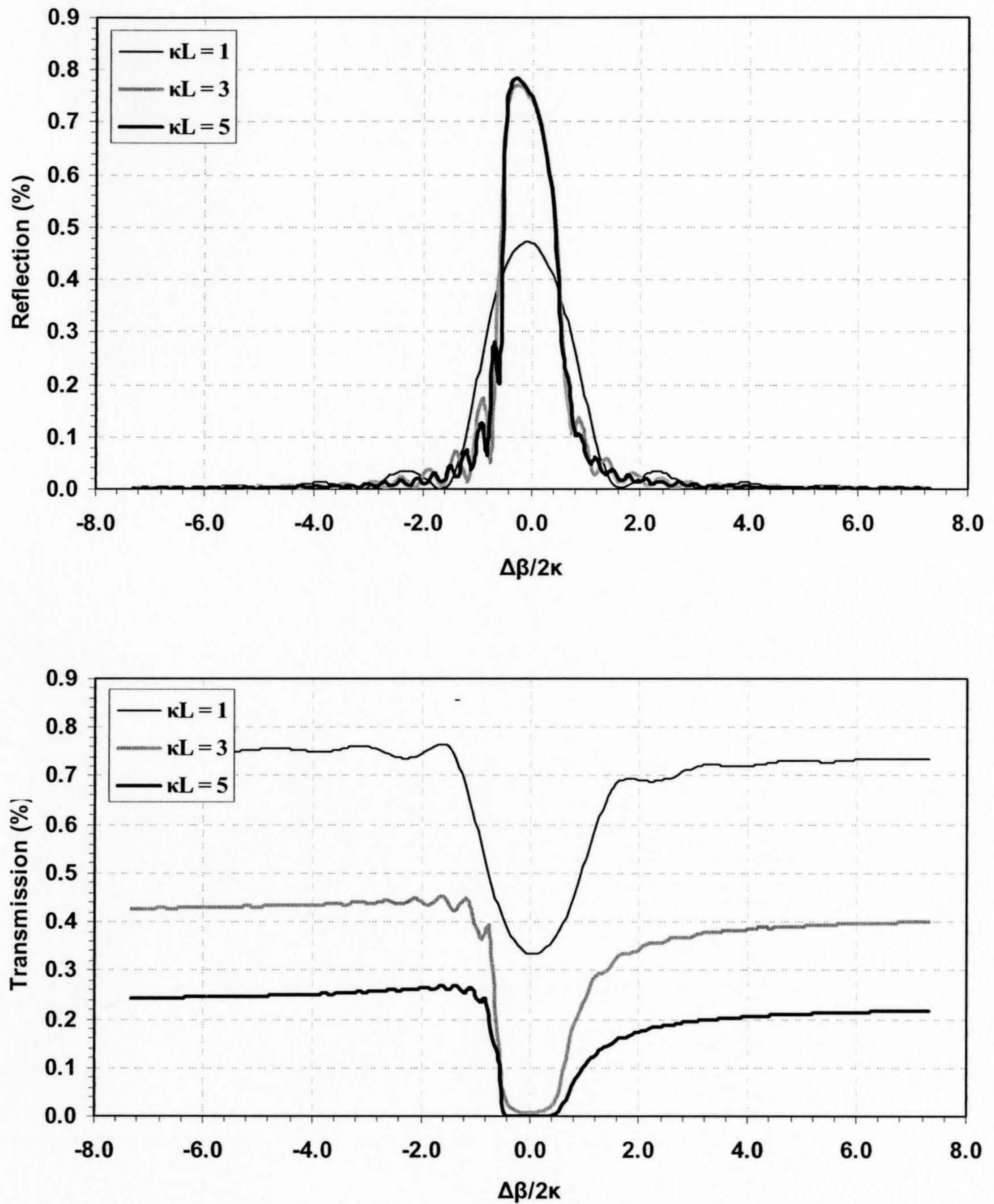

Figure 2.17 Calculated reflected and transmitted spectra for three Bragg gratings of increasing length

Figure 2.17 illustrates the characteristic dip at the resonant wavelength expected from a waveguide Bragg grating structure and depicts the effect of the lossy medium. As previously mentioned the grating strength is an increasing function of $|\kappa|L$ and in the event of a lossless medium the strength eventually saturates to a reflected value approaching one hundred percent. However, in the event of absorption loss, the maximum reflected power saturates to a value that is only a fraction of the input power. In the case illustrated, the maximum reflected power saturates at approximately eighty percent of the input power. Increasing the length L of the grating further only has the effect of deviating from the 'sinc' shaped spectral response to a more 'box-like' response and a resulting squeezing of the sidelobes. As expected, increasing the grating length also has the effect of decreasing the amount of transmitted power. For long gratings a drastic reduction in the transmission occurs. This makes it difficult to discern the transmitted grating shape and it is beneficial to normalize the plots to their respective transmitted powers. This is shown in Figure 2.18 and the trade-off between transmitted power and extinction ratio becomes more evident.

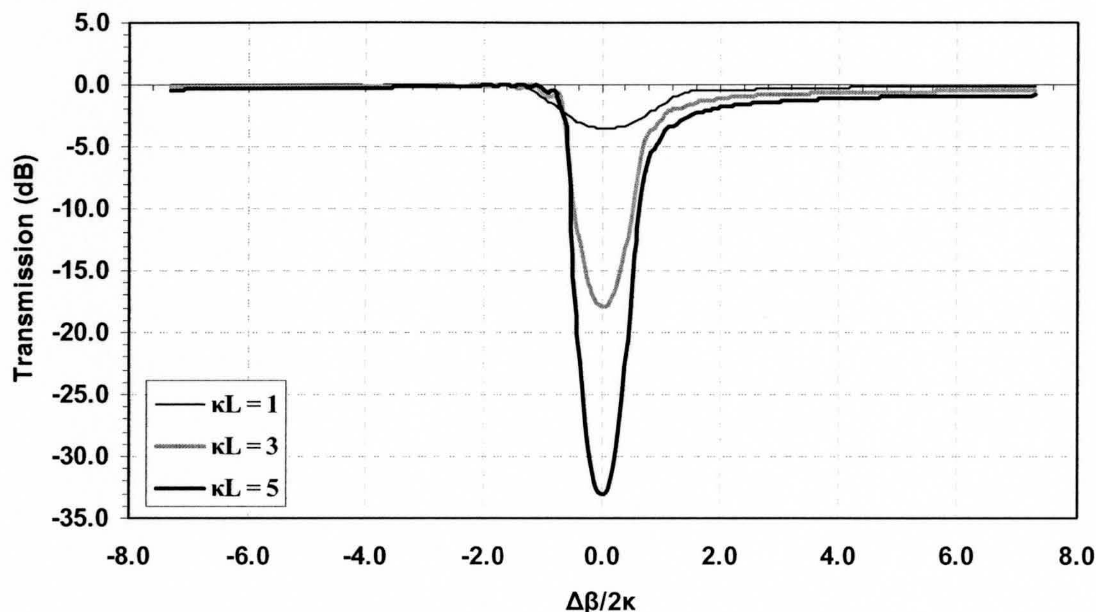

Figure 2.18 Calculated reflected spectrum normalized to transmitted power

To see the effect of the absorption loss on a strong Bragg grating ($\kappa L >> 1$) Figure 2.19 shows the relationship between the reflected spectrum and an increasing absorption coefficient. A dramatic change of the maximum reflected power and a significant variation from the box-like spectral response occurs with an increasing absorption coefficient. Since the modal absorption coefficient is directly related to the implant depth, a deep implant can be detrimental to the shape of the grating response. Therefore, it is very important to minimize the additional loss while maintaining the increased refractive index of the amorphous silicon. One of the best methods to reduce any excess optical absorption is through low temperature annealing to eliminate point defects and other low energy defects which might contribute to absorption. As previously mentioned, bulk losses on the order of 115 cm^{-1} have been achieved after annealing at 500°C for 1

hour while retaining an index increase of approximately 0.3 [51]. This value is approximately five times smaller than the absorption coefficient utilized for the simulations in Figure 2.17. Annealing studies will be described in the following chapters.

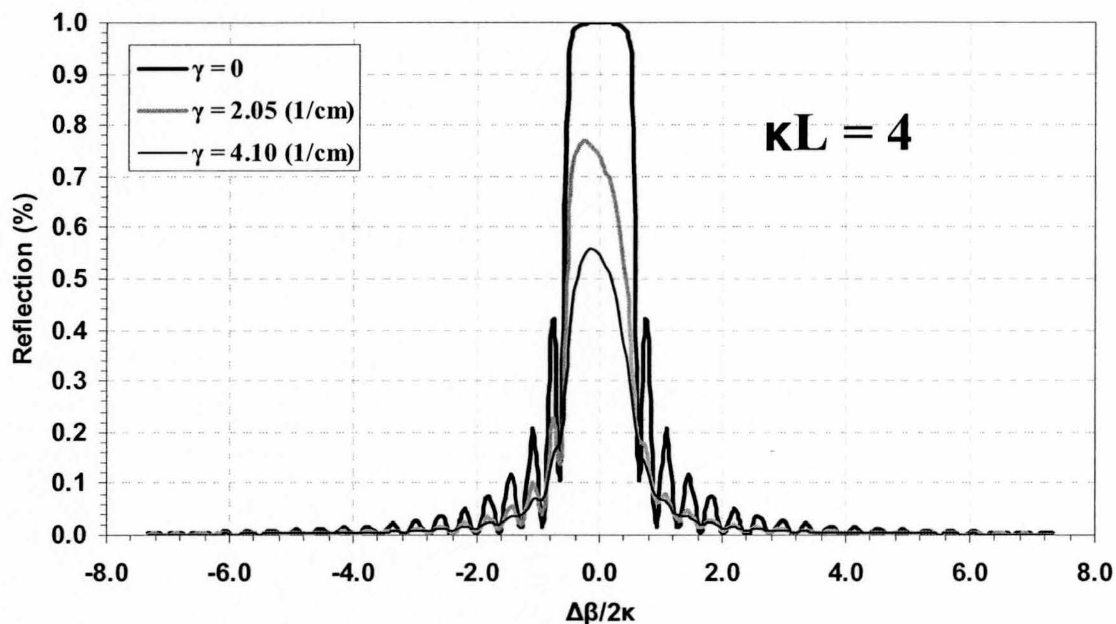

Figure 2.19 Calculated reflected spectrum versus the absorption coefficient for a grating length sufficient for strong reflections.

2.3.5 Propagation Losses Due to Implant

To obtain a general understanding of relationship between the transmitted power and the implanted grating depth, beam propagation simulations were carried out assuming a 50/50 duty cycle and a bulk absorption coefficient in the implanted regions of 115 cm^{-1}, as reported by de Dood *et al.* The results for TE and TM polarizations are presented in Figure 2.20.

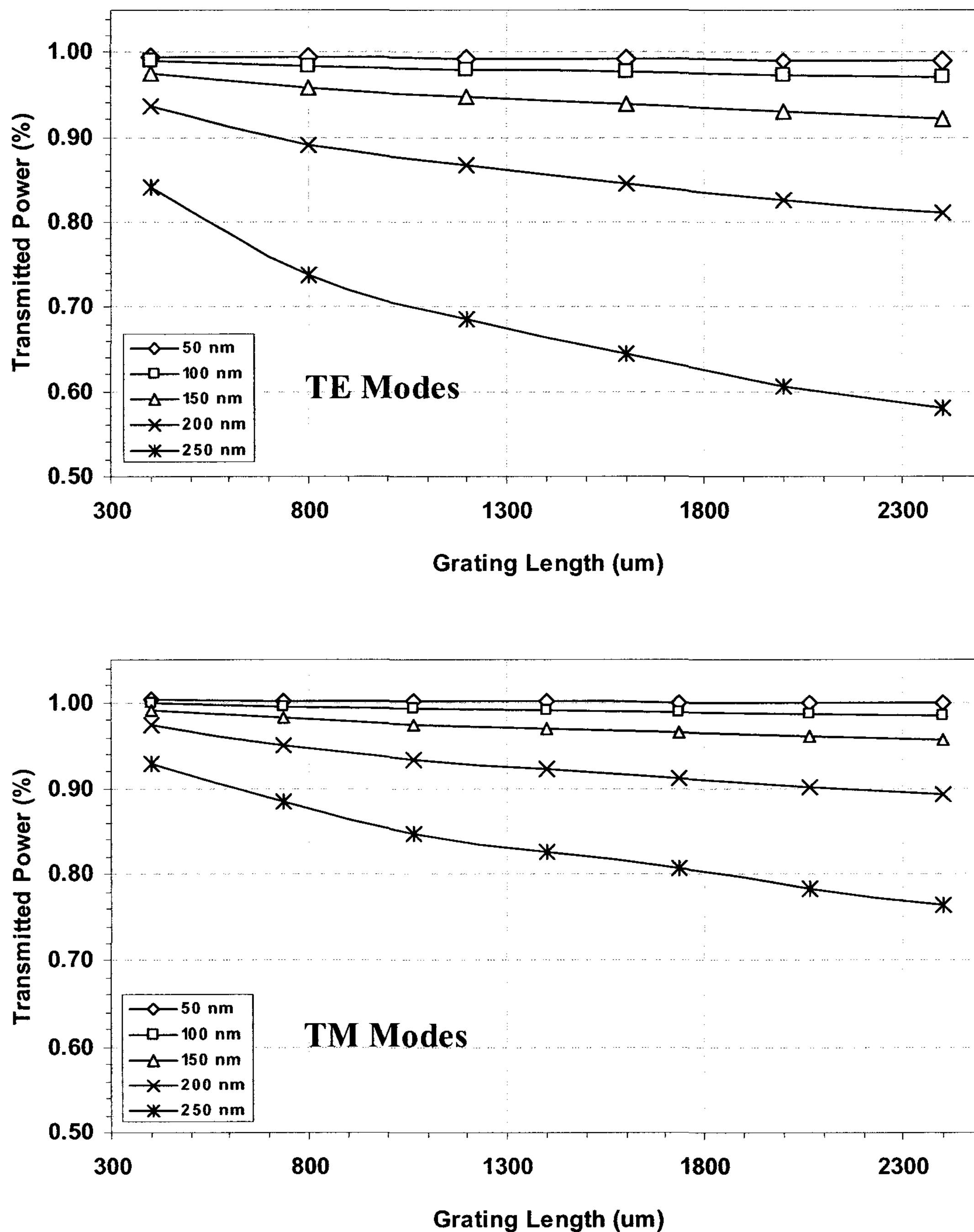

Figure 2.20 Propagation loss versus grating length for TE and TM polarization assuming a 50/50 duty cycle and implant depths ranging from 50 to 100 nm.

TE polarization exhibits preferential absorption with respect to the TM polarization. This agrees with previous observations that computed a higher relative modal confinement of TE modes with the grating region. The figure also shows the precariousness of the relationship. For TE light the difference in transmitted power for grating lengths of 2400 μm and implant depths of 200 and 250 nm is close to thirty percent. Since the grating strength is also strongly dependent on the grating depth it is very important to choose a grating depth that both maximizes the coupling coefficient and minimizes the propagation losses. From the analysis it is clear that grating depths on the order of 150 nm adhere to these restrictions.

Chapter 3

Fabrication

3.1 Fabrication of Silicon Photonic Devices

Relative to other integrated platforms, such as III-V compounds and lithium niobate, processing devices in SOI benefits from the plethora of existing knowledge and facilities established for microelectronic devices. Both well understood and well established processes integral to microelectronic fabrication can be directly implemented in a silicon photonics platform as well.

Originally derived for the electronics industry to reduce parasitic capacitance, SOI wafers are the foundation of silicon photonic applications. As interest in SOI photonics continues to grow, numerous manufacturing methods have been adopted to produce optically smooth SOI wafers that allow for maximum customizability of the silicon overlayer thickness and buried oxide layer thickness. The main methods for manufacturing SOI wafers are separation by oxide implantation (SIMOX), bond and etch-back (BESOI) and Smart-Cut® [107].

The SIMOX process involves a high dose oxygen implantation over the entire wafer resulting in a buried oxygen layer. Upon high temperature annealing (~1300°C) a silicon dioxide layer can be formed [10]. The depth and thickness of the oxide layer are determined, and also limited, by the implantation parameters and profiles.

On the other hand, the BESOI and Smart-Cut® methods involve a bit more physical manipulation; requiring bonding and polishing procedures. The BESOI process incorporates two separate silicon wafers, one having a pre-grown silicon dioxide and the other serving as the handle, brought into intimate contact by a bonding process. Following bonding, the silicon overlayer is formed by etching back the top silicon wafer through successive grinding and polishing steps. Due to the imprecise nature of the grinding and polishing process, the Smart-Cut® method was developed. It uses a high energy H^+ to weaken the silicon lattice along a particular plane prior to bonding the wafer to the silicon handle wafer. Following the bonding process, thermal annealing causes the implanted wafer to split along the implant-damaged silicon plane. Only a fine chemical mechanical polish (CVP) is required thereafter.

Of the three methods the BESOI process tends to give SOI wafers with the least uniform results. However, thick and damage free silicon overlayers are characteristic of BESOI wafers; where SIMOX and Smart-Cut® require expensive epitaxial growth methods to achieve the same specifications. Therefore, the tolerance and design requirements of your device dictate the suitability of the type of SOI wafer.

The rib waveguide is perhaps the most fundamental component to silicon photonics. Several methods have been reported to produce the not prohibitively deep (0.5 – 1 μm) etches required for rib waveguides. The different etches can be broken down into two classes, wet etches and dry etches. Wet etches, such as KOH and TMAH, are generally known to be anisotropic etchants, resulting in the 54.7° sloped side walls for SOI waveguide aligned in the <100> direction and have been successfully used to produce waveguides [108]. To produce truly perpendicular sidewalls, anisotropic RIE etching, using gases such as CH_3Br [17] or SF_6/O_2 [109], has been demonstrated. Vertical sidewalls produced by RIE etching allow for greater flexibility of the rib waveguide dimensions, although smoothing techniques are often required for rough sidewalls inherent to the RIE process.

As well as etching, other standard CMOS processes, such as photolithography, metallization, and ion implantation, are also utilized to produce integrated silicon photonics devices with a wide range of functionality.

3.2 Fabrication of Bragg Gratings

The previous section introduced silicon photonics and the procedures employed for fabricating devices on the scale of about a micron and greater. We now explore the more difficult task of fabricating Bragg gratings. As determined in the last chapter, Bragg gratings in SOI require periodicities on the order of 220 nm, which places them beyond the reach of conventional photolithography. As a result, numerous fabrication procedures have been developed to achieve the high spatial resolution required for Bragg gratings.

3.2.1 Lithographic Based Fabrication Techniques

Similar to the microelectronics industry, lithography based fabrication techniques dominate the manufacturing of Bragg gratings. Of these techniques, interference lithography is the pillar of integrated Bragg grating technology. The premise of interference lithography is simple and appealing, and a direct result of the fundamental phenomenon of two interacting coherent light beams. As two coherent plane waves overlap spatially, a standing wave is formed that can be recorded in a photoresist or other photosensitive material, as illustrated in Figure 3.1.

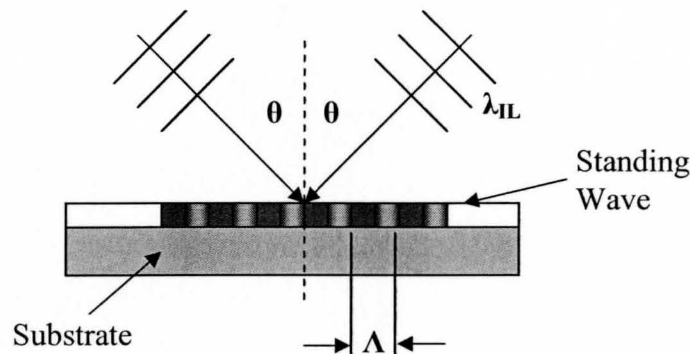

Figure 3.1 Interference holography producing a standing wave that can be recorded in a photosensitive layer.

The periodicity of the standing wave can be computed through

$$\Lambda = \frac{\lambda_{IL}}{2\sin\theta} \tag{3.1}$$

where λ_{IL} is the illuminating wavelength and θ is the half angle between the two interfering beams. To achieve a well defined periodic pattern the standing wave should possess a large degree of spatial coherence, which is related to the spatial and temporal coherence of the two interfering beams.

The Bragg gratings developed in this thesis were manufactured using a variant on the classic two beam interference system, known as a Lloyd's mirror setup. The optical setup is illustrated in Figure 3.2. In the Lloyd's mirror scheme, a mirror mounted perpendicular to the sample folds half the beam back onto itself to create the interference region. Therefore, adjusting the period of the fringes only requires a simple angular rotation of the Lloyd's mirror setup. The setup uses a 325 nm HeCd laser as the illuminating source and a pinhole is used to spatially filter any higher order lasing modes to ensure a spatially uniform optical beam intensity.

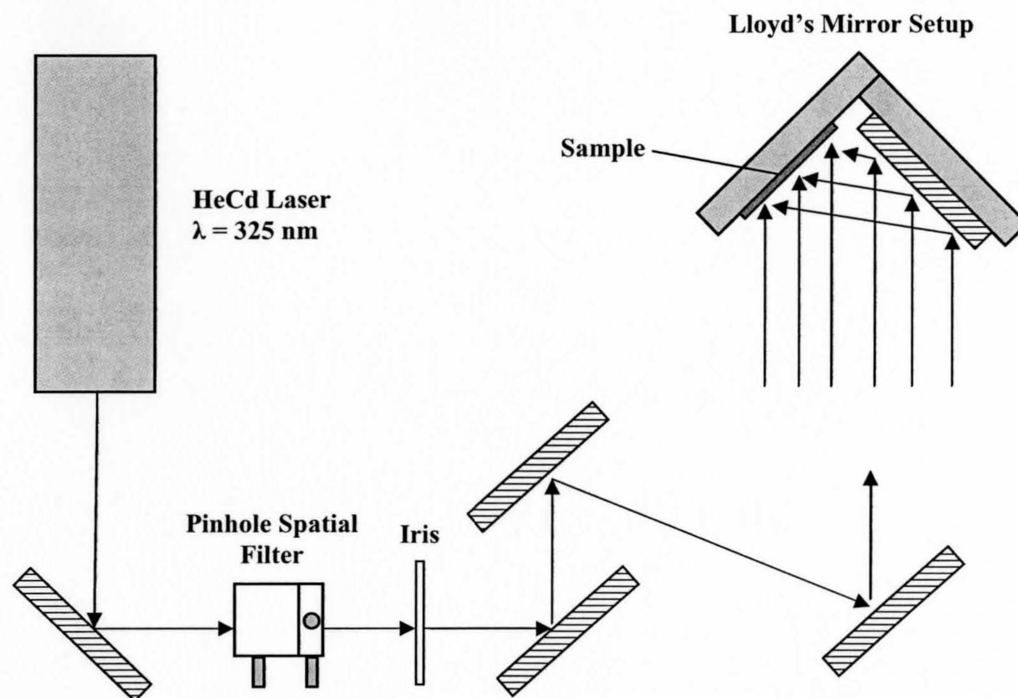

Figure 3.2 Lloyd's mirror setup employing a 325 nm HeCd laser and a spatial filter for beam uniformity.

One of the issues with this setup is the lack of collimating optics to ensure planar interacting waves at the sample. The waves are more accurately described as spherical waves. The Gaussian nature of the beam profile results in a non-uniform intensity profile of the standing wave pattern on the sample. Consequentially, exposure times and developments times are not consistent over the surface of the wafer and uneven grating profiles result. Extremely careful adjustments of the pinhole and manipulation of the beam overlap were required to produce uniform exposure intensities. Beam expansion due to an increase of the optical path length was attempted to produce a more uniform beam profile, however the reduction in beam intensity led to impractical exposure times.

Another issue with the interference lithography process is the perpendicular standing wave pattern that is produced via reflections off the wafer surface. Since the aspect ratio is generally quite large for Bragg gratings, the additional standing wave leads to ripples in the resist edges that are detrimental to line width control. Care must be taken to ensure the thickness of the photosensitive layer corresponds to only half the period of the standing wave pattern in the perpendicular direction (~150 nm). Otherwise, an additional antireflection coating is required to prevent unwanted substrate reflections.

Although the Lloyd's mirror is a very versatile setup, there are drawbacks that make it difficult to implement in a CMOS fabrication process. One of the major drawbacks is the inability to align the fringes to existing patterns on the substrate and, hence, gratings often have to be patterned first. Existing patterns on the substrate can also lead to undesirable interference effects during the exposure. There are also pattern consistency issues between consecutive samples due to the sensitivity of the grating profile with the alignment of the optics on the sample surface. Therefore, to address some of these issues, other fabrication methods have been developed.

One method is known as X-ray lithography. In this case, the initial grating pattern is produced via two-beam interference and transferred to a hard mask. The patterned grating is then used as a mask in a photolithographic procedure that uses small wavelength X-rays, capable of the required resolution, as the illuminating source [110]. The mask can be outfitted with alignment marks and ensures a repeatable grating profile from sample to sample. X-rays also have the added benefit of being absorbed by most materials, limiting the retro-reflected light off the substrate.

Another method which allows for ultimate control over the grating profiles and alignment is e-beam lithography. In this case, an e-beam is scanned over the surface in an e-beam sensitive resist, typically PMMA, to produce virtually any pattern imaginable. The biggest downfall of e-beam lithography is throughput, as the process requires each pixel to be exposed separately and sequentially. However, the ability to narrowly focus the e-beam results in patterns with unprecedented resolution. E-beam lithography is generally used to fabricate prototype devices and generating masks that can be utilized in more conventional lithographic processes.

Phase mask lithography is another alternative for producing fringe patterns [111]. In this case, an illuminating source impinges on a diffractive phase mask that, in turn, diffracts the light into three or more orders. The phase mask is generally designed to only diffract light in the +1 and -1 orders, and suppress 0th order diffraction. The +1 and -1 order then interfere to produce the standing wave pattern a short distance away. This method tends to be more stable than conventional interference lithography systems because the substrate and phase mask are typically held in vacuum contact, whereas in the conventional setup the beam is split and travels over relatively long distances before interfering on the photosensitive layer.

3.2.2 Other Fabrication Methods for Bragg Gratings

Although the most common methods were mentioned in the previous section, other, more physically based, methods also exist to produce Bragg gratings. Focused Ion Beam (FIB) milling has gained a lot of popularity recently for its ability to produce well

controlled extremely fine features. In this case energetic ions, usually Gallium or Xenon, are incident on a sample, in a similar manner to scanning electron microscopy (SEM), and cause the sputtering of a tiny amount of material. By repeating this process a pattern can be formed. The benefit of this process is that it is a direct writing process. Indeed this method has been used to produce Bragg gratings in SOI [35, 112].

Deep-UV contact lithography brings into intimate contact a pre-existing grating with a surface to be pattern. If the mask and resist are designed properly, upon UV illumination near-field optical effects allow for the transfer of patterns which would normally be below the resolution limit of the illuminating optics [113].

Although generally limited to polymer based materials, nano-imprint lithography involves the pressing of an existing surface relief grating pattern into a polymer material to produce another surface relief Bragg grating [114].

3.3 Implanted Bragg gratings in SOI waveguides

All implanted Bragg gratings described in this thesis were developed on SIMOX SOI wafers with a device layer thickness of 2.5 μm, a 0.375 μm buried oxide layer and a 625 μm base layer thickness. The wafers were lightly *p*-doped (boron) to a produce a nominal resistivity of 20 – 30 Ω cm. Following cleaving, the one inch square samples were subject to a rigorous cleaning procedure to remove the native oxide and residual organics and metals. The cleaning process consisted of a twice repeated acetone, methanol, deionised water (DI) rinse, followed by a 10 minute H_2SO_4:H_2O_2 (4:1) etch,

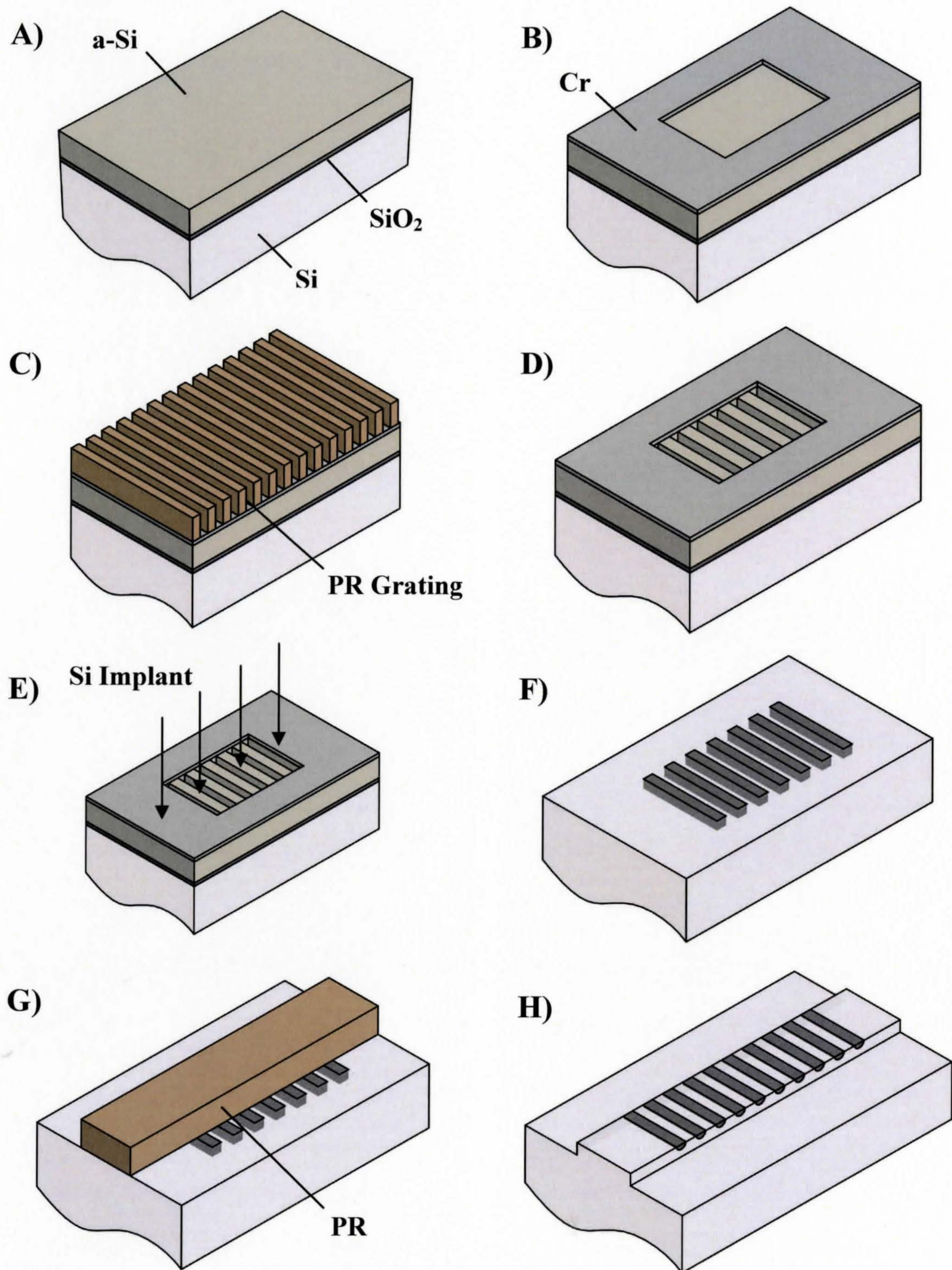

Figure 3.3 Fabrication process used to transfer implanted gratings to an SOI rib structure.

followed by a 20 minute UV ozone growth and a subsequent one and a half minute hydrofluoric acid (HF) etch.

Figure 3.3 outlines the steps implemented to fabricate the ion implanted Bragg gratings in SOI. The process has been broken down into eight steps and they will be explained hereafter.

A) Deposition of SiO_2 Buffer Layer and a-Si Implantation Mask

To provide adequate masking during the ion implantation process the deposition of two layers is required. The first layer is a ~25 nm thick silicon dioxide layer that serves as a buffer layer. The buffer layer acts as both an etch stop when transferring the grating pattern to the a-Si layer and lift-off layer when removing the a-Si layer following implantation. The second layer is an a-Si layer that serves as the implantation mask. Using the SSUPREM4 implantation simulator it was determined that the a-Si thickness should be approximately 250 nm thick to ensure adequate stoppage for Si ions implanted with energies of up to 60 keV. The thickness was chosen such that minimal ions (R_p + $3\Delta R_p$) would reach the silicon overlayer and cause damage. The SiO_2 and a-Si layers were deposited with an inductively couple plasma enhanced chemical vapour deposition (ICP-PECVD) chamber at McMaster University. An SEM of the deposited layers is shown in Figure 3.4, where the two little bumps are merely dust particles.

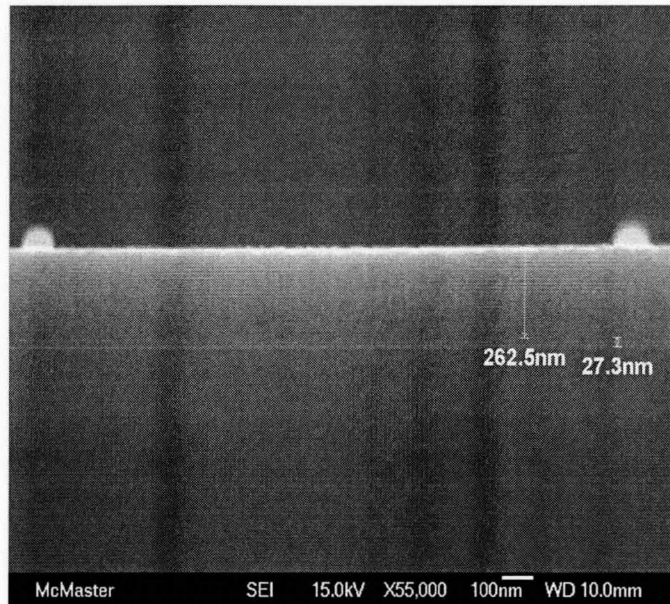

Figure 3.4 SEM showing deposited SiO_2 layer (~27 nm thick) and a-Si layer (~262 nm thick).

As can be seen, voids exist in the a-Si layer, which is common for a-Si CVD deposition. Following deposition, a high temperature anneal of 1000°C for 45 minutes was performed in a nitrogen ambient and atmospheric pressure to reduce the void concentration and rigidify the film. Annealing causes crystallization of the a-Si film, resulting in a poly-Si film. The poly-Si layer is preferred over a-Si because it has etching characteristics closer to c-Si when RIE etching, and well defined anisotropic c-Si RIE etches are well known.

B) Define Grating Windows

One of the downfalls of interference holography is the inability to define and align gratings to particular segments of the sample wafer. Therefore, prior to Bragg grating patterning with the Lloyd's mirror setup, grating windows must be defined that will

localize the gratings to specified locations. Grating windows with widths of 100 μm and lengths ranging from 350 – 2100 μm were patterned. This was accomplished with a chromium lift-off process.

Shipley 1808 positive photoresist was spun at 4000 rpm for 30 seconds to achieve a photoresist thickness of ~800 nm. Following a soft bake of 90 ^{O}C for 1 minute, undercutting was elicited by slightly overexposing (35 mJ) the photoresist using a Karl Suss MA6 mask aligner. The grating windows on the mask were aligned to the edge of the sample, which had been cleaved along a crystallographic plane; ensuring gratings are aligned perpendicular to the windows. To achieve good lift-off results, a preferential hardening of the surface was carried out via a 10 minute soak of the exposed wafer in toluene without agitation. After nitrogen blow drying, the sample was developed in a solution of DI:Microposit 351 (5:1) for ~40 seconds. A ~30 nm chromium layer was deposited using an e-beam metallization system to serve as the grating window. Following deposition, the chromium was lifted-off using an acetone bath for 10 minutes followed by a 2 minute ultrasonic acetone bath to remove any residual chromium particles.

C) Pattern Holographically Defined Grating

The gratings were defined using the Lloyd's mirror setup, as described in Figure 3.2, and were designed to exhibit resonance at a wavelength of ~1550 nm (period of 222 nm). Fabricating gratings is a highly sensitive process, both temporally and also to contamination. In order to achieve repeatability, extreme care must be exercised to

ensure clean glassware and to follow process steps in a timely manner. Due to the complicated nature of the process, the detailed steps are outlined in Table 3-1 below.

Table 3-1 Processing steps to achieve Bragg gratings in PR

STEP	PROCESS	COMMENTS
1	Bake sample	Hot plate 80°C for at least 5 minutes
2	Apply 2:3 (PR:Thinner) solution	After application wait 30 seconds
3	Spin	5000 rpm for 30 seconds
4	Wait 5 minutes	
5	Soft Bake	Hot plate at 80°C for 1 minute
6	Exposure	25 mJ of energy (~50 seconds)
7	Develop	CD-30 developper, slow agitation, approximately 45 seconds
8	Rinse	DI water 30 seconds
9	Blow dry	N_2 carefully
10	Hard Bake	Hot plate 110°C 2 minutes

During exposure the gratings are aligned on the chuck according to the same edge of the sample that was used to define the gratings windows. This will provide adequate alignment between the rib and the grating when the rib is defined in the silicon. To achieve a suitably thin PR thickness, ensuring good line width control, Shipley 1808 PR must be thinned to a ratio of 2:3 with positive PR thinner. After spinning at 5000 rpm, the result is a PR thickness that is on the order of the lateral feature size ~100 nm.

Since the PR is thinner it also requires a lower soft bake temperature and tends to be more susceptible to temperature variations. If the hot plate is too hot, not enough PR is removed during development and the grating is patchy. If it is too cold, too much of the PR is removed during development. After exposure to 25 mJ of UV light, the sample is developed in a gentle developer (Shipley CD-30). The development process is a very

difficult process to achieve good repeatability because the sensitivity of the process to small changes in cleanliness and surface deviations is quite large. Close inspection and slow agitation appeared to give the best results. When the sample is submerged, it first goes to a deep blue colour and remains this way for a large portion of the development process (20 – 30 seconds). The sample will then suddenly begin to turn a beige colour. The key is to carefully watch the sample until the whole area has uniform beige colour, and then rapidly remove the sample and immerse it in DI water. To achieve the best gratings, the exposure time should be adjusted such that the total development time is ~45 seconds.

To test the integrity of the grating, diffraction from a white light source can be used. Under the proper angle the diffracted light should be a uniform bright blue colour. The presence of black regions signifies either underdeveloped or overdeveloped grating regions. An example of gratings patterned in PR is shown in Figure 3.5. Notice the PR gratings are continuous across the chromium grating windows. Therefore, the height of the grating windows (~30 nm) had little effect on the spinning and development of the grating pattern.

D) Etching Gratings into a-Si Hard Mask

To produce a hard mask suitable for ion implantation the PR grating must be etched into the a-Si layer. This was accomplished using the Bosch process on an Alcatel 601E RIE etcher at the University of Western Ontario (UWO). The Bosch process is a cyclical etching procedure that alternates between etching and passivating cycles and allows for highly anisotropic (~ 90°) deep etches. The etching sequence uses a sulphur

hexafluoride (SF_6) ion enhanced plasma etch in a 2 second interval to etch the silicon in a nearly vertical direction. The next 1 second interval deposits a Teflon-like chemically inert passivating layer using C_4F_8 gas. The layer is deposited over the entire substrate, including the sidewalls. During the next etching stage, the directional ions in the plasma bombard the passivating layer along horizontal surfaces only. Was the sputtered off passivating layer is gone the etching sequence continues. By alternating these cycles, highly vertical etches with aspect ratios of 20:1 or more can be achieved. All the etches at Western were performed under a pressure of 1×10^{-2} mBar, plasma source RF power of 1000 W, substrate bias RF power of 80 W, and the backside of the sample was He cooled to 20 °C.

The etching rate of the photoresist, a-Si, silicon dioxide, and chromium were found to be ~100 nm/min, ~275 nm/min, ~25 nm/min, and < 5 nm/min respectively. This gave a selectivity of 2.75:1 of a-Si to PR. Therefore, the ~100 nm thick PR grating is just enough to etch the a-Si hard mask. The etching process was carried out for 1 minute and any over etching of the a-Si would essentially stop on the silicon dioxide buffer layer underneath. The large selectivity between chromium and a-Si ensured gratings were only etched at the grating windows. SEM images of the etched a-Si gratings are shown in Figure 3.5. The sinusoidal shape of the a-Si gratings are a consequence of the sinusoidal shape of the PR gratings. Since the edges of the grating teeth are thinner than in the middle, the process will etch through to the underlying a-Si in these areas and transfer the sinusoidal shape to the underlying layer. Following RIE etching, the residual PR was removed via an O_2 plasma ash for 10 minutes. Under white light, the gratings exhibited

uniform bright blue diffraction, signifying a very good transfer of the grating pattern to the a-Si.

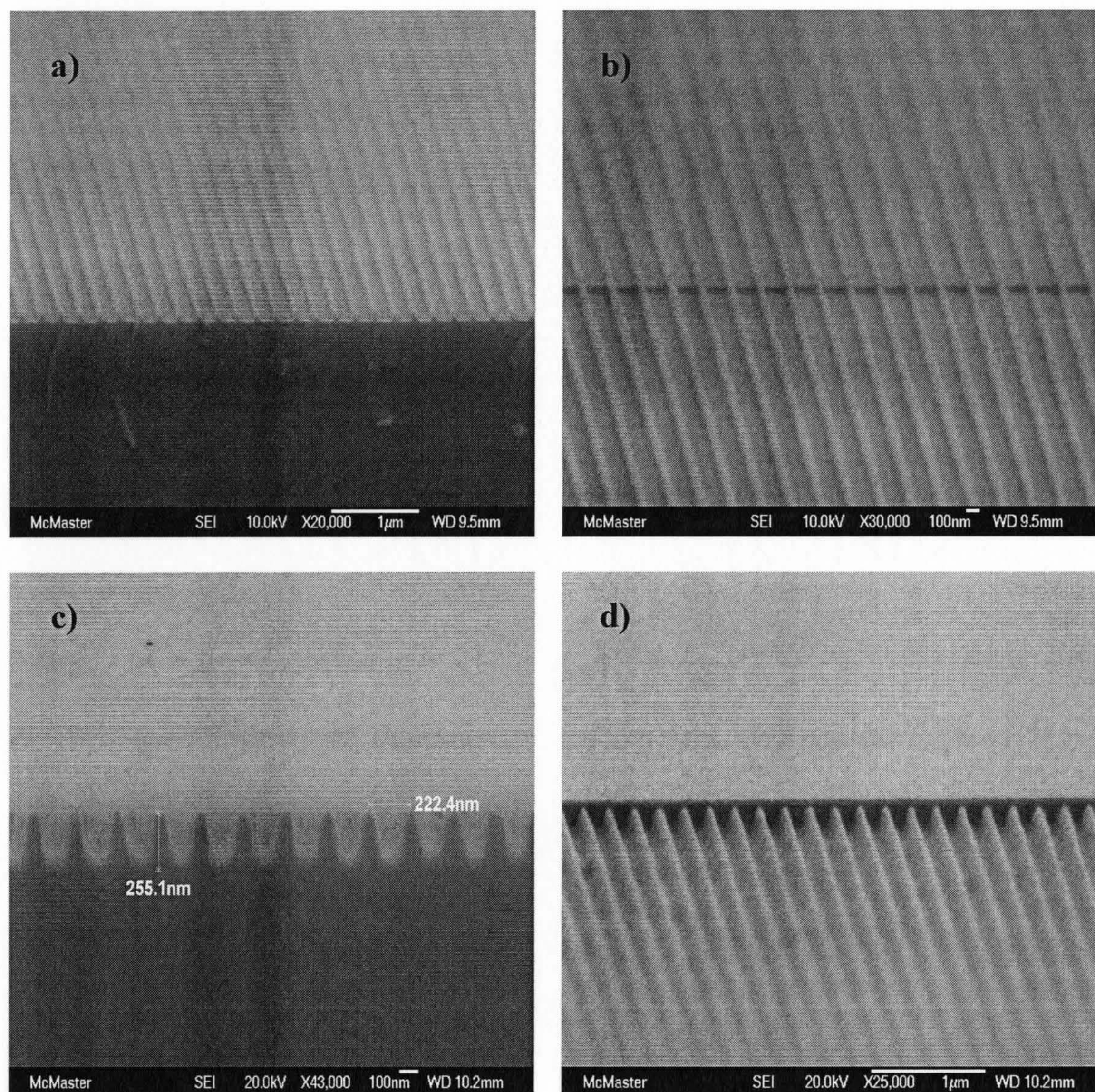

Figure 3.5 Illustration of fabricated Bragg gratings. a) PR gratings on silicon after development, b) PR gratings showing the effect of the chromium grating window, c) gratings etched into a-Si, d) grating etched into a-Si showing effect of chromium grating window.

E) Implantation of Si Ions

To produce damage-induced amorphous Si, Si ions were implanted using the ion implanter at UWO. To ensure complete amorphization the samples were implanted at liquid nitrogen temperatures (77 K) to a nominal dose of 2×10^{15} ions/cm^{-2}. From the SSUPREM4 simulations carried out in Chapter 2, energies of 50 keV and 60 keV were used during the implantation process. The presence of the silicon dioxide buffer layer minimizes channelling due to its non-crystalline structure, thus a tilt angle of 0° was used. Care must be taken to ensure intimate thermal contact between the sample and the sample holder during implantation to prevent possible dynamic annealing. A thermal paste placed between the sample and holder provides better thermal contact.

F) Implantation Mask Removal

Following implantation, removal of the implantation mask was carried out in order to pattern and etch the rib in the following step. First, the chromium grating window was removed via a selective chromium etch in Cyantek's CR-100 etchant. The etching rate was determined to be ~35 Å/min.

To remove the a-Si layer, the sample was submersed in HF for ~17 minutes. Two effects were found to occur. The PECVD a-Si has some oxygen content in the film and etches in HF at a rate found to be ~20 Å/min. Ultimately, however, the voids present in the film, and the grating teeth openings, led to the HF seeping to the silicon buffer layer below. After ~17 minutes the a-Si layer appeared to 'lift-off' quickly from the c-Si substrate layer. It is thought that the HF etch slowly opened the voids in the a-Si until an

appreciable amount of HF could interact with, and etch away, the oxide layer below. After the removal of the implantation mask, a visible colour difference existed in regions of the SOI wafer that had been ion-implanted. This is indicative of silicon amorphization and suggests that the areas were, in fact, damaged by the ion implantation process.

G) Rib Patterning

To integrate the Bragg grating into a rib structure, the planar implanted SOI samples were patterned using standard photolithography techniques. Ribs were defined in a ~800 nm thick Shipley 1808 photoresist using the Karl Suss MA6 mask aligner. The PR ribs are used directly as the etching mask in the RIE etching of the rib waveguide in the following step.

H) Etching the Rib and Facet Preparation

Using the Alcatel 601E RIE etcher at UWO again, the PR ribs were etched into the SOI wafer. The etching rate of the silicon was determined to be ~1.1 μm/min, making the selectivity of PR to silicon roughly 1:10. Since the etch depth of the silicon was targeted to be approximately 700 nm, see Figure 3.6, the PR mask is more than adequately thick. According to the theory and simulations presented in Chapter 2, the rib dimensions that ensure single mode operation and provide ample grating strength are illustrated in Figure 3.6. For comparative purposes, the actual etched rib waveguides are also presented. The geometric deviations from the simulated model should have little effect on the performance of the gratings, as only slight changes in the modal profile will occur; resulting in small modifications of the coupling coefficient only. Notice the

'scalloping' of the sidewalls of the rib structure. This is caused by the two cycle etching required for the Bosch process.

To ensure no surface corrugation exists along the rib structure near the implanted region, SEM images were taken along the entire length of various waveguides. To a resolution of ~10 nm no signs of surface corrugation existed along any of the waveguides

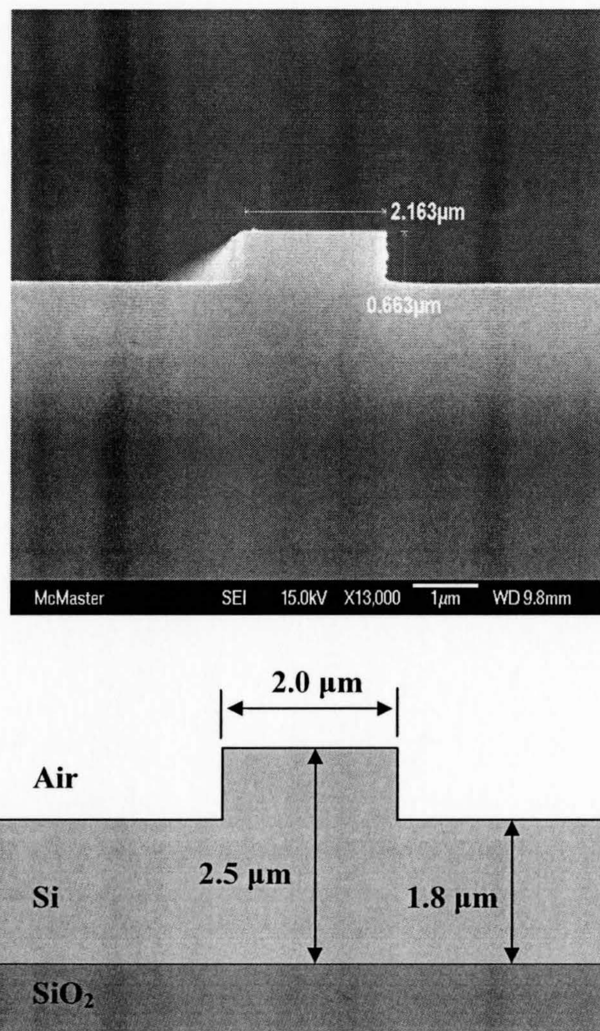

Figure 3.6 SEM images showing the dimensions of the actual etched rib and the simulated rib.

and the rib waveguides appear to be well defined along their lengths. An image of the rib in the location of the implantation is shown in Figure 3.7.

Optical facets were prepared through thinning and cleaving process, where the finished facet can be seen in Figure 3.6. To produce optimal facets the samples must be thinned down to a thickness of 250-300 μm. The samples were backside-thinned with a wet silicon carbide sandpaper. Samples were mounted on a sanding block facedown using a small amount of crystal bond. After thinning, the mounting blocks were heated to remove the sample. Any residual crystal bond was removed in an acetone bath followed by a 10 minute O_2 plasma ash.

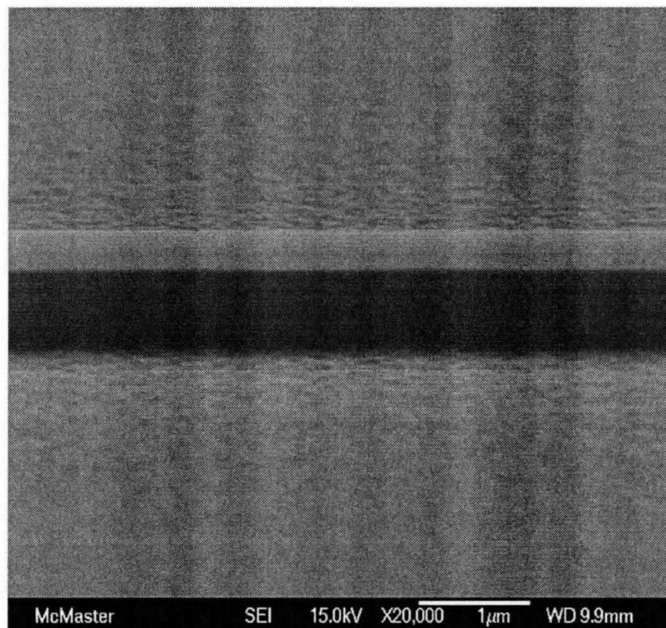

Figure 3.7 SEM image of the completed ion implanted SOI rib structure.

Chapter 4

Experimental Results

4.1 Experimental Setup for Optical Characterization

Two implanted rib samples in SOI, one implanted with a Si ion energy of 50 keV and another with 60 keV, were prepared with 10 grating lengths ranging from 350 – 2100 μm. Using Monte Carlo simulations, the estimated grating depth was ~140 – 150 nm and the duty cycle was approximately 20/80 for crystalline to amorphous regions. The rib

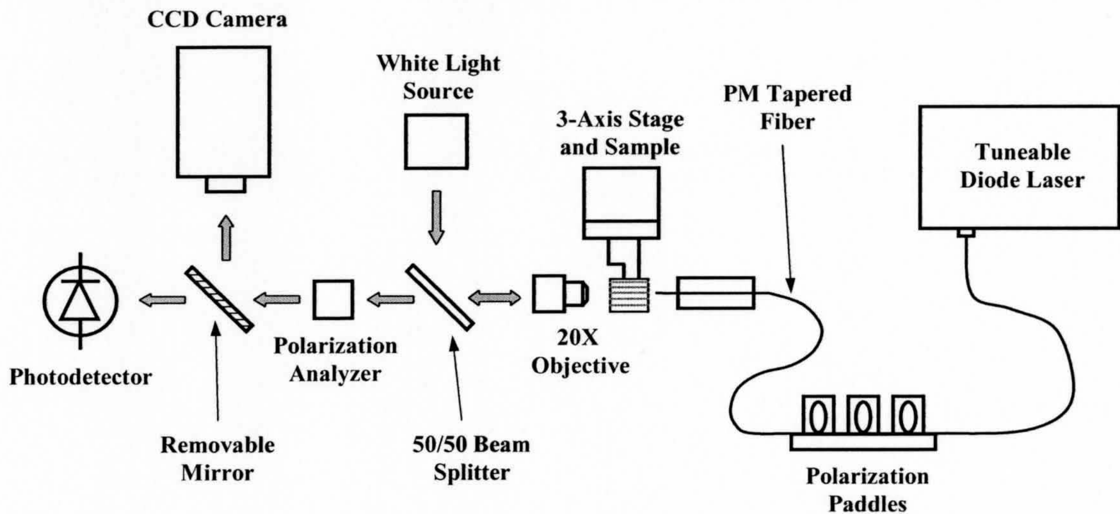

Figure 4.1 Experimental setup for optical characterization.

width was 2.2 μm and the silicon ridge layer was 2.5 μm at its center. The ribs were etched to a depth of ~700 nm. Five implant-free straight waveguides were also etched in each sample to measure the excess loss caused by the insertion of the implanted Bragg gratings.

To measure the response of the Bragg grating in the SOI rib waveguide for TE and TM light, transmission spectra were obtained using the experimental setup shown in Figure 4.1.

First, a tuneable diode laser scanned in the wavelength range 1520 – 1570 nm was fiber coupled to a three-pronged polarizer. The stress-induced birefringence acting on the looped fiber can be altered by tilting the paddle. Polarization changes can be made by altering the tilt of any of the paddles. The state of polarization, TE or TM, was set by the polarization analyzer in the setup. The polarized light was then fed through a polarization-maintaining (PM) single mode tapered fiber. This helps maintain the

polarization state set by the polarization paddles and slowly reduces the size of the optical mode in the fiber to ~2.5 μm to achieve better modal-matching with the mode of the rib waveguide, improving coupling drastically. Using a set of stages, the fiber was butt-coupled to the rib waveguide facet.

The light output from the rib waveguide was collected via a 20X objective lens. The light was then directed to either the CCD infrared camera, to aid in optical alignment and image the mode, or to the InGaAs photodetector to measure the optical power transmitted. The white light source and the 50/50 beam splitter were used for alignment purposes only.

4.2 Transmission Spectra and Strength of Implanted Gratings

TE and TM transmission spectra for the 50 keV and 60 keV implanted samples were measured by scanning the tuneable diode laser from 1520 nm to 1570 nm with a wavelength step of 0.1 nm. The results for grating lengths ranging from 350 μm to 2100 μm were obtained. TE spectra for the 60 keV sample with grating lengths of 350 μm, 1280 μm, and 2100 μm are shown in Figure 4.2. Each transmission spectrum was normalized to its corresponding throughput power at an off-resonant wavelength in order to establish grating strength trends. The losses invoked by the increased grating lengths will be discussed in the following sections.

There are two distinct dips in the transmission spectrum. The dip at ~1555 nm corresponds to the anticipated coupling between the forward and backward travelling

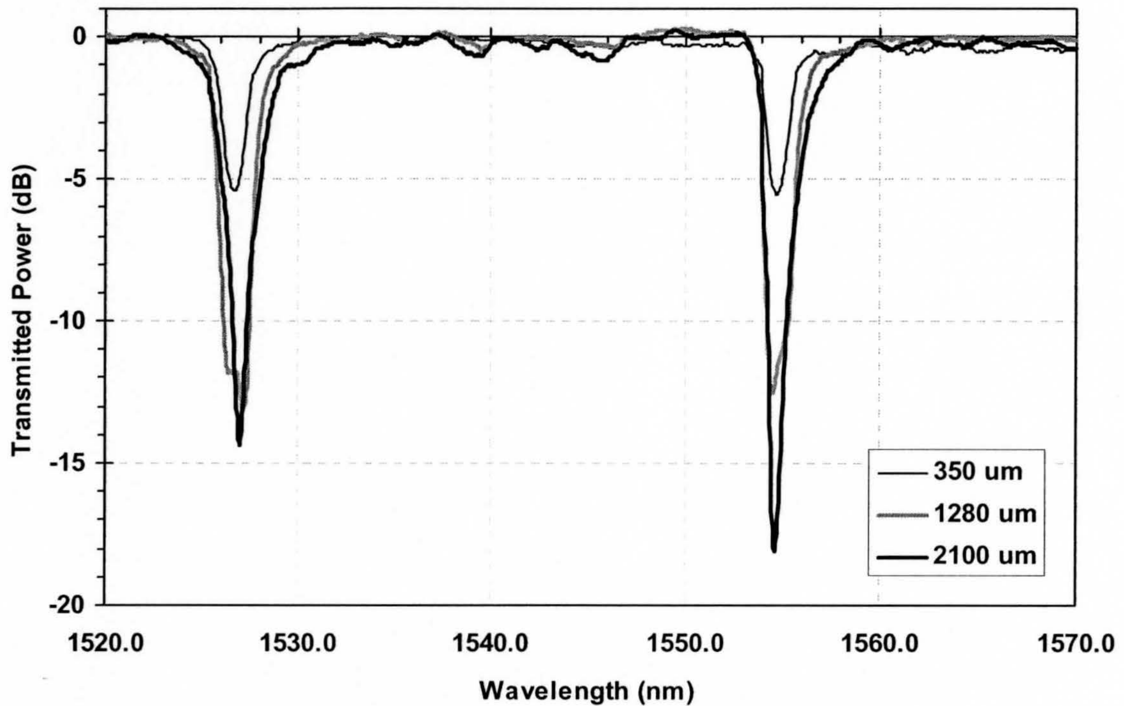

Figure 4.2 Measured TE transmission spectra for 350 μm, 1280 μm and 2100 μm long gratings and 60 keV implantation. The fundamental dip occurs at ~1555 nm, while the other dip (at ~1525 nm) corresponds to the 1st leaky mode.

fundamental modes. The dip occurring at ~1525 nm is a result of the fundamental forward travelling mode coupling to the 1st order backward travelling radiation mode.

The presence of radiation coupling is a well studied phenomenon in fiber Bragg gratings [115]. In the case of single mode rib waveguides, the second dip can be explained by grating-assisted coupling to higher order backward travelling modes. Although present in the transmission spectrum, the higher-order backward travelling modes are not supported in the single mode rib waveguide, and will radiate out of the rib shortly after being excited. Consequently, reflection spectra only exhibit peaks at the fundamental resonant wavelength.

As is expected, the suppression of the resonant wavelength is an increasing function of the grating length. The transmitted power for the 2100 μm long, 60 keV implanted grating exhibited an extinction of -18.10 dB. The 50 keV implanted Bragg grating showed similar behaviour, however for a 2100 μm grating length an extinction of -11.54 dB at the Bragg wavelength was achieved. This is in agreement with theoretical considerations because the higher implant energy results in a deeper damage profile, increasing the overlap integral of the grating with the mode and, therefore, increasing the strength of the grating per unit length. For 2100 μm grating length, the -3 dB bandwidth was measured to be ~0.65 nm (81 GHz) for the 50 keV implant and ~0.45 nm (56 GHz) for the 60 keV sample. It is noted that for both the 50 keV and 60 keV samples the Bragg wavelength occurs at ~1554.6 nm, showing the consistency of the fabrication process between samples. The slight deviation from the anticipated resonant wavelength of 1550 nm can be attributed to a slight angular misalignment of the Llyod's mirror setup. An angular deviation of 1° leads to a change in the Bragg wavelength of ~25 nm, making proper alignment crucial.

Figure 4.3 shows the measured TE and TM transmitted spectra for a 2100 μm length 60 keV implanted sample. The separation between the fundamental peaks is ~1.20 nm, or equivalently 150 GHz. Theoretically, for a 150 nm implant depth, the modal birefringence is predicted to be ~0.96 nm, or 120 GHz. The discrepancy is likely due to damage-induced increases of the refractive index in between grating teeth and also beyond the amorphous/crystalline transition region, which are not considered in the simulations. Also, the TE polarized mode shows a much stronger Bragg reflection than

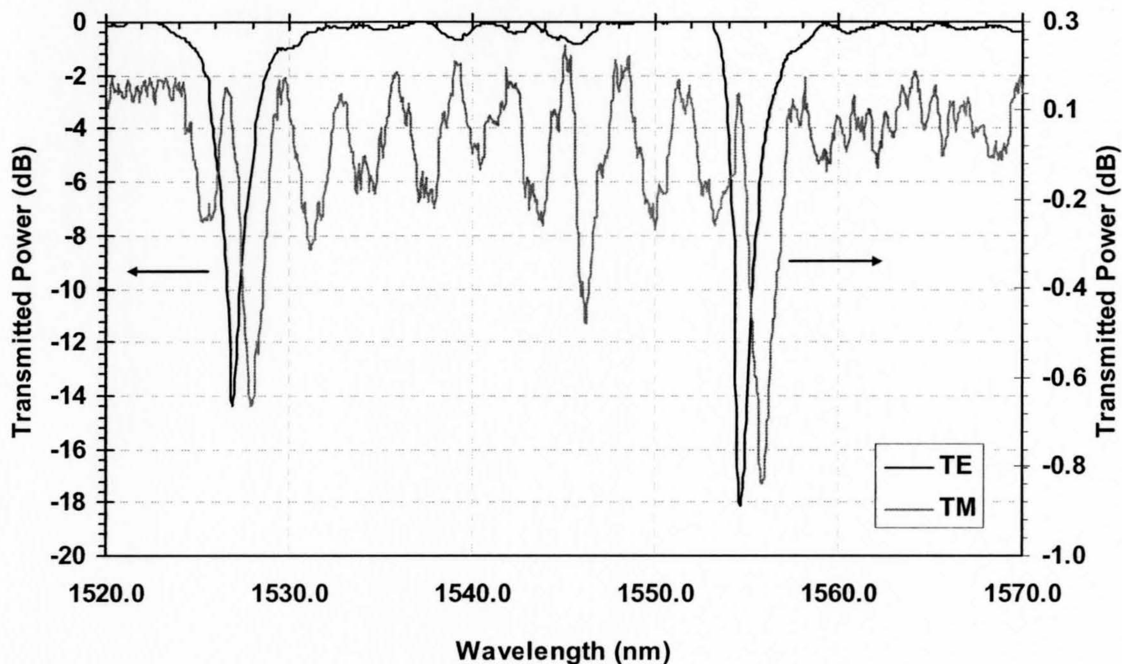

Figure 4.3 Measured transmission spectra of TE and TM polarization for 2100 μm length, 60 keV implanted grating sample.

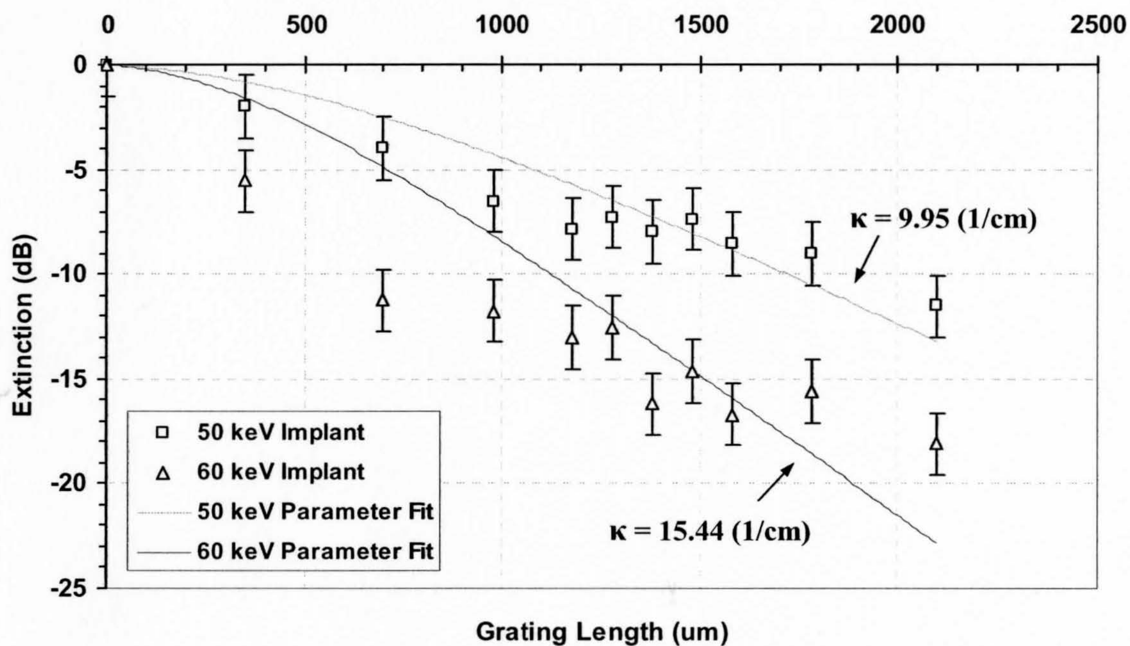

Figure 4.4 Grating strength as a function of the grating length for 50 keV and 60 keV implants.

the TM mode. Although this is expected, as described in Section 2.3.3, the magnitude of the difference is larger than anticipated. It is thought that a substantial difference in the mode overlap, as a result of mode shifting, occurs for TE polarized modes. Although detrimental for optical filtering applications, this effect could have interesting implications for polarization splitting.

Figure 4.4 depicts the relationship of the grating strength as a function of the grating length. Based on 5 successive measurements of 5 different waveguides, the uncertainty was estimated to be 1.5 dB. From the data it is possible to extract the coupling coefficient that characterises each of the Bragg grating samples. Using the coupled mode equations (2.75), a parameter fitting algorithm based on a standard least squares analysis was implemented to determine the coupling coefficient that demonstrated the best fit to the measure data, see Figure 4.4. The coupling coefficients were computed to be 9.95 cm^{-1} and 15.44 cm^{-1} for the 50 keV and 60 keV implanted samples respectively. According to the coupling coefficient calculations in section 2.3.3, and assuming a 20/80 duty cycle of crystalline to amorphous regions, the depth of the implant to achieve these coupling strengths would be approximately 161.8 nm for the 50 keV sample and 177.7 nm for the 60 keV sample. Compared to the Monte Carlo damage profiles computed in section 2.2.3, the simulations are close, but predict amorphous depths ~10 – 15 nm shallower. Similar to before, this can be attributed to the increased index below the amorphous/crystalline transition interface and the increased index between grating teeth, which are very difficult to estimate. Accounting for the increases

in the coupling coefficient calculations would result in a greater degree of modal shifting and, consequently, larger coupling coefficients per implant depth.

For comparison, Figure 4.5 plots the measured TE spectrum of a 2100 μm, 50 keV implanted sample, against the calculated spectral response, assuming $\kappa = 9.95$ cm^{-1}. Both plots were normalized according to their respective transmitted power at an off-resonant wavelength. There is good agreement between the two spectra, verifying the validity of the CMT model employed. Similar agreement was found between the measured and calculated spectra for the 60 keV implanted sample.

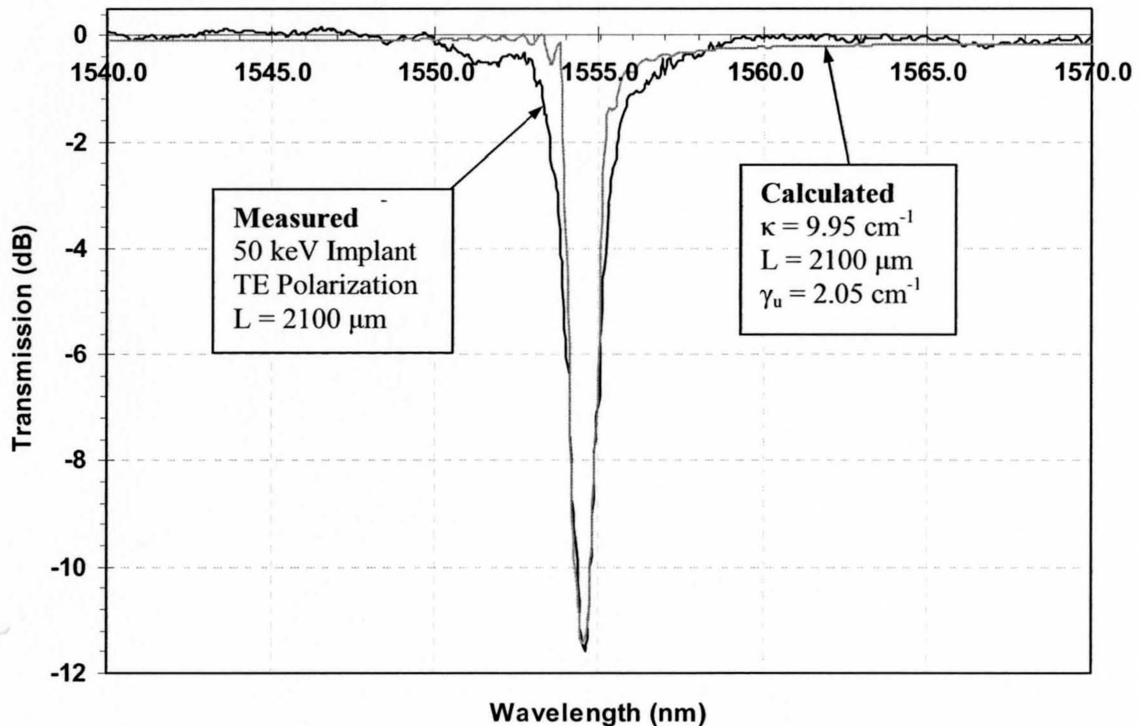

Figure 4.5 Comparison of measured and calculated TE spectral response for 50 keV implanted sample. The grating length L was 2100 μm.

4.3 Loss measurements

There exist many loss mechanisms that are detrimental to optical propagation in rib waveguide structures. The most prominent loss mechanisms include, scattering from sidewall roughness, mode-mismatch induced coupling losses, and Fresnel reflections at the input and output facets. Many of these losses are contingent on the fabrication process, or can be systematically minimized by another means and, therefore, it is usually beneficial to simply analyse the additional loss incurred by the incorporation of the device into the rib structure. This can be accomplished by including a series of straight waveguides on the sample with similar dimensions. Using the straight waveguide as a reference waveguide, the excess loss due to the implanted grating can be determined.

Figure 4.6 shows the measured excess loss as a function of the grating length for the 50 keV and 60 keV samples for both TE and TM polarizations. For the 50 keV implanted sample, the excess losses per unit length were measured to be 0.9 dB/mm (2.05 cm^{-1}) and 0.6 dB/mm (1.38 cm^{-1}) for TE and TM polarizations respectively. The 60 keV implanted sample had excess losses per unit length of 1.2 dB/mm (2.75 cm^{-1}) and 0.6 dB/mm (1.38 cm^{-1}) for the TE and TM polarizations respectively. Using the modal confinement factors computed with BPM in Section 2.3.3 and the appropriate duty cycle, the bulk propagation loss due to the implant of the as-implanted samples can be approximated. The bulk propagation losses due to the implant were found to be 0.2279 dB/μm (655 cm^{-1}) and 0.1979 dB/μm (568 cm^{-1}) for the 50 keV and 60 keV samples respectively.

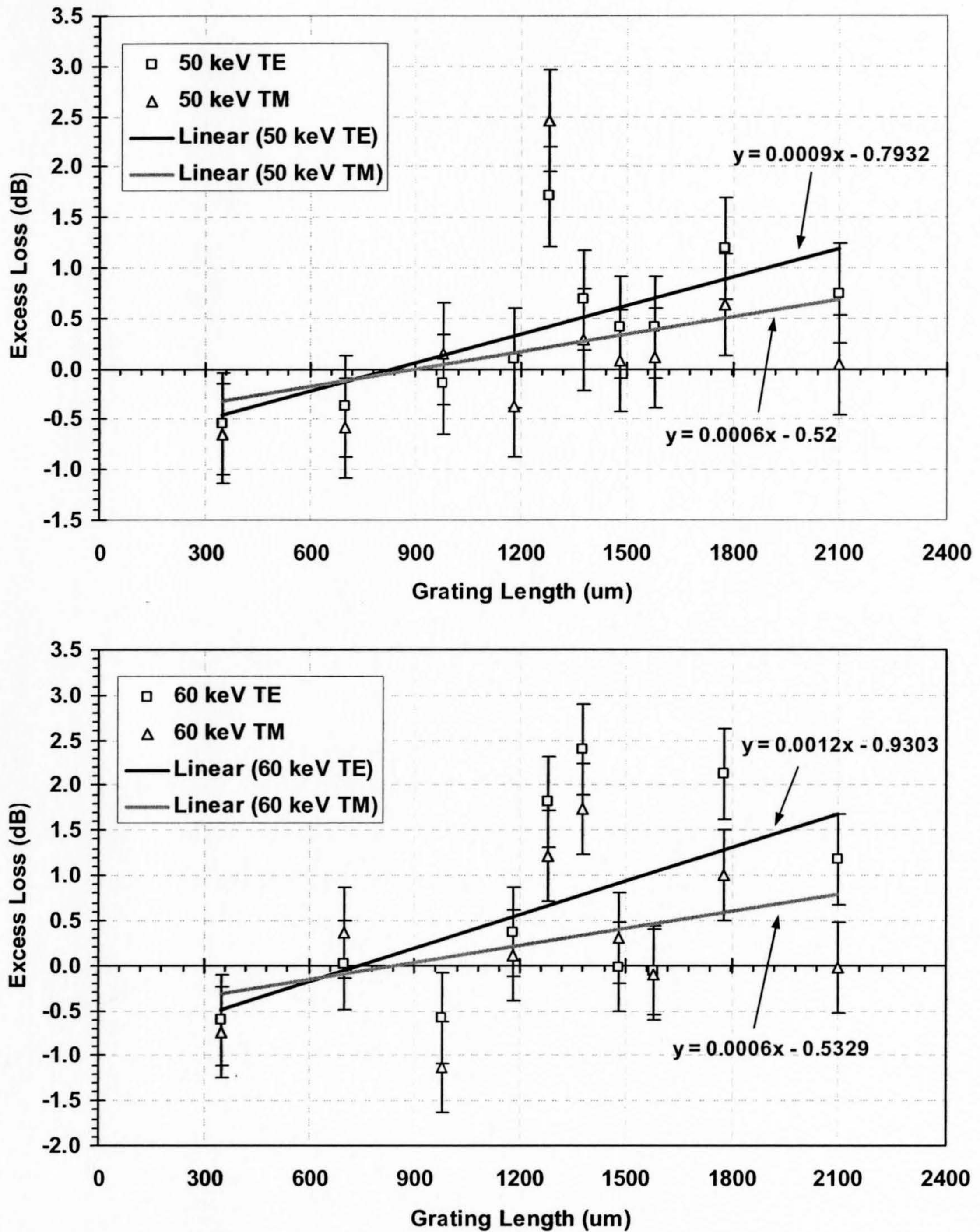

Figure 4.6 Excess loss measurements for TE and TM polarizations for the 50 keV and 60 keV implanted samples.

4.4 Low Temperature Annealing Effects

To mitigate the extent of the absorption effects, low temperature annealing can be applied to annihilate some of the low energy defects, such as interstitials, divacancies and di-interstitials, responsible for subgap optical absorption. On the other hand, complex defect clusters, dislocation loops, {113} defects and other high energy defects associated with amorphous silicon require high temperature annealing (~800-1000 °C) for removal. Therefore, low temperature annealing will reduce losses and 'sharpen' the grating profiles by annealing out defects in between the grating teeth and below the amorphous/crystalline interface.

To measure the change in the optical properties, isochronal annealing was carried out on the 60 keV implanted sample for 10 minute intervals at temperatures of 200, 250 and 300 °C. After each 10 minute anneal, excess loss measurements and spectral responses were obtained in a similar manner to that described previously. Figure 4.7 illustrates the excess loss as a function of annealing temperature for the 2100 μm grating length. Also plotted is the modal absorption loss due to the implanted damage, which was computed from linear fit curves of the excess loss versus grating length for the selected temperatures. Following implantation, temperatures of up to 150 °C were required during device processing and, hence, only annealing results obtained thereafter were relevant.

After annealing we observe a dramatic reduction (~2.7 times) of the excess loss and modal absorption coefficient between the unannealed and 300 °C annealed values. At an

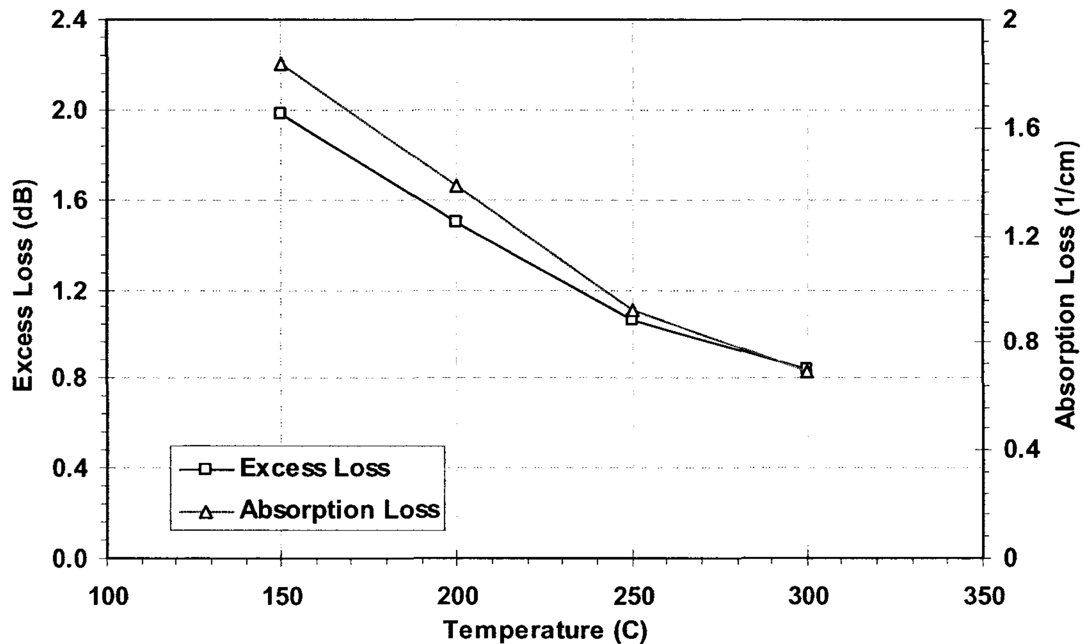

Figure 4.7 Excess loss and the absorption loss due to the implant as a function of annealing temperature.

off resonant wavelength, this corresponds to a transmitted power of ~87 % of the input power, a drastic increase from the ~62 % transmitted pre-anneal. The measure value is close to the simulated loss of ~93% using BPM and the absorption coefficient purported by de Dood et al in section 2.3.5. Similar trends were reported by Stein *et al.* and Foster *et al.* and were ascribed to the annealing of divacancies [92, 116].

However, in their cases, the low-loss characteristics of crystalline silicon were regained after low temperature annealing due to the non-amorphizing implantation doses used. In the present case significant losses, attributable to extended defects, still exist. This suggests that the implantation dose induced amorphization.

Damage annealing also has the effect of reducing the refractive index. In highly damaged, non-amorphous regions annealing can reduce the refractive index to its

crystalline value. However, low temperature annealing of amorphous silicon can lead to a thermally stablized amorphous state, with a refractive index intermediate between as-implanted and crystalline silicon. Therefore, this can also cause a change in the spectral response of the Bragg grating. Figure 4.8 compares the unannealed spectrum to the transmitted spectra for annealing temperatures of 200, 250 and 300 °C.

The 200 °C spectrum appears to be an anomalous result, thought to be caused by an improper alignment of the optical characterization setup. There are a number of interesting patterns evoked from the annealing response of the transmitted spectra. First of all, with increasing annealing temperature there appears to be a reduction in the grating strength. Again, this is most likely due to the decreased refractive index of the tails of the

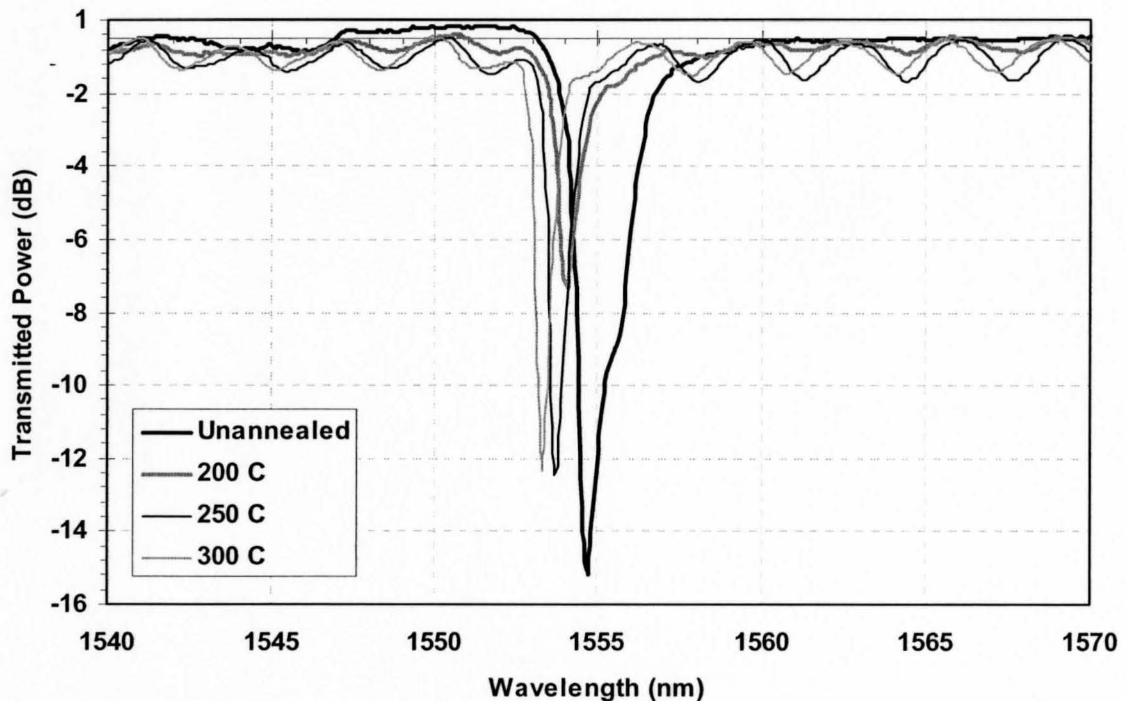

Figure 4.8 Annealing response of transmitted grating spectra for temperatures of 200, 250, and 300 °C and a grating length of 1480 μm.

implant profile, lowering the modal overlap with the grating region. There is an abrupt change from the unannealed spectrum to the 250 °C spectrum, and then a levelling off of the grating strength for the 300 °C spectrum. This implies that the refractive index change is correlated with the low energy defects as was pointed out by Wesch *et al.* [77]. There is also a noticeable blue-shifting of the Bragg wavelength with increasing temperature. This is consistent with a reduction in the refractive index between grating teeth and beyond the amorphous/crystalline interface, since the Bragg wavelength is determined by $\lambda = 2N_{eff}\Lambda$. As the effective index of the waveguide decreases, the resonant wavelength will shift to smaller wavelengths.

Another interesting phenomenon is a reduction of the -3 dB bandwidth. The unannealed spectrum has a -3 dB bandwidth of ~0.45 nm, while the 300 °C annealed spectrum has a -3 dB bandwidth of ~0.32 nm. This was consistent among measurements taken from waveguides with numerous grating lengths. The bandwidth of the filter can be mathematically described by

$$\Delta f = \frac{\kappa c}{\pi n_{eff}} \tag{4.1}$$

where n_{eff} is the effective index of the mode [41]. After annealing the effective index of the mode will decrease, thus increasing the bandwidth. However, the coupling coefficient will decrease and cause a decrease of the bandwidth. Since, the coupling coefficient is very sensitive to changes in modal overlap; this will tend to be the dominating factor. Therefore, an annealing-induced reduction of the modal overlap with the grating region, leads to a reduction of the -3 dB bandwidth.

4.5 Comparison to Etched Gratings

For comparative purposes, SOI rib waveguides integrated with an etched Bragg grating were fabricated with similar dimensions to their implanted counterparts. Figure 4.9 shows SEM images of the etched samples. The gratings were etched to a depth of ~120 nm, the grating length was ~7000 μm and the duty cycle was approximately 50/50. The rib was etched to a depth of ~750 nm.

The transmission spectra of TE and TM polarized light is plotted in Figure 4.10. Similar to the implanted samples, two distinct dips are present. For TE polarization, the dip at ~1533 nm corresponds to coupling from the fundamental forward to backward travelling mode and has an extinction of approximately -7 dB. The other dip is a result of coupling to the first higher order backward travelling radiation mode. The TM grating strength is much weaker compared to the TE response, exhibiting a suppression of approximately -1.2 dB. Similar to the implanted case, modal birefringence is present and its value is approximately 1 nm (125 GHz). The -3 dB bandwidth of the TE polarization was determined to be approximately 0.35 nm. It is noted that the shifting of the fundamental Bragg wavelength is primarily a result of a slight difference of the grating periods between the two samples.

Relative to the implanted sample, the etched grating displays a much weaker grating strength. Even though a large part of this discrepancy is a result of the shallower grating depth relative to the implanted sample, calculations of the coupling coefficient

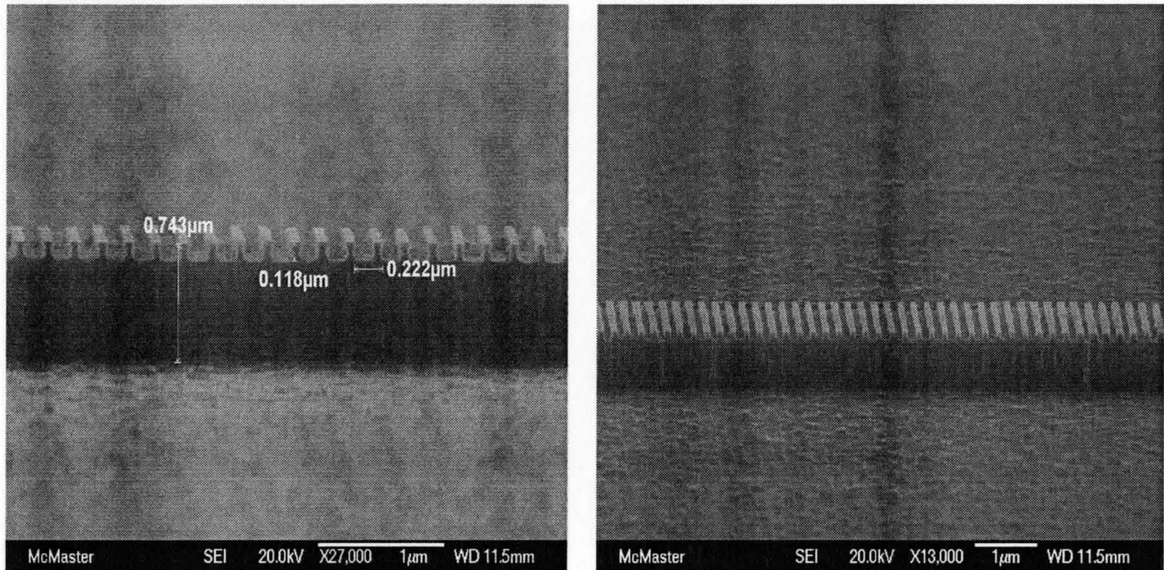

Figure 4.9 Etched grating in SOI rib waveguide. Gratings were etched to a depth of approximately 120 nm and the rib was etched approximately 740 nm. Grating length was ~7000 µm.

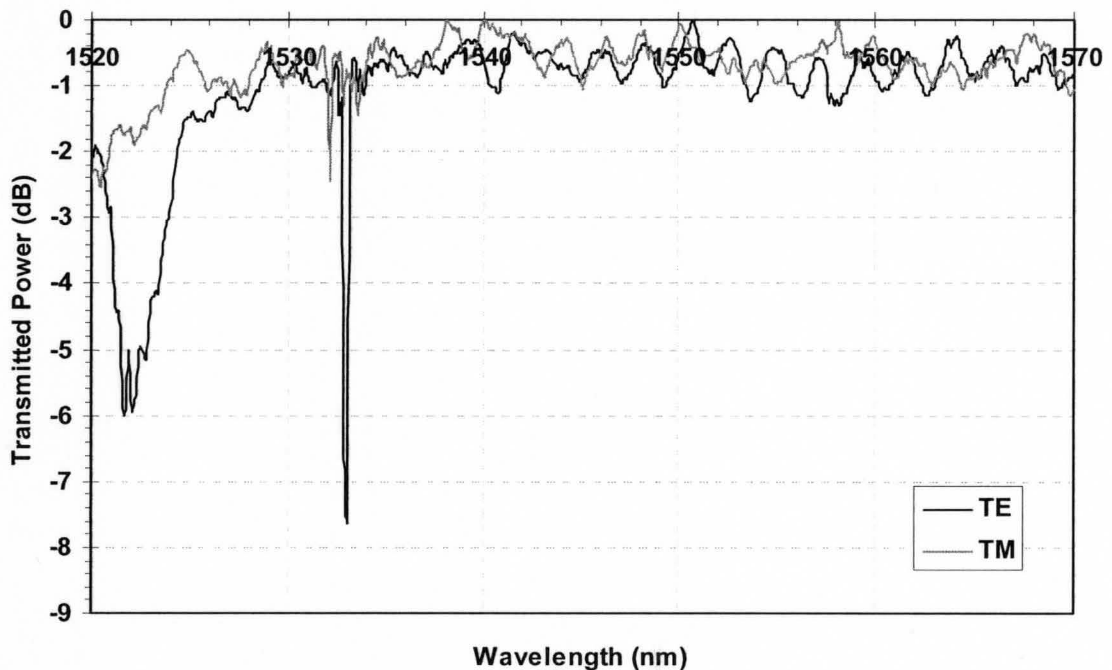

Figure 4.10 TE and TM transmission spectra of an SOI rib waveguide with etched Bragg grating. Grating depth is ~120 nm and the grating length is ~700 nm.

determined that even for an etched grating with a depth of ~150 nm, the coupling coefficient would have a value of approximately 5.2 cm^{-1}. Assuming an implanted duty cycle of 50/50, the coupling coefficient for a similar implanted sample was computed to be 6.3 cm^{-1}. Therefore, the mode shifting inherent to the higher-index implanted gratings has a dramatic effect on increasing the coupling coefficient. This effect can result in shorter device lengths for implanted gratings compared to etched gratings, which is beneficial for high density integration. Also, from the coupling coefficient calculations in section 2.3.3, the mode-shifting phenomenon is exponentially enhanced as the implant depth increases. As a result, strong Bragg gratings can be produced with only a small increase in the implantation depth.

Since the bandwidth is directly proportional to the coupling coefficient, this effect is also reflected in the larger -3 dB bandwidth of the implanted grating compared to the etched grating. Therefore, care must be taken to select an appropriate implantation depth depending on the application of interest. For optical filtering, in which a small bandwidth is beneficial, a shallow implantation should be used.

To our knowledge, this is the first demonstration of a Bragg grating integrated in SOI by means of ion-induced damage accumulation. Although losses are introduced during implantation, the devices show a strong grating response for grating lengths that are shorter than etched gratings with similar dimensions. Coupled with planar surface retention, implanted gratings could have applications for high density silicon photonic filtering, coupling and routing applications.

Chapter 5

Conclusion

To our knowledge the reported work represents the first time Bragg gratings have been successfully integrated in SOI rib waveguides by utilizing the unique optical properties associated with ion implanted defect engineering. By implanting silicon ions, and not introducing dopant species, first order Bragg gratings were fabricated by periodically amorphizing regions of the silicon device layer. The devices exhibited a characteristic Bragg wavelength dip in transmission and, importantly, retained a planar surface, making implanted Bragg gratings ideal for future processing and surface sensitive wafer bonding techniques.

Although, the extinction ratio of the implanted Bragg gratings did not adhere to the -30 dB benchmark required for optical network applications, they boded favourably compared to their etched grating counterparts. The damage induced mode shifting inherent to implanted gratings enabled the gratings to exhibit extinction ratios approximately 2.5 times larger for grating lengths approximately 3 times shorter than etched gratings with similar dimensions. This is of great consequence to silicon photonics, as integrated optical devices are typically restricted by geometric dimensions. Implanted Bragg gratings could greatly increase the device packing density while achieving the same degree of functionality as etched gratings.

Detrimental to implanted Bragg gratings is the loss introduced via defect production. The excess loss per unit length, as a direct result of the as-implanted gratings, was found to be on the order of 1 dB/mm. However, low temperature annealing of 300 °C was found to reduce the excess loss by a factor of approximately 3, to values approximately 0.3 dB/mm, while reducing the extinction ratio by only about 20%. Therefore, grating lengths of approximately 3300 μm could be incorporated into SOI rib waveguides while maintaining a device excess loss below 1 dB.

Coupled mode theory simulations accurately described the behaviour of TE polarized modes of implanted Bragg gratings in SOI rib waveguides; however they overestimated the response of TM polarized modes. This could be a result of neglecting the longitudinal (z) component of the electric field when calculating the coupling coefficient. More investigations should be carried out to understand the effect of high

index contrast and polarization dependence inherent to silicon photonics on the coupling coefficient.

To gain a better understanding of the Bragg grating response a more detailed study of the amorphous silicon damage profile and its optical properties at telecommunication wavelengths would be beneficial for this project and the silicon photonics platform in general. Also, a more detailed study on geometric device design to alleviate the effects of birefringence on the TE and TM responses is required. Further annealing studies would also be interesting in an attempt to minimize absorption and scattering losses and to understand the thermal stability of implanted Bragg gratings.

It is hoped that this work has introduced the viability of ion implanted Bragg gratings in silicon photonics and may serve as the foundation to many more devices, such as thermo-optically and free-carrier controlled optical modulators and switches. It has been demonstrated that implanted Bragg gratings exhibit benefits over etched gratings, while the added versatility of ion implantation can lead to the realization of innumerable devices that are only limited by imagination.

References

[1] G. Keiser, *Optical Fiber Communications.* New York: McGraw-Hill, 1983, pp. 318.

[2] T. K. Woodward and A. V. Krishnamoorthy, "1-Gb/s integrated optical detectors and receivers in commercial CMOS technologies," *IEEE Journal on Selected Topics in Quantum Electronics,* vol. 5, pp. 146-156, 1999.

[3] S. E. Miller, "Integrated Optics: An Introduction," *Bell Syst. Tech. J.,* pp. 2059, 1969.

[4] J. L. Merz, "III-V heterostructure devices for integrated optics," *Optical Engineering,* vol. 19, pp. 581-586, 1980.

[5] L. Eldada and L. W. Shacklette, "Advances in polymer integrated optics," *IEEE Journal on Selected Topics in Quantum Electronics,* vol. 6, pp. 54-68, 2000.

[6] C. Dominguez, J. A. Rodriguez, F. J. Munoz and N. Zine, "Plasma enhanced CVD silicon oxide films for integrated optic applications," *Vacuum,* vol. 52, pp. 395-400, 1999.

[7] R. M. Almeida, "Sol-gel planar waveguides for integrated optics," *J. Non Cryst. Solids,* vol. 259, pp. 176-181, 1999.

[8] B. G. Streetman, *Solid State Electronic Devices.* ,2d -- ed.Englewood Cliffs, N.J.: Prentice-Hall, 1980, pp. 461.

[9] R. A. Soref, "Silicon-based optoelectronics," *Proc IEEE,* vol. 81, pp. 1687-1706, 1993.

[10] G. T. Reed and A. P. Knights, *Silicon Photonics : An Introduction.* Chichester, West Sussex, England ; Etobicoke, Ont.: John Wiley & Sons, 2004, pp. 255.

[11] L. Pavesi and D. J. Lockwood, *Silicon Photonics.* , vol. 94, Berlin ; New York: Springer, 2004, pp. 397.

[12] S. G. Johnson, S. Fan, P. R. Villeneuve, J. D. Joannopoulos and L. A. Kolodziejski, "Guided modes in photonic crystal slabs," *Phys. Rev. B,* vol. 60, pp. 5751-5758, Aug. 1999.

[13] C. Kittel, *Introduction to Solid State Physics.* ,6th -- ed.New York ; Toronto: Wiley, 1986, pp. 646.

[14] M. A. Foster, A. C. Turner, J. E. Sharping, B. S. Schmidt, M. Lipson and A. L. Gaeta, "Broad-band optical parametric gain on a silicon photonic chip," *Nature,* vol. 441, pp. 960-963, 2006.

[15] L. D. Negro, M. Cazzanelli, Z. Gaburro, L. Pavesi, D. Pacifici, F. Priolo, G. Franzo and F. Iacona, "Optical gain in PECVD grown silicon nanocrystals," in *Optical Properties of Nanocrystals,* 2002, pp. 13-27.

[16] A. Liu, L. Liao, H. Rong, R. Jones, D. Samara-Rubio, D. Rubin, R. Cohen, O. Cohen, D. Hak, T. Franck, U. D. Keif and M. Paniccia, "Recent development in silicon photonics: 2.5 Gb/s silicon optical modulator and silicon raman laser," in *Optoelectronic Integration on Silicon II,* 2005, pp. 80-93.

[17] A. G. Rickman, G. T. Reed and F. Namavar, "Silicon-on-insulator optical rib waveguide loss and mode characteristics," *J. Lightwave Technol.,* vol. 12, pp. 1771-1776, 1994.

[18] T. Aalto, M. Kapulainen, S. Yliniemi, P. Heimala and M. Leppihalme, "Fast thermo-optical switch based on SOI waveguides," in *PROCEEDINGS OF SPIE: Integrated Optics: Devices, Materials, and Technologies VII,* 2003, pp. 149-159.

[19] Q. Fang, Y. He, H. Xin, F. Li and Y. Liu, "Efficient MMI SOI splitter with multimode input/output waveguides," *Pan Tao Ti Hsueh Pao/Chinese Journal of Semiconductors,* vol. 26, pp. 276-280, 2005.

[20] J. D. B. Bradley, P. E. Jessop and A. P. Knights, "Silicon waveguide-integrated optical power monitor with enhanced sensitivity at 1550 nm," *Appl. Phys. Lett.,* vol. 86, pp. 241103, 2005.

[21] F. Sun, J. Yu and S. Chen, "Directional-coupler-based Mach-Zehnder interferometer in silicon-on-insulator technology for optical intensity modulation," *Optical Engineering,* vol. 46, pp. 025601, 2007.

[22] H. Nishihara, M. Haruna and T. Suhara, *Optical Integrated Circuits.* New York, NY: McGraw-Hill, 1989, pp. 374.

[23] A. Othonos and K. Kalli, *Fiber Bragg Gratings : Fundamentals and Applications in Telecommunications and Sensing.* Boston: Artech House, 1999, pp. 422.

[24] L. C. West, C. W. Roberts, E. C. Piscani, M. Dubey, K. A. Jones and G. F. McLane, "Three-dimensional packaging of very large scale integrated optics (VLSIO) for high-complexity optical systems," in *Optoelectronic Packaging,* 1996, pp. 9-17.

[25] K. Aiki, M. Nakamura and J. Umeda, "Lasing characteristics of distributed-feedback GaAs-GaAlAs diode lasers with separate optical and carrier confinement," *IEEE J. Quant. Electron.,* vol. QE-12, pp. 597-603, 1976.

[26] K. Aiki, M. Nakamura and J. Umeda, "Frequency-multiplexing light source with monolithically integrated distributed-feedback diode lasers," *IEEE J. Quant. Electron.,* vol. QE-13, pp. 220-223, 1977.

[27] R. Kazarinov, "Narrow-band resonant optical reflectors and resonant optical transformers for laser stabilization and wavelength division multiplexing," *Quantum Electronics, IEEE Journal of,* vol. 23, pp. 1419-1425, 1987.

[28] G. D. Maxwell, R. Kashyap, B. J. Ainslie, D. L. Williams and J. R. Armitage, "UV written 1.5 µm reflection filters in single mode planar silica guides," *Electron. Lett.,* vol. 28, pp. 2106-2107, 1992.

[29] K. Kalli, H. L. Dobb, D. J. Webb, K. Carroll, C. Themistos, M. Komodromos, G. -. Peng, Q. Fang and I. W. Boyd, "Development of an electrically tuneable Bragg grating filter in polymer optical fibre operating at 1.55 νm," *Measurement Science and Technology,* vol. 18, pp. 3155-3164, 2007.

[30] A. Cutolo, M. Iodice, A. Irace, P. Spirito and L. Zeni, "Electrically controlled Bragg reflector integrated in a rib silicon on insulator waveguide," *Appl. Phys. Lett.,* vol. 71, pp. 199-201, 1997.

[31] S. Honda, Z. Wu, J. Matsui, K. Utaka, T. Edura, M. Tokuda, K. Tsutsui and Y. Wada, "Largely-tunable wideband Bragg gratings fabricated on SOI rib waveguides employed by deep-RIE," *Electron. Lett.,* vol. 43, pp. 630-631, 2007.

[32] T. Haensel, A. Schindler and B. Dissing, "Multiple high period accuracy gratings fabricated by holographic exposure and ion beam etching with nanometer depth accuracy in silicon," in *Optical Manufacturing and Testing V,* 2003, pp. 73-80.

[33] Z. Wu, W. Zhang, Z. Wang, G. Kai, S. Yuan, X. Dong, K. Utaka and Y. Wada, "Fabrication and evaluation of Bragg gratings on optimally designed silicon-on-insulator rib waveguides using electron-beam lithography," *Pan Tao Ti Hsueh Pao/Chinese Journal of Semiconductors,* vol. 27, pp. 1347-1350, 2006.

[34] D. J. Moss, V. Ta'eed, B. J. Eggleton, D. Freeman, M. Samoc, S. Madden, B. Luther-Davies, S. Janz and D. -. Xu, "High order mode conversion via focused ion beam milled bragg gratings in silicon-on-insulator waveguides," in *2004 IEEE LEOS Annual Meeting Conference Proceedings, LEOS 2004,* 2004, pp. 859-860.

[35] D. J. Moss, V. G. Ta'Eed, B. J. Eggleton, D. Freeman, S. Madden, M. Samoc, B. Luther-Davies, S. Janz and D. -. Xu, "Bragg gratings in silicon-on-insulator waveguides by focused ion beam milling," *Appl. Phys. Lett.,* vol. 85, pp. 4860-4862, 2004.

[36] E. C. Baranova, V. M. Gusev, Y. V. Martynenko, C. V. Starinin and I. B. Haibullin, "On silicon amorphization during different mass ion implantation," *Radiation Effects,* vol. 18, pp. 21-26, 1973.

[37] C. N. Waddell, W. G. Spitzer, J. E. Fredrickson, G. K. Hubler and T. A. Kennedy, "Amorphous silicon produced by ion implantation: effects of ion mass and thermal annealing," *J. Appl. Phys.,* vol. 55, pp. 4361-4366, 1984.

[38] H. Y. Fan and A. K. Ramdas, "Infrared Absorption and Photoconductivity in Irradiated Silicon," *J. Appl. Phys.,* vol. 30, pp. 1127-1134, August 1959. 1959.

[39] F. L. Pedrotti and L. S. Pedrotti, *Introduction to Optics.* Englewood Cliffs, N.J.: Prentice-Hall, 1987, pp. 551.

[40] E. Hecht, *Optics.* ,3rd ed.Reading, Mass.: Addison-Wesley, 1998, pp. 694.

[41] A. Yariv, P. Yeh and A. Yariv, *Photonics : Optical Electronics in Modern Communications.* ,6th ed.New York: Oxford University Press, 2007, pp. 836.

[42] A. Donval, R. Oron, M. Oron, A. N. M. M. Choudhury, T. R. Stanczyk and D. Richardson, "Low loss optical interconnects to silicon waveguides," in *Integrated Optics: Devices, Materials, and Technologies X,* 2006, pp. 61231.

[43] R. A. Soref, J. Schmidtchen and K. Petermann, "Large single-mode rib waveguides in GeSi-Si and Si-on-SiO_2," *IEEE J. Quant. Electron.,* vol. 27, pp. 1971-1974, 1991.

[44] A. G. Rickman, G. T. Reed and F. Namavar, "Silicon-on-insulator optical rib waveguide loss and mode characteristics," *J. Lightwave Technol.,* vol. 12, pp. 1771-1776, 1994.

[45] S. P. Pogossian, L. Vescan and A. Vonsovici, "Single-mode condition for semiconductor rib waveguides with large cross section," *J. Lightwave Technol.,* vol. 16, pp. 1851-1853, 1998.

[46] D. Yevick, "A guide to electric field propagation techniques for guided-wave optics," *Opt. Quant. Electron.,* vol. 26, pp. S185-S197, 03/01. 1994.

[47] R. Scarmozzino, "Numerical techniques for modeling guided-wave photonic devices," *Selected Topics in Quantum Electronics, IEEE Journal of,* vol. 6, pp. 150-162, 2000.

[48] D. L. Lee, *Electromagnetic Principles of Integrated Optics.* New York: Wiley, 1986, pp. 331.

[49] J. D. Plummer, M. D. Deal and P. B. Griffin, *Silicon VLSI Technology : Fundamentals, Practice, and Modeling.* Upper Saddle River, NJ: Prentice Hall, 2000, pp. 817.

[50] A. Harke, "Low-loss singlemode amorphous silicon waveguides," *Electronics Letters,* vol. 41, pp. 1377-1379, 2005.

[51] M. J. A. De Dood, A. Polman, T. Zijlstra and Van der Drift, E.W.J.M., "Amorphous silicon waveguides for microphotonics," *J. Appl. Phys.,* vol. 92, pp. 649, 2002.

[52] L. Pelaz, L. A. Marqus and J. Barbolla, "Ion-beam-induced amorphization and recrystallization in silicon," *J. Appl. Phys.,* vol. 96, pp. 5947-5976, 2004.

[53] J. S. Moore and G. R. Srinivasan, "Monte Carlo simulation of ion implantation in crystalline silicon using Marlowe," *J. Electrochem. Soc.,* vol. 135, pp. 2034-2038, 1988.

[54] M. Posselt, "Crystal-TRIM and its application to investigations on channeling effects during ion implantation," *Radiation Effects and Defects in Solids,* vol. 130-31, pp. 87-119, 1994.

[55] J. W. Corbett, *Electron Radiation Damage in Semiconductors and Metals.* , vol. Supplement 7, New York: Academic Press, 1966, pp. 410.

[56] W. P. Maszara and G. A. Rozgonyi, "Kinetics of damage production in silicon during self-implantation," *J. Appl. Phys.,* vol. 60, pp. 2310-2315, October 1, 1986. 1986.

[57] F. MOREHEAD JR and C. BL, "Model for the formation of amorphous Si by ion bombardment," vol. 6, pp. 27-32, 1970.

[58] G. Muller, S. Kalbitzer and G. N. Greaves, "Ion beams in amorphous semiconductor research," in , vol. 45, Anonymous 1997, pp. 85-123.

[59] D. A. Thompson, A. Golanski, K. H. Haugen, D. V. Stevanovic, G. Carter and C. E. Christodoulides, "Disorder production and amorphization in ion implanted silicon," *Radiation Effects,* vol. 52, pp. 69-84, 1980.

[60] J. S. Williams and J. M. Poate, *Ion Implantation and Beam Processing.* Sydney ; New York: Academic Press, 1984, pp. 419.

[61] L. M. Howe and M. H. Rainville, "Features of collision cascades in silicon as determined by transmission electron microscopy," *Nucl. Instrum. Methods,* vol. 182/183, pp. 143-15, 1980.

[62] W. G. Spitzer, G. K. Hubler and T. A. Kennedy, "Properties of amorphous silicon produced by ion implantation: thermal annealing," *Nuclear Instruments & Methods in Physics Research,* vol. 209-210, pp. 309-312, 1982.

[63] S. T. Pantelides, "Defects in Amorphous Silicon: A New Perspective," *Phys. Rev. Lett.,* vol. 57, pp. 2979-2982, Dec. 1986.

[64] S. Coffa, F. Priolo and A. Battaglia, "Defect production and annealing in ion-implanted amorphous silicon," *Phys. Rev. Lett.,* vol. 70, pp. 3756, 1993.

[65] F. F. Morehead, B. L. Crowder and R. S. Title, "Formation of Amorphous Silicon by Ion Bombardment as a Function of Ion, Temperature, and Dose," *J. Appl. Phys.,* vol. 43, pp. 1112-1118, March 1972. 1972.

[66] E. C. Baranova, V. M. Gusev, Y. V. Martynenko and I. B. Haibullin, "Effect of irradiation temperature on Si amorphization process," *Radiation Effects,* vol. 25, pp. 157-162, 1975.

[67] J. M. Haile, *Molecular Dynamics Simulation : Elementary Methods.* New York: Wiley, 1992, pp. 489.

[68] M. T. Robinson, "Binary collision approximation: Background and introduction," *Radiation Effects and Defects in Solids,* vol. 130-31, pp. 3-20, 1994.

[69] I. Manning, "Transport-theory approach to ion-beam mixing and recoil implantation," *Phys. Rev. B,* vol. 42, pp. 9853-9858, Dec. 1990.

[70] Institute of Physics, International Union of Pure and Applied Physics and United States. Air Force, *Radiation Damage and Defects in Semiconductors.* , vol. 16, London: Institute of Physics, 1973, pp. 458.

[71] S. U. Campisano, S. Coffa, V. Raineri, F. Priolo and E. Rimini, "Mechanisms of amorphization in ion implanted crystalline silicon," *Nucl Instrum Methods Phys Res Sect B,* vol. 80-81, pp. 514, 1993.

[72] L. A. Christel, J. F. Gibbons and T. W. Sigmon, "Displacement criterion for amorphization of silicon during ion implantation," *J. Appl. Phys.,* vol. 52, pp. 7143-7146, December 1981. 1981.

[73] J. E. Fredrickson, C. N. Waddell, W. G. Spitzer and G. K. Hubler, "Effects of thermal annealing on the refractive index of amorphous silicon produced by ion implantation," *Chemical Technology Review,* pp. 219-229, 1983.

[74] G. K. Hubler, C. N. Waddell, W. G. Spitzer, J. E. Fredrickson, S. Prussin and R. G. Wilson, "High-fluence implantations of silicon: layer thickness and refractive indices," *J. Appl. Phys.,* vol. 50, pp. 3294-3303, 1979.

[75] C. N. Waddell, W. G. Spitzer, J. E. Fredrickson, G. K. Hubler and T. A. Kennedy, "Amorphous silicon produced by ion implantation: effects of ion mass and thermal annealing," *J. Appl. Phys.,* vol. 55, pp. 4361-4366, 1984.

[76] C. N. Waddell, W. G. Spitzer, G. K. Hubler and J. E. Fredrickson, "Infrared studies of isothermal annealing of ion-implanted silicon: refractive indices, regrowth rates, and carrier profiles," *J. Appl. Phys.,* vol. 53, pp. 5851-5862, 1982.

[77] W. Wesch, E. Glaser, G. Goetz, H. Karge and R. Prager, "Correlation between structural defects and optical properties in ion-implanted silicon," *Physica Status Solidi (A) Applied Research,* vol. 65, pp. 225-232, 1981.

[78] J. S. Custer, M. O. Thompson, D. C. Jacobson, J. M. Poate, S. Roorda, W. C. Sinke and F. Spaepen, "Density of amorphous Si," *Appl. Phys. Lett.,* vol. 64, pp. 437, 1994.

[79] U. Zammit, K. N. Madhusoodanan, M. Marinelli, F. Scudieri, R. Pizzoferrato, F. Mercuri, E. Wendler and W. Wesch, "Optical absorption studies of ion implanted and amorphous silicon," *Journal De Physique. IV : JP,* vol. 4, pp. 7-113, 1994.

[80] S. Roorda, W. C. Sinke, J. M. Poate, D. C. Jacobson, S. Dierker, B. S. Dennis, D. J. Eaglesham, F. Spaepen and P. Fuoss, "Structural relaxation and defect annihilation in pure amorphous silicon," *Phys. Rev. B. Condens Matter,* vol. 44, pp. 3702-3725, Aug 15. 1991.

[81] A. J. M. Berntsen, W. F. van der Weg, P. A. Stolk and F. W. Saris, "Separating the effects of hydrogen and bond-angle variation on the amorphous-silicon band gap," *Phys. Rev. B,* vol. 48, pp. 14656-14658, Nov. 1993.

[82] G. K. Hubler, C. N. Waddell, W. G. Spitzer, J. E. Fredrickson and T. A. Kennedy, "Physical properties of two metastable states of amorphous silicon," in *Ion Implantation and Ion Beam Processing of Materials,* 1984, pp. 217-222.

[83] J. E. Fredrickson, C. N. Waddell, W. G. Spitzer and G. K. Hubler, "Effects of thermal annealing on the refractive index of amorphous silicon produced by ion implantation," *Chemical Technology Review,* pp. 219-229, 1983.

[84] F. Schwidefsky, "Increase of the refractive index of silicon films by dangling bonds," *Thin Solid Films,* vol. 18, pp. 45-52, 1973.

[85] A. Mathew and K. N. Madhusoodanan, "Subgap optical absorption studies in boron implanted silicon," *Japanese Journal of Applied Physics, Part 1: Regular Papers and Short Notes and Review Papers,* vol. 43, pp. 5088-5094, 2004.

[86] E. Wendler, K. Gartner, W. Wesch, U. Zammit and K. N. Madhusoodanan, "Defect investigation in boron implanted silicon by means of temperature dependent RBS and

optical near-edge absorption," *Nucl Instrum Methods Phys Res Sect B,* vol. 85, pp. 528, 1994.

[87] A. P. Knights and G. F. Hopper, "Effect of ion implantation induced defects on optical attenuation in silicon waveguides," *Electron. Lett.,* vol. 39, pp. 1648-1649, 2003.

[88] P. G. Coleman, C. P. Burrows and A. P. Knights, "Simple expression for vacancy concentrations at half ion range following MeV ion implantation of silicon," *Appl. Phys. Lett.,* vol. 80, pp. 947, 2002.

[89] L. J. Cheng, J. C. Corelli, J. W. Corbett and G. D. Watkins, "1.8-, 3.3-, and 3.9-\mu Bands in Irradiated Silicon: Correlations with the Divacancy," *Phys. Rev.,* vol. 152, pp. 761-774, Dec. 1966.

[90] J. W. Corbett, J. P. Karins and T. Y. Tan, "Ion-induced defects in semiconductors," *Nucl. Instrum. Methods,* vol. 182/183, pp. 457-47, 1980.

[91] W. Jung and G. S. Newell, "Spin-1 Centers in Neutron-Irradiated Silicon," *Phys. Rev.,* vol. 132, pp. 648-662, Oct. 1963.

[92] H. J. Stein, F. L. Vook and J. A. Borders, "Direct evidence of divacancy formation in silicon by ion implantation," *Appl. Phys. Lett.,* vol. 14, pp. 328-330, May 15, 1969. 1969.

[93] G. D. Cody, T. Tiedje, B. Abeles, B. Brooks and Y. Goldstein, "Disorder and the Optical-Absorption Edge of Hydrogenated Amorphous Silicon," *Phys. Rev. Lett.,* vol. 47, pp. 1480-1483, Nov. 1981.

[94] G. N. van den Hoven, Z. N. Liang, L. Niesen and J. S. Custer, "Evidence for vacancies in amorphous silicon," *Phys. Rev. Lett.,* vol. 68, pp. 3714-3717, Jun. 1992.

[95] W. Sinke, T. Warabisako, M. Miyao, T. Tokuyama, S. Roorda and F. W. Saris, "Transient structural relaxation of amorphous silicon," *J. Non Cryst. Solids,* vol. 99, pp. 308-323, 1988.

[96] B. E. Little, "Variational coupled-mode theory including radiation loss for grating-assisted couplers," *J. Lightwave Technol.,* vol. 14, pp. 188-195, 1996.

[97] D. L. Jaggard and C. Elachi, "Floquet and couple-waves analysis of higher-order Bragg coupling in a periodic medium," *J. Opt. Soc. Am.,* vol. 66, pp. 674-682, 1976.

[98] B. Crosignani, P. D. Porto and A. Yariv, "Coupled-mode theory and slowly-varying approximation in guided-wave optics," *Opt. Commun.,* vol. 78, pp. 237-239, 1990.

[99] A. Bakhtazad, H. Abiri, R. Ghayour, H. R. Mohammad and Z. Mehrdad, "Orthogonal coupled mode theory for rectangular dielectric waveguides," *Proc SPIE Int Soc Opt Eng,* vol. 3625, pp. 165-175, 1999.

[100] A. Yariv, *Introduction to Optical Electronics.* ,2nd ed. New York: Holt, Rinehart and Winston, 1976, pp. 438.

[101] S. Cho, B. Kim and N. Dagli, "Extended additional layer method of calculating the coupling coefficient of arbitrarily shaped gratings," *Microwave Opt. Techno.l Lett.,* vol. 16, pp. 143-145, 1997.

[102] S. Park, S. H. Song, C. Oh and P. Kim, "Ray-optical determination of the coupling coefficients of grating waveguide by use of the rigorous coupled-wave theory," *J. Lightwave Technol.,* vol. 19, pp. 120-125, 2001.

[103] P. Verly, R. Tremblay and J. W. Y. Lit, "Application of the effective-index method to the study of distributed feedback in corrugated waveguides. TE polarization," *J. Opt. Soc. Am.,* vol. 70, pp. 964-968, 1980.

[104] P. Brosson, C. Artigue, B. Fernier, D. Leclerc, J. Jacquet and J. Benoit, "Simple determination of coupling coefficient in DFB waveguide structures," *Electron. Lett.,* vol. 24, pp. 990-991, 1988.

[105] K. David, J. Buus, G. Morthier and R. Baets, "Coupling coefficients in gain-coupled DFB lasers: Inherent compromise between coupling strength and loss," *IEEE Photonics Technology Letters,* vol. 3, pp. 439-441, 1991.

[106] Y. Luo, C. -. Sun, Y. Nakano and K. Tada, "Analysis of gain and index coupling coefficients of DFB semiconductor lasers using a practical model," *Int. J. Optoelectron.,* vol. 10, pp. 331-335, 1995.

[107] S. Cristoloveanu and G. K. Celler, "Frontiers of silicon-on-insulator," *J. Appl. Phys.,* vol. 93, pp. 4955-4978, 2003.

[108] J. Schmidtchen, A. Splett, B. Schueppert, K. Petermann and G. Burbach, "Low loss singlemode optical waveguides with large cross-section in silicon-on-insulator," *Electron. Lett.,* vol. 27, pp. 1486-1488, 1991.

[109] P. D. Trinh, S. Yegnanarayanan and B. Jalali, "Integrated optical directional couplers in silicon-on-insulator," *Electron. Lett.,* vol. 31, pp. 2097-2098, 1995.

[110] R. A. Ghanbari, "Physics and Fabrication of Quasi-One-Dimensional Conductors," Doctoral Thesis, MIT, 1993.

[111] K. O. Hill, B. Malo, F. Bilodeau, D. C. Johnson and J. Albert, "Bragg gratings fabricated in monomode photosensitive optical fiber by UV exposure through a phase mask," *Appl. Phys. Lett.,* vol. 62, pp. 1035-1037, 1993.

[112] J. Schrauwen, F. Van Laere, D. Van Thourhout and R. Baets, "Focused-ion-beam fabrication of slanted grating couplers in silicon-on-insulator waveguides," *IEEE Photonics Technology Letters,* vol. 19, pp. 816-818, 2007.

[113] J. G. Goodberlet, "Patterning 100 nm features using deep-ultraviolet contact photolithography," *Appl. Phys. Lett.,* vol. 76, pp. 667-669, 2000.

[114] L. Guo, P. R. Krauss and S. Y. Chou, "Nanoscale silicon field effect transistors fabricated using imprint lithography," *Appl. Phys. Lett.,* vol. 71, pp. 1881-1883, 1997.

[115] B. J. Eggleton, P. S. Westbrook, C. A. White, C. Kerbage, R. S. Windeler and G. L. Burdge, "Cladding-mode-resonances in air-silica microstructure optical fibers," *J. Lightwave Technol.,* vol. 18, pp. 1084-1100, 2000.

[116] P. J. Foster, J. K. Doylend, P. Mascher, A. P. Knights and P. G. Coleman, "Optical attenuation in defect-engineered silicon rib waveguides," *J. Appl. Phys.,* vol. 99, pp. 073101, 2006.